

# Bayesian Optimization with Gaussian Processes to Accelerate Stationary Point Searches

✉ Rohit Goswami<sup>1</sup>

Institute IMX and Lab-COSMO  
École polytechnique fédérale de Lausanne (EPFL)  
Station 12, CH-1015 Lausanne, Switzerland

rgoswami@ieee.org

March 17, 2026

## Abstract

Accelerating the explorations of stationary points on potential energy surfaces building local surrogates spans decades of effort. Done correctly, surrogates reduce required evaluations by an order of magnitude while preserving the accuracy of the underlying theory. We present a unified Bayesian Optimization view of minimization, single point saddle searches, and double ended saddle searches through a unified six-step surrogate loop, differing only in the inner optimization target and acquisition criterion. The framework uses Gaussian process regression with derivative observations, inverse-distance kernels, and active learning. The Optimal Transport GP extensions of farthest point sampling with Earth mover’s distance, MAP regularization via variance barrier and oscillation detection, and adaptive trust radius form concrete extensions of the same basic methodology, improving accuracy and efficiency. We also demonstrate random Fourier features decouple hyperparameter training from predictions enabling favorable scaling for high-dimensional systems. Accompanying pedagogical Rust code demonstrates that all applications use the exact same Bayesian optimization loop, bridging the gap between theoretical formulation and practical execution.

**Keywords:** Gaussian Process Regression, Bayesian Optimization, Saddle Point Search, Dimer Method, NEB, Active Learning

## 1 Introduction

Chemical reactions, atomic diffusion in crystals, and conformational changes in proteins all represent trajectories through a high-dimensional configurational space. For a system of  $N$  atoms, assuming a ground electronic state under the Born-Oppenheimer approximation decouples electronic and nuclear motion. Fundamentally, this physical decoupling simply maps a  $3N$ -dimensional spatial coordinate  $\mathbf{x}$  to a relative scalar energy  $y$ , generating the potential energy surface (PES). Due to methodological differences in calculations of absolute energies, the exact numerical value of  $y$  holds no intrinsic physical weight for locating geometries. According to Boltzmann statistics, stable species occupy hyper-volumes around local energy minima [1]. Transitioning between stable states requires the system to cross a dividing surface, optimally through a first-order saddle point where the gradient vanishes and the Hessian matrix possesses exactly one negative eigenvalue, with the eigenvector corresponding to this negative eigenvalue taken to be the reaction coordinate. Harmonic transition state theory (HTST) [2–4] relates the saddle point to the rate constant:

$$k_{\text{HTST}} = \frac{\prod_{i=1}^{3N} \nu_i^{\min}}{\prod_{i=1}^{3N-1} \nu_i^{\text{SP}}} \exp\left(-\frac{E_{\text{SP}} - E_{\min}}{k_B T}\right) \quad (1.1)$$

The rate depends exponentially on the barrier  $E_{\text{SP}} - E_{\min}$ , with the vibrational frequency ratio ( $\nu_i^{\min}$  at the minimum,  $\nu_i^{\text{SP}}$  at the saddle) acting as a prefactor that captures the width of the two basins. The denominator runs over  $3N - 1$  modes because the saddle has one imaginary frequency along the reaction

coordinate under four assumptions covered elsewhere [5]. In practice, predicting the rate reduces to finding the minima and saddle points<sup>2</sup>. To this end we consider minimization on an energy surface, along with two common modalities to find saddle points. To this end we consider minimization on an energy surface, along with two common modalities to find saddle points. We will use the term “point searches” to cover the union of the search methods.

The global minimum for such systems being largely ill defined due to the lack of an absolute zero, so the map from geometry to energy and atomistic forces (the pointwise derivative w.r.t positions) also ends up being relative. One can construct several alternative surrogate energy surfaces that perfectly preserve the minima and saddles of the true PES, even if those surrogates distort the broader configurational space. This inherently local understanding of the process provides the leeway required to handle the extreme dimensionality of the  $3N$  space despite there being “no-free-lunch” [6] and has connections to vibrational analysis [7].

Point searches typically need hundreds of such evaluations to converge, and this cost becomes prohibitive in large-scale studies where workflow-driven screening with tools such as AiiDA [8] or Snakemake [9] may require characterizing thousands of distinct transitions. may require characterizing thousands of distinct transitions. The problem is compounded in applications that embed saddle searches as an inner loop. Adaptive kinetic Monte Carlo (AKMC) [10, 11] discovers escape routes on the fly from each visited minimum, reaction network exploration catalogs competing pathways in complex catalytic cycles, and high-throughput screening for materials design may require characterizing saddle points across hundreds of candidate systems. In each case, the per-search cost of electronic structure evaluations is the rate-limiting step, and reducing it from hundreds of calls to tens opens qualitatively different scales of investigation.

When electronic structure methods calculate  $y$  and its gradients, single queries consume minutes to hours. Machine learning has opened two distinct approaches to this bottleneck. The first strategy constructs *global* machine-learned interatomic potentials (MLIPs), models trained on a large database of electronic structure calculations that approximates the PES over a broad region of configuration space by mapping onto a descriptor space [12, 13]. Gaussian Approximation Potentials (GAP) [14] using SOAP descriptors, moment tensor potentials (MTP) [15], and neural network potentials (NNP) [16] exemplify this approach; the review by Deringer, Bartok, and Csanyi [17] covers this area in detail. More recently, universal foundation models such as PET-MAD [18, 19] and MACE-MP-0 [20] have demonstrated transferability across the periodic table. These global models enable fast energy and force evaluation and allow molecular dynamics, geometry optimizations, and NEB calculations to run at near-electronic-structure accuracy.

Saddle points in particular however, occupy a vanishingly small, rarely sampled fraction of the total volume. Applying a global MLIP to saddle point searches encounters a fundamental sampling problem. Saddle points are rare events, and equilibrium sampling almost never visits them. Random structure searches explore configuration space without bias toward the transition region. Most training sets assembled from these approaches will have a blind spot precisely where it matters for kinetics [21]. The MLIP may give accurate energies near minima (where training data is plentiful) but unreliable predictions near the transition state (where it is sparse). Retraining a global potential or even fine-tuning for every novel reaction pathway could defeat the purpose of high-throughput screening.

The second strategy, and the subject of this review, constructs a *local, ephemeral* surrogate of the PES on-the-fly during each individual search, using only the data generated in the course of that specific calculation. This is an active learning approach [22, 23] in which the surrogate model decides where to sample next, balancing exploitation of the current prediction against exploration of uncertain regions [23, 24]. The surrogate need not represent the PES globally; it only needs to be accurate near the path being optimized. Convergence to a saddle point typically requires on the order of 30 electronic structure evaluations [25], compared to the thousands needed for even a modest MLIP. The surrogate is discarded after each search completes.

The local GP accelerates exactly the PES that the user intends to study. There is no dependence on a training database assembled at some other level of theory or for some other class of systems. The GP learns from the electronic structure method of choice (DFT, coupled cluster, or any other) as the search proceeds, and the accuracy of the surrogate improves precisely where it matters, near the transition path under investigation. In contrast, deploying a global MLIP for saddle point searches requires either (a) retraining or fine-tuning the potential for each new system and electronic structure method, or (b) accepting that the pre-trained potential may be unreliable in the transition state region where training data is sparse. The local GP sidesteps this

---

<sup>2</sup>along with the Hessian test for the first order saddle point estimate, often skipped in high throughput workflows

problem entirely, being system-specific and method-specific by construction. This distinction between global and local modeling forms the conceptual backbone of the review: Section 2 establishes the physical setting and classical methods, Section 3 develops the GP framework, and Sections 5, 6, and 7 show how the local GP approach applies to each classical method.

Gaussian process regression (GPR) [26, 27] is well matched to this local surrogate role. The GP posterior provides two quantities required by the active learning loop: the predicted energy surface (the posterior mean) and a calibrated uncertainty estimate (the posterior variance). The variance enables active learning. Many optimization steps can be run on the cheap surrogate surface, and when the next expensive electronic structure evaluation is needed, the configuration where the GP is least certain is selected. This active learning loop (evaluate, update the model, optimize on the surrogate, evaluate again where uncertainty is highest) distinguishes the approach from passive regression on a pre-existing database.

The two approaches differ in what the GP is asked to do. In the MLIP setting, the GP is a *regression* tool that, given a large, pre-computed training set, interpolates to approximate the energy at new configurations. In the active learning setting developed here, the GP is an *acquisition* tool that decides where to acquire new data based on its own uncertainty, and the training set is assembled incrementally as a byproduct of the search itself. The kernel operates on inverse interatomic distances rather than high-dimensional structural descriptors like the smoothed overlap of atomic positions, or SOAP [28], because the model only needs to resolve the PES in a local neighborhood where pairwise distance features suffice. The inverse-distance kernel has been validated across 500+ reaction benchmarks with both SE and Matern kernels [25, 29]. The computational overhead of the GP (dominated by the  $\mathcal{O}(M^3)$  Cholesky decomposition with  $M \sim 30$ ) is negligible compared to the electronic structure cost it replaces, whereas an MLIP-scale GP with  $M \sim 10^4$  would require sparse approximations.

This tutorial review provides a self-contained treatment of GPR-accelerated stationary point searches. We develop the mathematical foundations of GPR with derivative observations in sufficient detail for a practitioner to implement the method from scratch, and apply the framework to the dimer method, the nudged elastic band (NEB), and local minimization. Accompanying Rust code (chemgp-core, available at <https://github.com/HaoZeke/ChemGP>) is both the pedagogical reference and the production implementation; each equation maps to a specific function, and the same binary runs the benchmarks reported here. We give practical guidance on hyperparameter selection, coordinate systems, trust regions, data management, and the statistical evaluation of algorithmic performance. A unifying observation runs through the three applications: every GP method shares the same Bayesian optimization outer loop of training a surrogate, selecting a query point by an acquisition criterion, evaluating the oracle. With four shared components (FPS subset, EMD trust, RFF approximation, LCB acquisition) that are formalized as the Bayesian surrogate loop in Section 4 and developed in detail within the OT-GP framework (Section 8). The unified Bayesian optimization framework using Gaussian process surrogates is detailed in Alg. 1.

The methods differ only in the optimization and acquisition phases. Minimization uses L-BFGS descent and implicit acquisition; the dimer uses CG rotation plus L-BFGS translation with trust-clipped acquisition; the NEB uses path relaxation with UCB acquisition from unevaluated images.

**Algorithm 1: Unified Bayesian surrogate loop for stationary point searches (overview)**


---

**Input:** Initial configuration(s)  $\mathbf{x}_0$ , oracle tolerance  $\epsilon$ , trust radius  $\Delta$   
**Output:** Converged stationary point(s)  $\mathbf{x}^*$

- 1 Initialize dataset  $\mathcal{D} \leftarrow \{(\mathbf{x}_0, V(\mathbf{x}_0), \nabla V(\mathbf{x}_0))\}$ ;
- 2  $\mathbf{x}^* \leftarrow \mathbf{x}_0$ ;
- 3 **while**  $|\nabla V(\mathbf{x}^*)| > \epsilon$  **do**
- 4 SELECT training subset  $\mathcal{D}_{\text{train}} \subset \mathcal{D}$  via farthest point sampling;
- 5 TRAIN hyperparameters  $\theta$  via MAP estimation;
- 6 BUILD surrogate model  $V_{\text{GP}}$  (Exact GP or Random Fourier Features);
- 7 OPTIMIZE  $\mathbf{x}_{\text{prop}}$  on  $V_{\text{GP}}$  via method-specific inner loop;
- 8 CLIP  $\mathbf{x}_{\text{prop}}$  to trust region boundary  $\Delta$  (EMD or Euclidean);
- 9 ACQUIRE new oracle evaluation at  $\mathbf{x}_{\text{prop}}$  based on acquisition criterion;
- 10 Update dataset  $\mathcal{D} \leftarrow \mathcal{D} \cup \{(\mathbf{x}_{\text{prop}}, V(\mathbf{x}_{\text{prop}}), \nabla V(\mathbf{x}_{\text{prop}}))\}$ ;
- 11 Update trust radius  $\Delta$  based on surrogate accuracy;
- 12  $\mathbf{x}^* \leftarrow \mathbf{x}_{\text{prop}}$ ;
- 13 **end**
- 14 **return** Converged stationary point(s)  $\mathbf{x}^*$

---

The review is organized as follows. Section 2 establishes the physical setting and the classical search algorithms. Section 3 develops the GPR framework, including molecular kernels and gradient observations. Section 4 formalizes the Bayesian surrogate loop that unifies the three applications. Section 5 presents GPR-accelerated minimum mode following (the GP-dimer), Section 6 covers GPR-accelerated NEB, and Section 7 treats GPR-accelerated minimization. Section 8 introduces the Optimal Transport GP (OT-GP) extensions that address scaling and stability. Section 9 connects the mathematics to executable code and describes the analysis tooling.

## 2 The Potential Energy Surface and Stationary Point Searches

### 2.1 The PES and Its Stationary Points

We collect the positions of  $N$  atoms into a single vector  $\mathbf{x} \in \mathbb{R}^{3N}$ . The PES  $V(\mathbf{x})$  [30] gives the energy at each configuration, and the atomic force vector is its negative gradient:

$$\mathbf{F}(\mathbf{x}) = -\nabla V(\mathbf{x}) \tag{2.1}$$

Every algorithm in this review queries  $V$  and  $\mathbf{F}$  at chosen configurations to locate stationary points, configurations where  $\nabla V(\mathbf{x}^*) = \mathbf{0}$ . For the search algorithms that follow, only two types of stationary point matter: local minima (all Hessian eigenvalues positive) and first-order saddle points (exactly one negative eigenvalue). The eigenvector belonging to that negative eigenvalue is the *minimum mode* and points along the reaction coordinate. Six zero eigenvalues from rigid-body translation and rotation must be projected out. Figure 12 shows the Muller-Brown surface [31], a standard 2D test PES, with its three minima, two saddle points, and a converged minimum energy path.

The *minimum energy path* (MEP) [4] connects a saddle point to the adjacent minima along the steepest descent:

$$\frac{d\mathbf{x}}{ds} = -\frac{\nabla V(\mathbf{x})}{|\nabla V(\mathbf{x})|} \tag{2.2}$$

where  $s$  is arc length. The energy difference between the saddle and the minimum is the barrier that enters the HTST rate (Eq. 1.1) [5]. The two families of algorithms in Sections 2.3 and 2.4 approach the problem from opposite ends. The dimer method [32] searches for the saddle without knowing the MEP, while the NEB [33] approximates the entire MEP and locates the saddle as its highest point through the climbing image extension [34]. Both classical methods rely on repeated evaluations of the true PES and its gradients, which motivates the GP acceleration strategies developed in Sections 3 and 5.

## 2.2 Local Minimization

Local minimization is the simplest stationary point problem, where the system relaxes along the negative gradient until the forces vanish. Limited memory Broyden–Fletcher–Goldfarb–Shanno, or L-BFGS [35–37], approximates the Hessian using gradient evaluations, to save on computing the full Hessian. The L-BFGS here finds use for both dimer translation and surrogate optimization, and plays a central role throughout the GPR-accelerated algorithms. L-BFGS maintains a history of  $m$  recent position and gradient differences  $\{(\mathbf{s}_k, \mathbf{y}_k)\}$  and computes a search direction via the two-loop recursion without explicitly forming the Hessian.

$$\mathbf{s}_k = \mathbf{x}_{k+1} - \mathbf{x}_k, \quad \mathbf{y}_k = \nabla V(\mathbf{x}_{k+1}) - \nabla V(\mathbf{x}_k) \quad (2.3)$$

$$\rho_k = \frac{1}{\mathbf{y}_k^T \mathbf{s}_k}, \quad H_k^0 = \frac{\mathbf{s}_{k-1}^T \mathbf{y}_{k-1}}{\mathbf{y}_{k-1}^T \mathbf{y}_{k-1}} \mathbf{I} \quad (2.4)$$

The L-BFGS direction is then obtained by the standard two-loop recursion applied to the current gradient. This optimizer is used both within the dimer method (for translation) and within the GPR-accelerated algorithms (for optimization on the surrogate surface).

Section 3 develops the GP framework that makes surrogate-accelerated optimization possible, including the inverse-distance kernel for molecular systems and the derivative observations that provide  $3N+1$  constraints per evaluation.

## 2.3 Minimum Mode Following, the Dimer Method

The dimer method [32] estimates PES curvature by comparing forces at two nearby points, much like a finite-difference approximation to the second derivative but applied directionally. This costs just two force evaluations per direction, rather than the  $\sim 6N$  evaluations needed for the full  $3N \times 3N$  Hessian (or an analytic Hessian, which most electronic structure codes do not expose). The single lowest curvature direction, the minimum mode, points along the reaction coordinate. The two-point probe rotates until the most negative curvature is located, and the system walks uphill along it. The dimer’s cost is dominated by the rotation phase, where each translation step requires 5–15 rotation evaluations (each a full electronic structure call) to converge the orientation. This inner-loop cost is where the GP surrogate provides the largest savings [25, 38–40], as we discuss in Section 5.

Concretely, two replicas of the system are placed symmetrically about a midpoint [11]:

$$\mathbf{R}_{1,2} = \mathbf{R} \pm \Delta R \hat{\mathbf{N}} \quad (2.5)$$

where  $\hat{\mathbf{N}}$  is a unit vector (the dimer axis) and  $\Delta R$  is a small separation, typically 0.01 Å. The algorithm alternates between two operations (Figure S1, left): rotating the dimer to find the minimum curvature direction, and translating the midpoint uphill along that direction while relaxing perpendicular to it.

### 2.3.1 Rotation

The curvature along the dimer axis is estimated from the force difference at the two endpoints:

$$C(\hat{\mathbf{N}}) \approx \frac{(\mathbf{F}_2 - \mathbf{F}_1) \cdot \hat{\mathbf{N}}}{\Delta R} \quad (2.6)$$

where  $\mathbf{F}_{1,2} = \mathbf{F}(\mathbf{R}_{1,2})$ . Eq. 2.6 is a directional second derivative: the force difference across the dimer, projected onto the axis, divided by the separation. When  $C < 0$ , the axis points along a direction of negative curvature. The rotation phase minimizes  $C$  over all orientations of  $\hat{\mathbf{N}}$ , which aligns the dimer with the lowest curvature mode. The perpendicular component of the force difference supplies the gradient for this minimization, and conjugate gradient (CG) [41] with the Polak-Ribiere [42] update provides the search direction:

$$\beta_i = \frac{(\mathbf{F}_i^\perp - \mathbf{F}_{i-1}^\perp) \cdot \mathbf{F}_i^\perp}{|\mathbf{F}_i^\perp|^2} \quad (2.7)$$

CG is the default for rotation [43]. L-BFGS [44] converges in fewer steps when the minimum mode is well-separated, but it can lock onto a wrong mode when the gap is small [45]. Bayesian benchmarking [46] and theoretical considerations favor CG overall for the rotation phase [47], with the advantage concentrated in systems with near-degenerate curvature modes.

When the dimer operates on molecular systems (as opposed to 2D model surfaces), rigid-body translations and rotations must be projected out of the *translation step* [38, 48] to prevent the molecule from drifting through space. Projecting these modes out of the *orientation vector*  $\hat{\mathbf{N}}$  itself is catastrophic: it removes the component of the minimum mode that distinguishes a saddle point from a minimum. In an 8-atom system, projecting translations from the orient vector changed the estimated curvature from  $-8.4 \text{ eV}/\text{\AA}^2$  (correct, negative) to  $+103 \text{ eV}/\text{\AA}^2$  (wrong sign), causing the dimer to walk away from the saddle point. The rule is: project rigid-body modes from translation steps only, never from the dimer orientation. The projection formula and Gram-Schmidt basis construction are detailed in the SI.

### 2.3.2 Translation

Once the rotation has identified the minimum mode, translation must move the midpoint *uphill* along that mode while simultaneously relaxing in all other directions. Geometrically, this is a Householder reflection [37]: the force vector is reflected about the hyperplane perpendicular to  $\hat{\mathbf{N}}$ , which flips the sign of the component along the minimum mode while leaving the  $3N - 1$  perpendicular components unchanged. The system therefore climbs the ridge while sliding down into the valley on each side of it. The modified force is:

$$\mathbf{F}^\dagger = \begin{cases} \mathbf{F}(\mathbf{R}) - 2[\mathbf{F}(\mathbf{R}) \cdot \hat{\mathbf{N}}]\hat{\mathbf{N}} & \text{if } C(\hat{\mathbf{N}}) < 0 \\ -[\mathbf{F}(\mathbf{R}) \cdot \hat{\mathbf{N}}]\hat{\mathbf{N}} & \text{if } C(\hat{\mathbf{N}}) \geq 0 \end{cases} \quad (2.8)$$

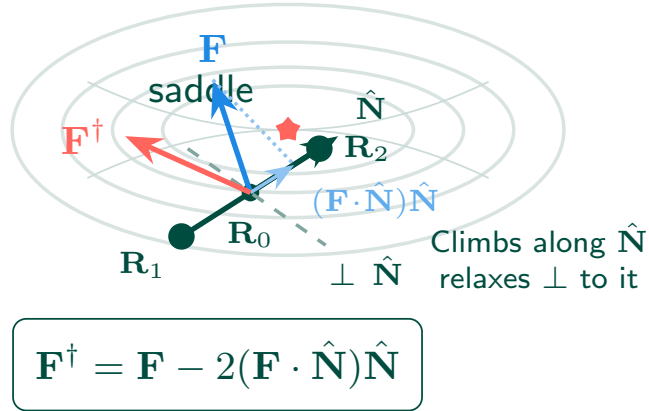


**Figure 1.** Geometry of the dimer and Householder reflection. The dimer pair ( $\mathbf{R}_1, \mathbf{R}_2$ ) straddles the midpoint  $\mathbf{R}_0$  with axis  $\hat{\mathbf{N}}$ . The true force  $\mathbf{F}$  (blue) is reflected about the hyperplane perpendicular to  $\hat{\mathbf{N}}$ , producing the modified force  $\mathbf{F}^\dagger$  (coral) that climbs along the minimum mode while relaxing perpendicular to it.

The first case ( $C < 0$ ) applies the Householder reflection just described: the dimer is already in a region of negative curvature, so climbing along  $\hat{\mathbf{N}}$  while relaxing perpendicular to it drives the system toward the saddle. The second case ( $C \geq 0$ ) handles the early phase of the search when the dimer has not yet reached the transition region; here only the component along  $\hat{\mathbf{N}}$  is retained to push the system toward the ridge. Translation uses L-BFGS, and the search terminates when the true force magnitude  $|\mathbf{F}(\mathbf{R})|$  drops below a threshold  $\epsilon_{\text{force}}$ . Algorithm 2 summarizes the full iteration.

**Algorithm 2: Classical dimer method**


---

**Input:** Midpoint  $\mathbf{R}$ , initial dimer axis  $\hat{\mathbf{N}}$ , separation  $\Delta R$ , force threshold  $\epsilon_{\text{force}}$   
**Output:** saddle point at  $\mathbf{R}$

```

1 repeat
2   Place endpoints  $\mathbf{R}_{1,2} = \mathbf{R} \pm \Delta R \hat{\mathbf{N}}$ ;
3   Evaluate  $\mathbf{F}(\mathbf{R}_1), \mathbf{F}(\mathbf{R}_2)$  on true PES;
   // Rotation
4   repeat
5      $C(\hat{\mathbf{N}}) \leftarrow (\mathbf{F}_2 - \mathbf{F}_1) \cdot \hat{\mathbf{N}} / \Delta R$ ;
6     Rotate  $\hat{\mathbf{N}}$  to minimize  $C$  (CG, Eq. 2.7);
7     Evaluate  $\mathbf{F}(\mathbf{R}_1)$  at new endpoint;
8   until rotation converged;
   // Translation
9   if  $C(\hat{\mathbf{N}}) < 0$  then
10     $\mathbf{F}^\dagger \leftarrow \mathbf{F}(\mathbf{R}) - 2[\mathbf{F}(\mathbf{R}) \cdot \hat{\mathbf{N}}]\hat{\mathbf{N}}$ ;
11  else
12     $\mathbf{F}^\dagger \leftarrow -[\mathbf{F}(\mathbf{R}) \cdot \hat{\mathbf{N}}]\hat{\mathbf{N}}$ ;
13  end
14   $\mathbf{R} \leftarrow \mathbf{R} + \text{L-BFGS step on } \mathbf{F}^\dagger$ ;
15 until  $|\mathbf{F}(\mathbf{R})| < \epsilon_{\text{force}}$ ;

```

---

The dimer’s cost is dominated by the rotation phase, since each rotation step requires a force evaluation at the new  $\mathbf{R}_1$  position (the midpoint force can be reused from the previous translation). A typical search requires 5 to 15 rotations per translation step, and 20 to 50 translation steps to converge. This inner-loop cost is where the GP surrogate provides the largest savings, as we discuss in Section 5.

The dimer method establishes the conceptual template for GP acceleration: replace expensive inner-loop evaluations with cheap surrogate predictions, and only return to the true PES to validate and extend the training set. Section 5 develops this idea in detail, showing how the GP replaces the rotation-phase force evaluations with surrogate queries, reducing the total evaluation count from hundreds to tens while preserving accuracy.

## 2.4 Double-Ended Path Methods

When both initial and final states are known, the MEP connecting them is found by optimizing a discrete chain of  $P + 1$  images  $\{\mathbf{R}_0, \mathbf{R}_1, \dots, \mathbf{R}_P\}$  with fixed endpoints. Two competing requirements must be satisfied: the images must converge toward the MEP (shape optimization) and remain well-distributed along the path (spacing control). The nudged elastic band (NEB) [33] decouples them through force projections: the true force acts only perpendicular to the local tangent, driving images toward the MEP, while fictitious spring forces act only parallel, maintaining spacing. The string method [49, 50] replaces springs with interpolation-based reparameterization ( $k \rightarrow \infty$  limit). Figure S2 (left) summarizes the NEB iteration.

### 2.4.1 The Nudged Elastic Band

A converged MEP satisfies the condition that the perpendicular force vanishes everywhere along the path:

$$(\nabla V)^\perp(\mathbf{R}) = \nabla V(\mathbf{R}) - [\nabla V(\mathbf{R}) \cdot \hat{\boldsymbol{\tau}}]\hat{\boldsymbol{\tau}} = \mathbf{0} \quad (2.9)$$

A naive elastic band, where springs connect the images and the full potential force acts on each one, fails to converge to the MEP for two reasons. First, the potential force has a component *along* the path that drags images away from the saddle region and bunches them in low-energy basins (the “sliding-down” artifact). Second, the spring force has a component *perpendicular* to the path that pulls the chain off the MEP into straight-line shortcuts through high-energy regions (the “corner-cutting” artifact) [51]. The NEB eliminates both by projecting each type of force onto the subspace where it belongs. The true force acts only perpendicular to the path, driving each image toward the MEP, while the spring force acts only parallel to the path, controlling image spacing. The total NEB force on image  $i$  is:

$$\mathbf{F}_i^{\text{NEB}} = -\nabla V(\mathbf{R}_i)|_{\perp} + \mathbf{F}_i^s|_{\parallel} \quad (2.10)$$

The perpendicular projection of the true force removes the sliding-down component:

$$-\nabla V(\mathbf{R}_i)|_{\perp} = -\nabla V(\mathbf{R}_i) + [\nabla V(\mathbf{R}_i) \cdot \hat{\boldsymbol{\tau}}_i] \hat{\boldsymbol{\tau}}_i \quad (2.11)$$

and the parallel projection of the spring force prevents corner-cutting:

$$\mathbf{F}_i^s|_{\parallel} = k(|\mathbf{R}_{i+1} - \mathbf{R}_i| - |\mathbf{R}_i - \mathbf{R}_{i-1}|) \hat{\boldsymbol{\tau}}_i \quad (2.12)$$

This decoupling of shape optimization (perpendicular) from spacing control (parallel) is the ‘‘nudging’’ that gives the method its name.

The spring constant  $k$  controls image spacing. Energy-weighted springs [52] replace the uniform  $k$  with image-dependent values  $k_i$  that increase near the energy maximum, concentrating resolution where it matters most for the barrier height while allowing wider spacing in the flat approach regions.

The tangent direction  $\hat{\boldsymbol{\tau}}_i$  enters every projection in the NEB force, so errors in the tangent propagate into the path shape. The simplest estimate, bisecting the vectors to the two neighbors,  $(\boldsymbol{\tau}_i^+ + \boldsymbol{\tau}_i^-)/2$  with  $\boldsymbol{\tau}_i^{\pm} = \mathbf{R}_{i\pm 1} - \mathbf{R}_i$ , breaks down at energy extrema along the path. At a local maximum, the two neighbors are both downhill but in different directions, and their average can point perpendicular to the path rather than along it, producing visible kinks. The *improved tangent* estimate [53] fixes this by selecting the tangent from the higher-energy neighbor:

$$\hat{\boldsymbol{\tau}}_i = \begin{cases} \boldsymbol{\tau}_i^+ & \text{if } V_{i+1} > V_i > V_{i-1} \\ \boldsymbol{\tau}_i^- & \text{if } V_{i+1} < V_i < V_{i-1} \\ \text{energy-weighted bisection} & \text{otherwise} \end{cases} \quad (2.13)$$

When the energy is monotonically increasing or decreasing through image  $i$ , the tangent points toward the uphill neighbor. When image  $i$  sits at a local extremum (the ‘‘otherwise’’ case), an energy-weighted average smoothly interpolates between the two directions. The stability condition for the NEB requires that the parallel spring force be bounded by the product of the perpendicular curvature and the image spacing; the bisection tangent violates this at large  $P$ , while the improved tangent does not.

#### 2.4.2 The Climbing Image and Its Connection to Minimum Mode Following

The standard NEB converges to a discretized MEP but does not place an image exactly at the saddle point. The *climbing image* (CI-NEB) modification [34, 54] promotes the highest-energy image to saddle-point-seeking behavior by removing its spring force and inverting the parallel component of the true force:

$$\mathbf{F}_{i_{\max}}^{\text{CI}} = -\nabla V(\mathbf{R}_{i_{\max}}) + 2[\nabla V(\mathbf{R}_{i_{\max}}) \cdot \hat{\boldsymbol{\tau}}_{i_{\max}}] \hat{\boldsymbol{\tau}}_{i_{\max}} \quad (2.14)$$

This image minimizes energy perpendicular to the path tangent while maximizing along it, which is precisely the condition for a first-order saddle point. Compare Eq. 2.14 to the dimer translational force (Eq. 2.8 with  $C < 0$ ):

$$\mathbf{F}^{\dagger} = \mathbf{F}(\mathbf{R}) - 2[\mathbf{F}(\mathbf{R}) \cdot \hat{\mathbf{N}}] \hat{\mathbf{N}} \quad (2.15)$$

The dimer method and the climbing image NEB (CI-NEB) are intricately linked. Both employ Householder reflections of the form:

$$\mathbf{F}^{\dagger} = \mathbf{F} - 2(\mathbf{F} \cdot \hat{\mathbf{v}}) \hat{\mathbf{v}} \quad (2.16)$$

The only difference lies in the source of the distinguished direction  $\hat{\mathbf{v}}$ :

**Dimer** (Eq. 2.8):  $\hat{\mathbf{v}} = \hat{\mathbf{N}}$ , the minimum mode derived directly from finite-difference curvature.

**CI-NEB** (Eq. 2.14):  $\hat{\mathbf{v}} = \hat{\boldsymbol{\tau}}_{i_{\max}}$ , the path tangent estimated from neighboring images.

This structural identity admits a precise geometric interpretation. The dimer (two images symmetrically displaced about a midpoint) acts as a truncated, free-ended chain. The midpoint plays the role of the climbing image, and the two endpoints provide the curvature information that determines the climbing direction. Extending this to a full chain of  $P$  images with fixed endpoints recovers the NEB. Conversely, truncating the NEB to three free-ended images recovers the dimer. Both methods converge to the exact same saddle point when the minimum mode aligns with the path tangent ( $\hat{\mathbf{N}} \approx \hat{\boldsymbol{\tau}}$ ), a commonality exploited in the OCI-NEB [11, 54].

Section 4 develops the Bayesian optimization framework that unifies GP-accelerated versions of these three methods.

Algorithm 3 summarizes the NEB iteration with optional climbing image activation. The NEB’s cost is dominated by the force evaluations at each image, with typical runs requiring  $P \sim 10$  images and 20 to 50 iterations. This makes NEB a natural candidate for GP acceleration, as we discuss in Section 6.

---

### Algorithm 3: Nudged elastic band with climbing image

---

**Input:** Initial chain  $\{\mathbf{R}_0, \dots, \mathbf{R}_P\}$ , spring constant  $k$ , CI threshold  $\epsilon_{CI}$ , convergence tolerance  $\epsilon_{tol}$

**Output:** converged MEP  $\{\mathbf{R}_0, \dots, \mathbf{R}_P\}$

```

1 CI ← false;
2 repeat
3   Evaluate  $V(\mathbf{R}_i), \mathbf{F}(\mathbf{R}_i)$  at all movable images;
4   for each image  $i = 1, \dots, P - 1$  do
5     Compute tangent  $\hat{\boldsymbol{\tau}}_i$  (Eq. 2.13);
6     if CI is true and  $i = i_{\max}$  then
7        $\mathbf{F}_i \leftarrow -\nabla V + 2(\nabla V \cdot \hat{\boldsymbol{\tau}}_i)\hat{\boldsymbol{\tau}}_i$ ;
8     else
9        $\mathbf{F}_i^\perp \leftarrow -\nabla V + (\nabla V \cdot \hat{\boldsymbol{\tau}}_i)\hat{\boldsymbol{\tau}}_i$ ;
10       $F_i^s \leftarrow k(|\mathbf{R}_{i+1} - \mathbf{R}_i| - |\mathbf{R}_i - \mathbf{R}_{i-1}|)$ ;
11       $\mathbf{F}_i \leftarrow \mathbf{F}_i^\perp + F_i^s \hat{\boldsymbol{\tau}}_i$ ;
12    end
13  end
14  Update all images  $\mathbf{R}_i \leftarrow \mathbf{R}_i + \Delta t \mathbf{F}_i$ ;
15  if CI is false and  $\max_i \|\mathbf{F}_i\| < \epsilon_{CI}$  then
16    CI ← false;
17     $i_{\max} \leftarrow \arg \max_i V(\mathbf{R}_i)$ ;
18  end
19 until  $\max_i \|\mathbf{F}_i\| < \epsilon_{tol}$ ;
```

---

## 3 Gaussian Process Regression

### 3.1 What the Surrogate Must Provide

The surrogate model must interpolate a small, incrementally growing set of energy and force data, provide calibrated uncertainty for active learning, and remain cheap enough that fitting and querying costs far less than the electronic structure call it replaces. Gaussian process regression satisfies all three. This section develops the GP from the perspective of building and using the surrogate, covering what quantities need to be computed, how they connect to the physics, and where the bottlenecks arise. We refer readers to Rasmussen and Williams [55] and Gramacy [27] for the mathematical foundations. As noted earlier, Deringer, Bartok, and Csanyi [17] has a detailed review of GPR in atomistic simulation from a global MLIP view, including structural descriptors (SOAP, ACE), sparse approximations, and validation methodology. That review treats the GP as a tool for building global machine-learned potentials from large databases; the present treatment focuses on the complementary regime of local surrogates built on the fly from tens of data points. The key distinction is hyperparameter management: MLIP approaches optimize hyperparameters once on a large training set and fix them, while the local GP re-optimizes at every step as the training set grows, requiring trust regions and active data selection to maintain stability.

The PES is modeled as a Gaussian process, which means that the energy values at any finite collection of configurations follow a multivariate normal (MVN) distribution [27]. The correlations between configurations

are encoded in a kernel  $k(\mathbf{x}, \mathbf{x}')$ , and the prior mean is set to zero (the constant kernel offset absorbs the baseline energy):

$$f(\mathbf{x}) \sim \mathcal{GP}(0, k(\mathbf{x}, \mathbf{x}')) \tag{3.1}$$

Before seeing any data, the PES is assumed to be drawn from a distribution over functions whose smoothness and amplitude are governed entirely by  $k$ . For molecular PES this assumption has a theoretical justification beyond convenience. Near a pronounced global minimum, the vibrational degrees of freedom contribute additively to the potential energy, and by the central limit theorem these many contributions lead the PES on a random coordinate frame to appear approximately Gaussian [7, 11]. Thus the GP prior forms a reasonable model for the local structure of the PES in the neighborhoods that matter for saddle point searches.

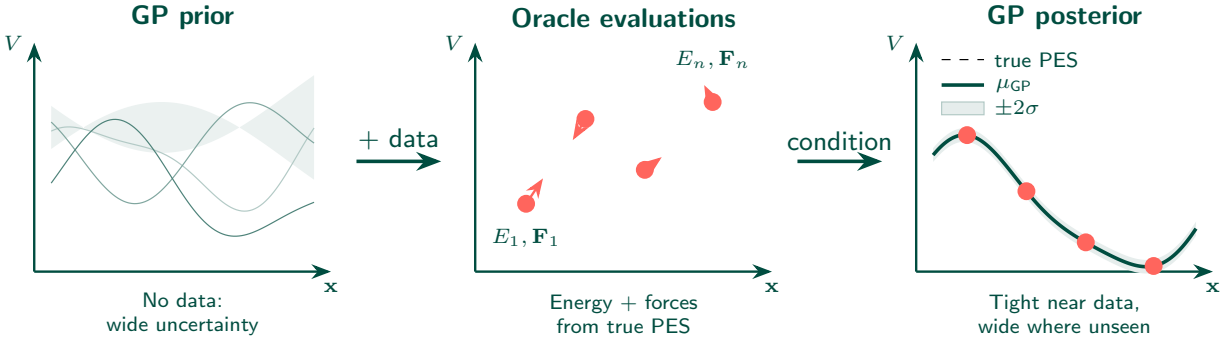


**Figure 2.** GP conditioning in three panels. (Left) Before any data, the prior (Eq. 3.1) admits a wide family of smooth functions. (Center) Oracle evaluations supply energies and forces at selected configurations. (Right) Conditioning on the data collapses the posterior near training points while preserving wide uncertainty elsewhere; the posterior mean serves as the surrogate surface  $V_{GP}$ .

After observing  $M$  data points  $\mathbf{y} = [y_1, \dots, y_M]^T$  at inputs  $\mathbf{X} = [\mathbf{x}_1, \dots, \mathbf{x}_M]$ , the joint distribution of the training observations and a new query point  $\mathbf{x}_*$  is written as a single MVN. Let  $[\mathbf{K}]_{ij} = k(\mathbf{x}_i, \mathbf{x}_j)$  be the kernel matrix over training points,  $[\mathbf{k}_*]_i = k(\mathbf{x}_i, \mathbf{x}_*)$  the cross-covariance with the query, and  $k_{**} = k(\mathbf{x}_*, \mathbf{x}_*)$ :

$$\begin{bmatrix} \mathbf{y} \\ f(\mathbf{x}_*) \end{bmatrix} \sim \mathcal{N}\left(\mathbf{0}, \begin{bmatrix} \mathbf{K} + \sigma_n^2 \mathbf{I} & \mathbf{k}_* \\ \mathbf{k}_*^T & k_{**} \end{bmatrix}\right) \tag{3.2}$$

Conditioning this joint distribution on the observed values  $\mathbf{y}$  gives the predictive distribution at  $\mathbf{x}_*$ , which is again Gaussian with mean and variance:

$$\bar{f}(\mathbf{x}_*) = \mathbf{k}_*^T (\mathbf{K} + \sigma_n^2 \mathbf{I})^{-1} \mathbf{y} \tag{3.3}$$

$$\text{var}[f(\mathbf{x}_*)] = k_{**} - \mathbf{k}_*^T (\mathbf{K} + \sigma_n^2 \mathbf{I})^{-1} \mathbf{k}_* \tag{3.4}$$

The posterior mean (Eq. 3.3) coincides with the kernel ridge regression (KRR) estimator with regularization  $\sigma_n^2$  [55], but the GP additionally provides the predictive variance (Eq. 3.4), which is the basis for the acquisition criterion in Section 6.

The mean is the surrogate’s prediction; the variance measures how much information the training set carries about  $\mathbf{x}_*$ . Near observed data, the variance drops to the noise floor  $\sigma_n^2$ . Far from observed data, it approaches the prior variance  $k_{**}$ . This variance structure is the basis for the acquisition criterion: the point of highest variance is, in the GP’s own assessment, the most informative place to sample next.

The interaction between these two quantities during a search is illustrated by the following progression. In the first few iterations, the GP has little data and the variance is large everywhere except at the evaluated configurations (Figure 3, top-left panel). The surrogate prediction is correspondingly uncertain, and the trust region (Section 5.2) constrains the optimizer to small steps. As data accumulates, the variance shrinks in the neighborhood of the reaction path (Figure 4) and the surrogate becomes a faithful replica of the true PES in that local region (Figure 3, bottom panels). The optimizer can now take longer steps on the cheap surrogate,

and the active learning criterion directs the next expensive evaluation to the frontier where the variance is still large. This feedback between uncertainty, data acquisition, and optimization step length accounts for the roughly ten-fold savings in electronic structure calls.

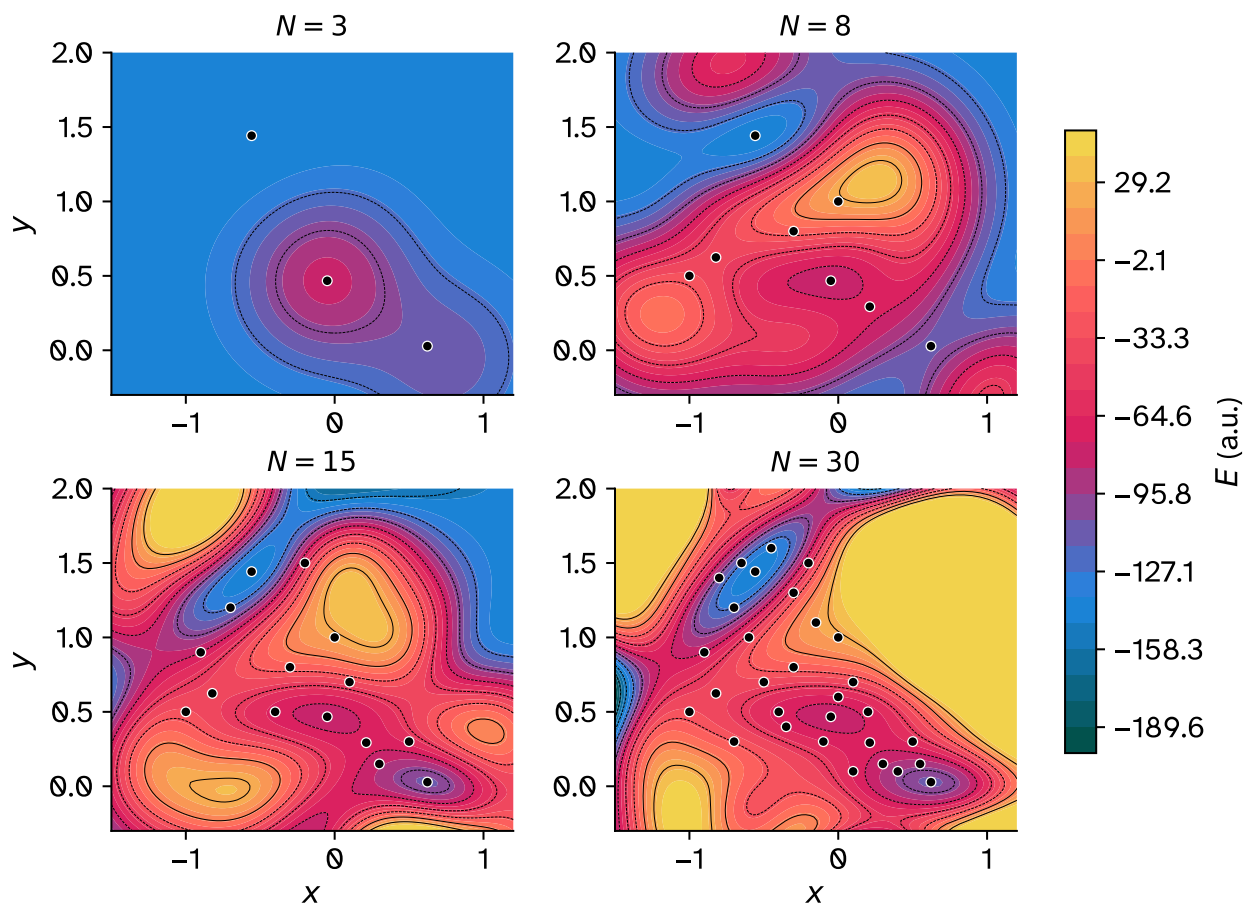


**Figure 3.** GP surrogate fidelity as a function of training set size on the Muller-Brown surface. Each panel shows the GP posterior mean contours after training on  $M = 5, 15, 30, 50$  Latin hypercube-sampled configurations (black dots). With 5 points the surrogate captures only crude basin structure; by 30 points the contours closely match the true PES (Figure 12) in the sampled region.

Both expressions involve the matrix inverse  $(\mathbf{K} + \sigma_n^2 \mathbf{I})^{-1}$ , which is never formed explicitly. Instead, the Cholesky factorization  $\mathbf{K} + \sigma_n^2 \mathbf{I} = \mathbf{L}\mathbf{L}^T$  is computed once at  $\mathcal{O}(M^3)$  cost, and the weight vector  $\boldsymbol{\alpha} = (\mathbf{K} + \sigma_n^2 \mathbf{I})^{-1} \mathbf{y}$  is obtained by forward-back substitution against  $\mathbf{L}$ :

$$\mathbf{L}\mathbf{z} = \mathbf{y}, \quad \mathbf{L}^T \boldsymbol{\alpha} = \mathbf{z} \quad (3.5)$$

Each new prediction then costs  $\mathcal{O}(M^2)$  for the matrix-vector product  $\mathbf{k}_*^T \boldsymbol{\alpha}$ . For added robustness the implementation in `chemgp-core` uses a Cholesky factorization wrapped in a guarded routine that applies exponentially increasing jitter when the matrix is nearly singular, starting at  $10^{-8} \max(\text{diag}(\mathbf{K}))$  and increasing by a factor of 10 per attempt. This adaptive jitter handles the rank deficiency that arises naturally from molecular kernels, where the feature space dimension (number of atom pairs) can be smaller than the coordinate dimension  $3N$ . With  $M \sim 30$ , the factorization is instantaneous; the cost only becomes relevant when derivative observations are included (Section 3.2), which inflate the effective training set size.

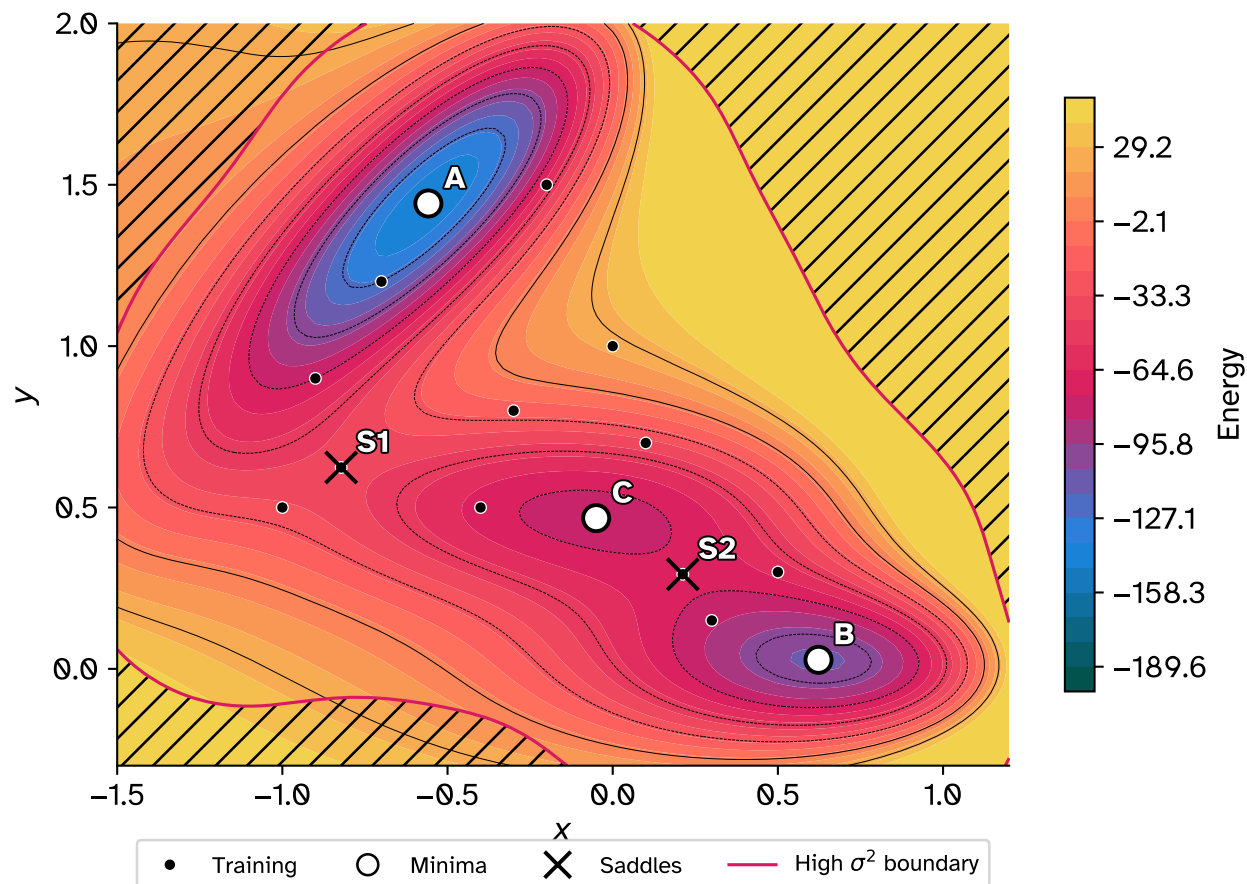


**Figure 4.** GP predictive variance on the Muller-Brown surface after 20 training evaluations clustered near minimum A and saddle S1 (black dots). The variance is near zero close to training data and grows with distance, reaching a maximum (coral diamond) in the unexplored region. This variance landscape is the basis for active learning: the next electronic structure evaluation is placed where the GP is least certain.

### 3.2 Regression with Derivative Observations

Every electronic structure evaluation returns not just the energy but also the atomic forces (the negative gradient of the PES) at negligible extra cost. For a system of  $N$  atoms, each evaluation therefore provides  $1 + 3N$  scalar constraints on the PES: one energy and  $3N$  force components. A 10-atom system yields 31 constraints per call, so  $M = 30$  evaluations already give 930 independent observations, enough to pin down a local region of the PES with high fidelity. Training the GP on energies alone would discard all but  $1/(1 + 3N)$  of this information [56], requiring an impractically large number of evaluations to achieve the same coverage. The GP accommodates derivative observations naturally because differentiation is a linear operation on the kernel [57]:

$$\text{cov} \left[ f(\mathbf{x}), \frac{\partial f}{\partial x'_j} \right] = \frac{\partial k(\mathbf{x}, \mathbf{x}')}{\partial x'_j} \quad (3.6)$$

$$\text{cov} \left[ \frac{\partial f}{\partial x_i}, \frac{\partial f}{\partial x'_j} \right] = \frac{\partial^2 k(\mathbf{x}, \mathbf{x}')}{\partial x_i \partial x'_j} \quad (3.7)$$

In the implementation, the kernel matrix acquires a  $2 \times 2$  block structure over the energy and force observations:

$$\mathbf{K}_{\text{full}} = \begin{bmatrix} \mathbf{K}_{EE} & \mathbf{K}_{EF} \\ \mathbf{K}_{FE} & \mathbf{K}_{FF} \end{bmatrix} \quad (3.8)$$

where the blocks are the energy-energy ( $M \times M$ ), energy-force ( $M \times MD$ ), and force-force ( $MD \times MD$ ) covariances with  $D = 3N$ . The full matrix is  $M(1+D) \times M(1+D)$ , and the Cholesky cost becomes  $\mathcal{O}(M^3 D^3)$ . Figure 5 shows this block structure schematically. As a concrete example, a 10-atom molecule with  $M = 30$  accumulated configurations gives a  $930 \times 930$  matrix. This is still fast, but growth is cubic, which is why the data management strategies in Section 8 become necessary for longer searches.

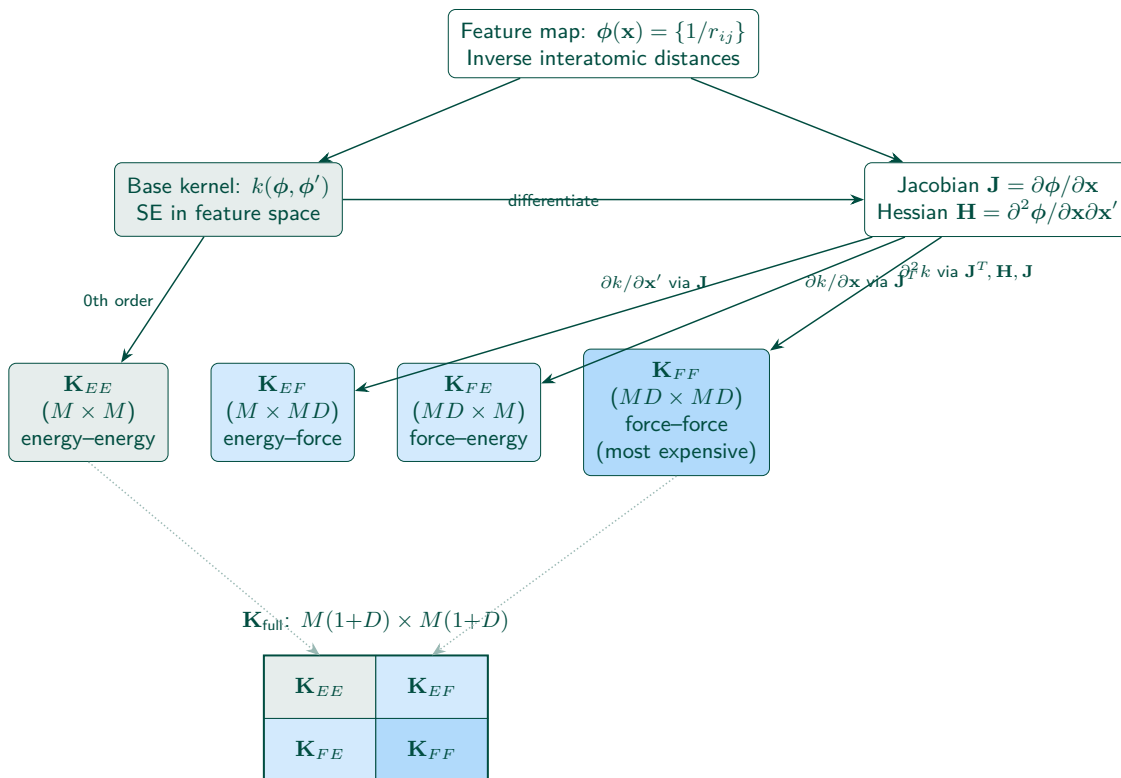


**Figure 5.** Block structure of the full covariance matrix  $\mathbf{K}_{\text{full}}$ . The base kernel in feature space generates four Cartesian-space blocks through differentiation via the feature Jacobian  $\mathbf{J}$ . Darker shading indicates higher computational cost.

Energies and forces have different magnitudes and units, so separate noise variances  $\sigma_E^2$  and  $\sigma_F^2$  are assigned to each block. Because the electronic structure data is deterministic (no stochastic noise), these are not physical noise parameters but Tikhonov regularizers; they are set to small values ( $\sim 10^{-8}$ ) to keep the matrix well-conditioned. The ratio  $\sigma_E^2/\sigma_F^2$  controls the relative weight the GP places on matching energies versus forces, and incorrect specification of this ratio degrades surrogate quality.

Including forces provides substantial payoff. Each evaluation contributes  $1 + 3N$  scalar constraints, so  $M = 30$  calls for a 10-atom system yield 930 constraints, enough to resolve the PES locally without needing a large training set. This information density is the core reason the local surrogate strategy works with so few evaluations. It also imposes a stringent requirement on the kernel implementation, namely that the derivative blocks (Eqs. 3.6–3.7) must be computed analytically, as discussed in detail in Section 3.3.1. The inverse-distance kernel provides the required invariance, but the composition of the inverse, the norm, and the exponential makes it particularly sensitive to numerical noise in the derivative blocks, and the production C++ code (`gpr\optim`) is heavily optimized around this bottleneck.

### 3.3 Covariance Functions for Molecular Systems

The kernel encodes the assumption about which configurations should have similar energies. If  $k(\mathbf{x}, \mathbf{x}')$  is large, the GP expects the energies at  $\mathbf{x}$  and  $\mathbf{x}'$  to be correlated, and it will interpolate smoothly between them; if  $k$  is small, the GP treats them as independent. For molecular systems, the kernel must respect the physical symmetries of the PES, namely rotational and translational invariance, and ideally also permutation invariance for identical atoms. A kernel operating directly on Cartesian coordinates  $\mathbf{x} \in \mathbb{R}^{3N}$  fails the first requirement immediately, because rotating all atoms changes  $\mathbf{x}$  but not  $V(\mathbf{x})$ , so two identical configurations related by a rigid rotation would appear dissimilar to the GP.

Global MLIP frameworks solve this with high-dimensional structural descriptors that project the atomic environment onto a rotationally invariant representation. SOAP (Smooth Overlap of Atomic Positions) [58]

constructs a local neighbor density around each atom, expands it in a radial-spherical basis, and forms the power spectrum, a descriptor that is automatically invariant to rotations and permutations of like atoms. The body-order interpretation is illuminating. A linear SOAP kernel is a three-body model (each descriptor entry involves a central atom and a pair of neighbors), and raising the kernel to the power  $\zeta$  yields a  $(2\zeta + 1)$ -body model [17]. The ACE (Atomic Cluster Expansion) [59] framework generalizes this construction to arbitrary body orders in a systematic manner. These descriptors are engineered to resolve fine structural differences across all of configuration space, with convergence parameters (radial and angular truncation orders, cutoff radius) that control the trade-off between accuracy and cost.

For the *local* surrogates discussed in this work [11, 60–63], that level of sophistication is unnecessary and carries a cost that defeats the purpose. The GP only needs to distinguish configurations in a small neighborhood of the reaction path, where the molecular connectivity does not change and pairwise distance information captures the relevant variation. Computing SOAP descriptors and their analytic derivatives for each of the  $M \sim 30$  training points would add overhead comparable to the GP algebra itself, erasing the wall-time savings. More fundamentally, the derivative blocks (Section 3.2) require second-order kernel derivatives with respect to Cartesian coordinates, and the composition of a high-dimensional descriptor with the kernel introduces an additional layer of chain-rule complexity that must be handled analytically to avoid numerical noise (Section 3.3.1). The inverse-distance feature map [29]  $\phi_{ij} = 1/r_{ij}$  is the simplest descriptor that provides rotational and translational invariance while admitting tractable analytical derivatives. The idea of using inverse interatomic distances as molecular features has roots in the Coulomb matrix representation [64].

A pairwise-distance representation is preferred for local surrogates. The stationarity of the SE kernel (the assumption that the covariance depends only on the *difference* between inputs) means the GP assumes uniform fluctuations across its domain. In Cartesian coordinates, this assumption is catastrophically wrong for a PES because the energy varies slowly near a minimum but changes by electron-volts over sub-Angstrom displacements near a repulsive wall. The GP would need an impossibly short length scale to capture the repulsive region, which would destroy its interpolation ability in the flat valley. By transforming to inverse interatomic distances, the energy landscape is effectively *preconditioned*. The  $1/r$  map compresses the repulsive region (where  $r$  is small and  $1/r$  changes slowly in relative terms) and stretches the long-range region (where small changes in  $r$  produce large changes in  $1/r$ ). The result is a feature space where the PES has more uniform curvature, and the stationary kernel becomes a reasonable approximation. This is the core reason the inverse-distance kernel outperforms Cartesian kernels for molecular systems, even when both are given the same training data.

### 3.3.1 The Inverse-Distance Squared Exponential Kernel

The solution is to work with internal features that are inherently invariant. The inverse interatomic distance provides a physically motivated feature:

$$\phi_{ij}(\mathbf{x}) = \frac{1}{r_{ij}(\mathbf{x})} = \frac{1}{\sqrt{\sum_{d=1}^3 (x_{i,d} - x_{j,d})^2}} \quad (3.9)$$

The inverse-distance squared exponential (SE) kernel is then:

$$k(\mathbf{x}, \mathbf{x}') = \sigma_c^2 + \sigma_f^2 \exp \left( -\frac{1}{2} \sum_i \sum_{j>i} \left( \frac{\phi_{ij}(\mathbf{x}) - \phi_{ij}(\mathbf{x}')}{l_{\phi(i,j)}} \right)^2 \right) \quad (3.10)$$

where:

- $\sigma_f^2$  is the signal variance, controlling the amplitude of the GP prior.
- $\sigma_c^2$  is a constant offset, accounting for the mean energy level.
- $l_{\phi(i,j)}$  are length-scale parameters, one per atom-pair type  $\phi(i,j)$ , controlling how rapidly the covariance decays as the inverse distances change.

The  $1/r_{ij}$  feature has three properties that matter for the GP. First, it is invariant under rigid-body motions, so the covariance between two configurations is unaffected by how they are oriented in the lab frame. Second,

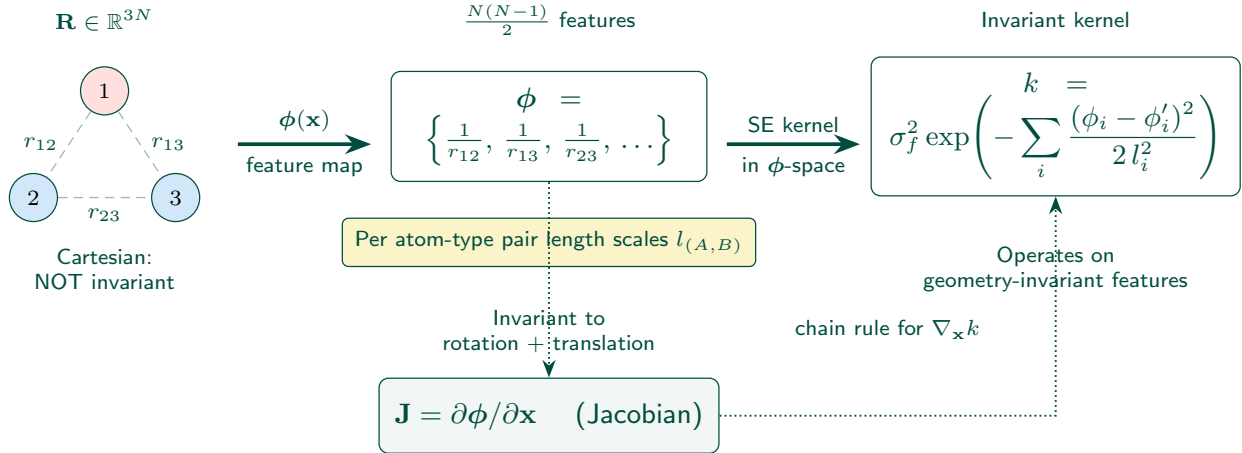


**Figure 6.** The inverse-distance feature map. Cartesian coordinates ( $\mathbb{R}^{3N}$ , not invariant) are mapped to pairwise inverse distances ( $N(N-1)/2$  features, invariant to rotation and translation). The SE kernel operates in this feature space. The Jacobian  $\mathbf{J} = \partial\phi/\partial\mathbf{x}$  propagates through the kernel via the chain rule to produce the derivative blocks needed for force predictions.

and more subtle, the divergence as  $r_{ij} \rightarrow 0$  creates a natural barrier in feature space: two configurations where any atom pair has a markedly different close-contact distance are mapped to widely separated points in the inverse-distance representation. The GP, which interpolates smoothly in feature space, cannot interpolate *through* this barrier. This means the surrogate will never predict a smooth, low-energy path through a repulsive wall, even when it has no training data in that region. The divergence does the work that an explicit repulsive prior would otherwise have to do. Third, the number of features  $N_{\text{pairs}} = N(N-1)/2$  is fixed for a given molecular formula regardless of the spatial arrangement, so the kernel is always well-defined. This is a practical advantage over radial-cutoff descriptors, where the number of neighbors within a fixed radius can vary between configurations, creating a dimension mismatch that requires padding or variable-length handling.

The length-scale parameters  $l_{\phi(i,j)}$  control the GP’s sensitivity to changes in each interatomic distance. A short length scale for a particular atom pair means the GP treats small changes in that pair’s inverse distance as significant (i.e., the pair is “stiff” in the model’s view); a long length scale means the GP is insensitive to that pair. In practice, the hyperparameter optimization (Section 3.4) learns these from the data, and bonds that are actively breaking or forming during the reaction acquire short length scales, while spectator bonds that barely change acquire long ones. This automatic relevance determination is what allows the GP to focus its limited training data on the degrees of freedom that matter for the particular transition being studied.

The constant offset  $\sigma_c^2$  is fixed rather than optimized alongside the other hyperparameters, since with the small training sets typical of on-the-fly searches ( $M \sim 10-50$ ), the marginal likelihood cannot reliably distinguish  $\sigma_c^2$  from  $\sigma_f^2$ . A default of  $\sigma_c^2 = 1.0$  works well for molecular systems with eV-scale energies; for 2D model surfaces (LEPS, Muller-Brown) where energies are already centered near zero,  $\sigma_c^2 = 0.0$  avoids introducing a superfluous degree of freedom. Without it, the GP prior mean is zero, and the posterior mean would revert to zero far from the training data. The constant kernel adds a baseline covariance that is independent of configuration, which allows the GP to represent a nonzero mean energy level. In practice, this absorbs the large absolute energy that is common in electronic structure calculations, so the GP only needs to model the *relative* energy variations. Because the constant kernel contributes only to the energy-energy block of the covariance matrix (its derivative with respect to any coordinate is zero), it does not affect force predictions and carries no risk of corrupting the gradient information that drives the optimization.

The kernel derivative blocks needed for Eq. 3.8 are obtained by applying the chain rule through the feature map:

$$\frac{\partial k}{\partial x_a} = \sum_{(i,j)} \frac{\partial k}{\partial \phi_{ij}} \frac{\partial \phi_{ij}}{\partial x_a} \tag{3.11}$$

where  $\partial\phi_{ij}/\partial x_a$  is the Jacobian of the inverse-distance features with respect to the Cartesian coordinates. For the SE kernel, the partial derivative with respect to a feature is:

$$\frac{\partial k}{\partial \phi_{ij}} = -\sigma_f^2 \frac{\phi_{ij}(\mathbf{x}) - \phi_{ij}(\mathbf{x}')}{l_{\phi(i,j)}^2} \exp(\dots) \quad (3.12)$$

The second-order derivatives  $\partial^2 k / \partial x_a \partial x'_b$  follow analogously through the Hessian of the feature map. In the implementation, the Jacobian of the inverse-distance features has the explicit form:

$$\frac{\partial \phi_{ij}}{\partial x_{i,a}} = -\frac{x_{i,a} - x_{j,a}}{r_{ij}^3}, \quad \frac{\partial \phi_{ij}}{\partial x_{j,a}} = \frac{x_{i,a} - x_{j,a}}{r_{ij}^3} \quad (3.13)$$

and the force-force block of the covariance matrix is assembled via the chain rule as  $\mathbf{K}_{FF} = \mathbf{J}_1^T \mathbf{H}_{\text{feat}} \mathbf{J}_2$ , where  $\mathbf{H}_{\text{feat}}$  is the Hessian of the kernel in feature space and  $\mathbf{J}_1, \mathbf{J}_2$  are the Jacobians at the two configurations. We stress that these derivatives *must* be computed analytically. Using nested automatic differentiation (e.g., dual-number propagation through the inverse-distance computation and the kernel exponential) introduces numerical noise of order  $\sim 10^{-8}$  in the force-force block. This is the same magnitude as the Tikhonov regularizer  $\sigma_F^2$ , so the assembled covariance matrix loses positive definiteness after approximately 10 training points. The problem is intrinsic to the composition of the inverse ( $1/r$ ), the Euclidean norm ( $\sqrt{\cdot}$ ), and the exponential in the SE kernel, where each layer of dual-number arithmetic accumulates truncation error that the subsequent layer amplifies. The MATLAB, Rust, and C++ implementations all use fully analytical derivatives for this reason. In production codes [38], the derivative computation is further optimized by pre-computing and caching the inverse-distance Jacobians, vectorizing the block assembly with Eigen array operations, and zeroing covariance entries below machine epsilon to prevent noise accumulation. This level of optimization is necessary because the derivative block computation dominates the wall time of the GP update step. In general the ill-conditioning due to the addition of derivative observations has been noted across disciplines [65, 66].

### 3.4 Hyperparameter Optimization

The GP model has a set of free parameters  $\boldsymbol{\theta} = \{\sigma_f^2, \sigma_c^2, \{l_{\phi(i,j)}\}, \sigma_E^2, \sigma_F^2\}$  that must be determined from the data, and have no connection to the bond lengths [38]. We optimize these by maximizing the log marginal likelihood:

$$\log p(\mathbf{y} | \mathbf{X}, \boldsymbol{\theta}) = -\frac{1}{2} \mathbf{y}^T \mathbf{K}_{\boldsymbol{\theta}}^{-1} \mathbf{y} - \frac{1}{2} \log |\mathbf{K}_{\boldsymbol{\theta}}| - \frac{n}{2} \log(2\pi) \quad (3.14)$$

where  $\mathbf{K}_{\boldsymbol{\theta}}$  is the full covariance matrix (including noise) and  $n$  is the total number of scalar observations. The first term penalizes poor data fit, the second penalizes model complexity (large determinant), and the third is a normalization constant. The gradient with respect to each hyperparameter is available in closed form:

$$\frac{\partial \log p}{\partial \theta_j} = \frac{1}{2} \text{tr} \left[ (\boldsymbol{\alpha} \boldsymbol{\alpha}^T - \mathbf{K}_{\boldsymbol{\theta}}^{-1}) \frac{\partial \mathbf{K}_{\boldsymbol{\theta}}}{\partial \theta_j} \right] \quad (3.15)$$

where  $\boldsymbol{\alpha} = \mathbf{K}_{\boldsymbol{\theta}}^{-1} \mathbf{y}$ . Maximizing the MLL is equivalent to computing the maximum a posteriori (MAP) estimate of the hyperparameters under a flat (improper) prior. With few training points the MLL landscape is flat or multimodal, and the MAP estimate is poorly determined. Two failure modes result: the signal variance  $\sigma_f^2$  can grow without bound (the data-fit term in Eq. 3.14 dominates the complexity penalty), and the full hyperparameter vector can oscillate between competing MLL modes as each new data point shifts the landscape. Both pathologies produce surrogates that are unrelated to the true PES and must be regularized; Section 8.2 addresses this.

Both the Rust code for this tutorial and the production C++ code use the scaled conjugate gradient (SCG) optimizer [67], which exploits the analytical gradient of the marginal likelihood (Eq. 3.15). The hyperparameters are re-optimized at every outer iteration, which means the marginal likelihood landscape changes as data accumulates. This re-optimization is both the source of the GP's adaptivity and, as discussed in Section 8.2, a potential source of instability.

The necessity of per-step hyperparameter optimization is a distinguishing feature of the local surrogate regime that sets it apart from global GP potentials. In MLIP frameworks, especially universal models [18] the kernel operates in a descriptor space (SOAP, ACE) whose structure already encodes the relevant chemical environment. The descriptors are designed so that the kernel length scale has a physical interpretation (the Gaussian mollification width  $\sigma_a$ , typically 0.3 Å for systems containing hydrogen and 0.5 Å for heavier elements) that is nearly universal across chemical systems. The practitioner fixes these hyperparameters a priori from physical reasoning and then builds the training set to achieve a target accuracy, rather than optimizing hyperparameters to match a fixed dataset. The regularization parameter is set to the estimated noise level of the training data, and data is added until the model reaches this noise floor. The problem is, as it were, “turned upside down”: instead of fitting hyperparameters to data, one chooses hyperparameters that encode prior physical knowledge and fits the *data* to the model.

This inversion is possible because the high-dimensional descriptor space absorbs most of the complexity that the hyperparameters would otherwise need to capture. The SOAP descriptor or higher order kernels [68], for instance, encodes three-body and higher correlations through its expansion in radial and angular basis functions, so a simple stationary kernel with fixed hyperparameters suffices to interpolate smoothly in descriptor space. By contrast, the inverse-distance kernel used here operates in a lower-dimensional pairwise feature space, and the length-scale parameters compensate for the missing higher-body information by adapting to the local PES region. As the search moves from a minimum through a transition region to a saddle point, the effective stiffness of the PES changes, and the length scales track this change. This is why re-optimization occurs at every step and why the hyperparameter instabilities of Section 8.2 arise: the optimization is chasing a moving target.

The effect of hyperparameter choice on the surrogate is illustrated in Figure 7, which shows 1D slices of the GP prediction on the Muller-Brown surface for a grid of length scale and signal variance values. A remark on the physical interpretation of the optimized hyperparameters is warranted. In some formulations, the length scales  $l_{\phi(i,j)}$  are expected to converge to quantities related to equilibrium bond lengths [62, 69, 70] or covalent radii, but this expectation lacks a first-principles justification [38]. One length scale per *atom-pair type* (e.g., one for all C–H pairs, one for all C–C pairs) is defined, and optimizing over all instances of that type in the training set yields a global, averaged stiffness for each interaction type that reflects the local PES region explored at the current stage of the search, not a fixed molecular property. The signal variance  $\sigma_f^2$  similarly does not correspond to a physical energy scale but controls the flexibility of the surrogate model. The disconnect is fundamental. The marginal likelihood (Eq. 3.14) is maximized, a statistical quantity that measures the model’s consistency with the observed data under a Gaussian assumption, and the resulting surrogate reproduces the true PES well enough that its stationary points approximate the true ones. The hyperparameters encode the GP’s many-body effects implicitly through a few parameters per pair type, and their numerical values are best understood as model-fitting artifacts rather than physical constants.

The signal variance  $\sigma_f^2$  can be handled in multiple ways. In this framework it is a free hyperparameter optimized by MLL, with a logarithmic barrier (Section 8.2) to prevent divergence. An alternative is to marginalize  $\sigma_f^2$  out under a conjugate inverse-gamma prior. The result is a Student’s t-process [71] whose predictive mean is identical to the GP’s but whose heavier-tailed variance produces more conservative uncertainty estimates; this has been applied to surrogate-accelerated NEB for surface catalysis [62]. Other kernels (e.g., Matern [72]) can each be made to work with appropriate tuning. The requirements are that the surrogate is locally faithful, that the uncertainty is calibrated well enough to guide sampling, and that the hyperparameters do not destabilize the model; the specific mechanism for achieving these is secondary.

### 3.4.1 Data-Dependent Initialization

Good initialization of the hyperparameters is critical for avoiding poor local optima. Following Gramacy [27], the signal variance and length scales are initialized from the data range:

$$\sigma_f^2 = \left( \Phi^{-1}(0.75) \cdot \frac{\text{range}(\mathbf{y})}{3} \right)^2 \tag{3.16}$$

$$l = \Phi^{-1}(0.75) \cdot \frac{\text{range}(\mathbf{X})}{3} \tag{3.17}$$

where  $\Phi^{-1}(0.75) \approx 0.6745$  is the 75th percentile of the standard normal, and  $\text{range}(\cdot)$  denotes the data range. This initialization places the GP in a reasonable regime where it can capture the variation in the data without overfitting. The sensitivity to these choices is demonstrated in Figure 7, and the corresponding NLL landscape (Figure S3) shows how the MAP optimum balances data fit against model complexity.

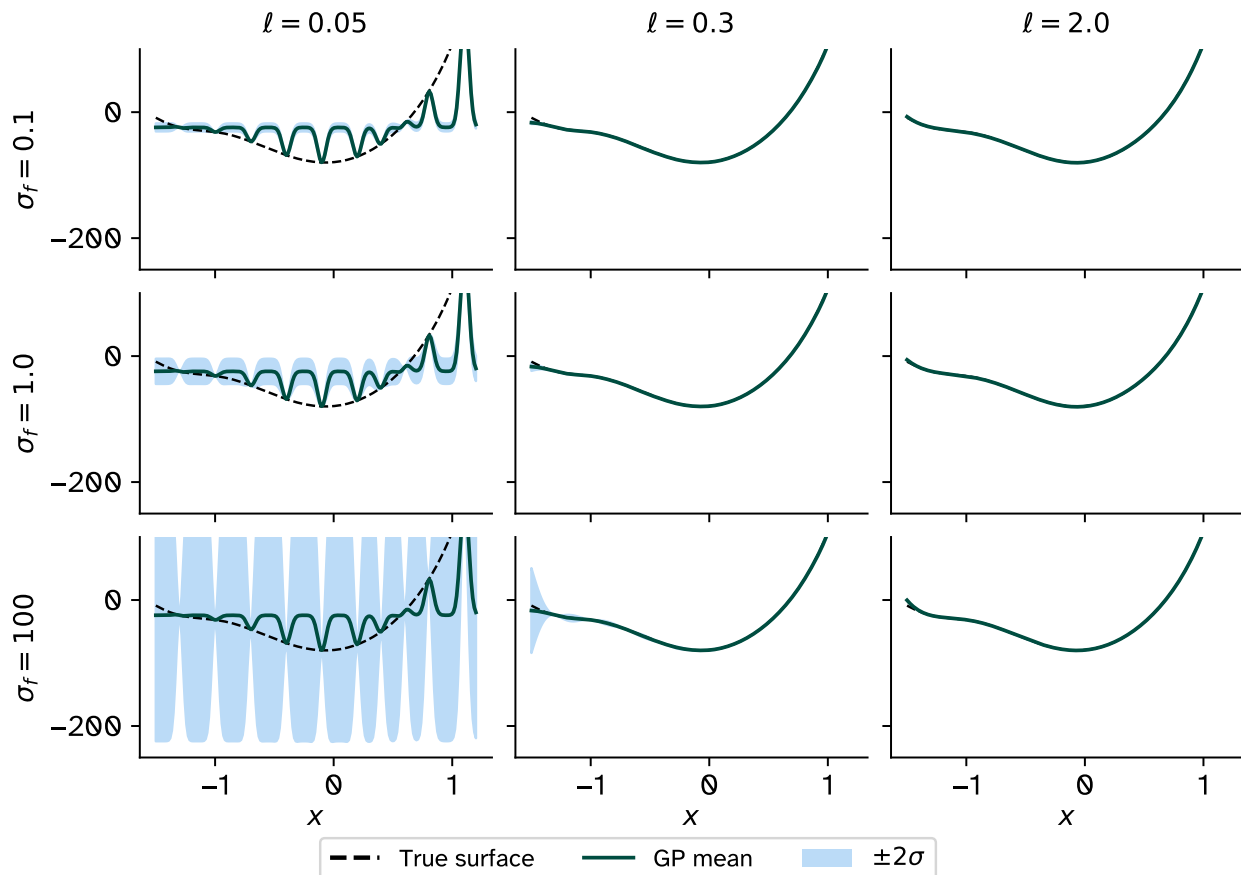


**Figure 7.** Hyperparameter sensitivity on the Muller-Brown surface. Each panel shows a 1D slice at  $y = 0.5$  with the true PES (black dashed), the GP posterior mean (teal), and the  $\pm 2\sigma$  confidence band (light blue), for nine combinations of length scale  $\ell \in \{0.05, 0.3, 2.0\}$  (columns) and signal variance  $\sigma_f \in \{0.1, 1.0, 100.0\}$  (rows). Small  $\ell$  produces noisy interpolation; large  $\ell$  over-smooths and misses barrier structure. The center cell ( $\ell = 0.3, \sigma_f = 1.0$ ) shows well-calibrated behavior where the confidence band tightly encloses the true surface near training data and widens appropriately in data-sparse regions.

## 4 The Bayesian Surrogate Loop: Anatomy of the Unified Framework

The preceding sections develop the GP as a regression tool: given training data, it produces a posterior mean (the surrogate surface) and a posterior variance (the uncertainty). What converts this into an optimization tool is the realization that both quantities feed naturally into an iterative decision loop. The posterior mean provides a cheap surface on which to run standard optimizers (L-BFGS, CG, NEB relaxation), and the posterior variance provides a criterion for when and where to request the next expensive electronic structure evaluation. This is a Bayesian optimization (BO) loop [27, 73, 74], adapted from the scalar setting (optimize an unknown function) to structured PES problems (find saddle points, minimum energy paths, and local minima) with gradient observations.

The abstraction that makes this unification possible is simple: the GP operates on configurations in  $\mathbb{R}^{3N}$  with associated energy and force observations. The GP does not know whether a state came from a dimer midpoint, a NEB image, or a minimization step. The same kernel, the same covariance algebra, the same

hyperparameter training applies regardless. Methods differ only in which optimizer produced the current geometry and which acquisition criterion selects the next one.

---

**Algorithm 4: Generic Bayesian surrogate loop for PES optimization**


---

**Input:** Initial configuration(s)  $\mathbf{X}_0$ , oracle  $V(\cdot)$ , convergence threshold  $\epsilon$

- 1 Evaluate oracle at  $\mathbf{X}_0$ ; initialize  $\mathcal{D} = \{(\mathbf{x}, V(\mathbf{x}), \nabla V(\mathbf{x}))\}$ ;
  - 2 **repeat**
  - 3     SELECT training subset  $\mathcal{S} \subseteq \mathcal{D}$ ;
  - 4     TRAIN hyperparameters  $\theta$  on  $\mathcal{S}$ ;
  - 5     BUILD prediction model from  $\mathcal{D}$  with  $\theta$ ;
  - 6     OPTIMIZE on surrogate  $V_{\text{GP}}$ : method-specific inner loop;
  - 7     CLIP proposed step via trust region;
  - 8     ACQUIRE: select next oracle point  $\mathbf{x}^*$  via criterion  $\alpha(\mathbf{x})$ ;
  - 9     Evaluate oracle at  $\mathbf{x}^*$ ;  $\mathcal{D} \leftarrow \mathcal{D} \cup \{(\mathbf{x}^*, V, \nabla V)\}$ ;
  - 10 **until**  $|\mathbf{F}(\mathbf{x}^*)| < \epsilon$ ;
- 

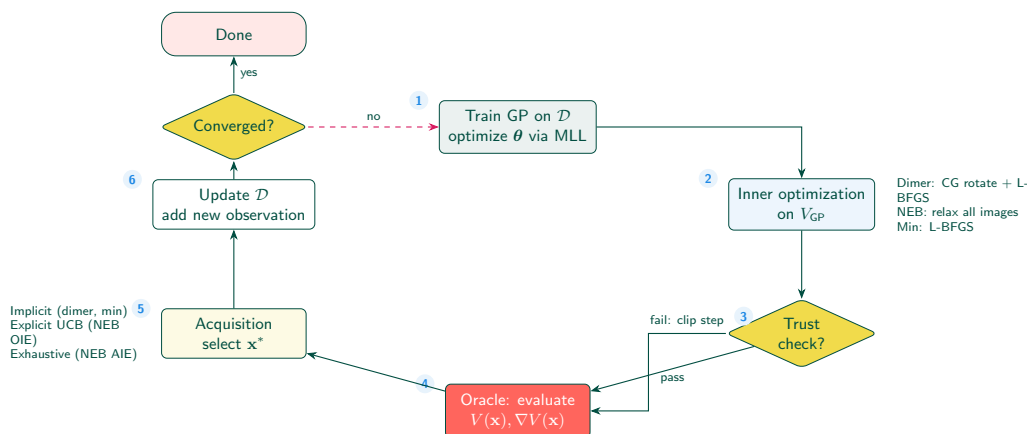


**Figure 8.** Visual overview of the Bayesian surrogate loop (Algorithm 4). Numbered steps proceed clockwise: (1) train the GP, (2) optimize on the surrogate, (3) check trust constraints, (4) evaluate the oracle, (5) select the next query point, (6) update the training set. The oracle (coral) is the only expensive step; all others operate on the cheap surrogate. Method-specific annotations indicate how each algorithm instantiates the inner optimization and acquisition steps.

Table 1 summarizes how each method instantiates Algorithm 4.

**Table 1.** Instantiation of Algorithm 4 across methods

Step	Minimization	GP-dimer	GP-NEB
1. Select subset	Global FPS	Global FPS	Per-bead FPS
2. Train $\theta$	SCG on MAP	SCG on MAP	SCG on MAP
3. Build model	Exact/RFF	Exact/RFF	Exact/RFF
4. Inner optimization	L-BFGS	CG rotate + L-BFGS	NEB relaxation
5. Trust clip	EMD/Euclidean	EMD	EMD
6. Acquisition	Implicit	Implicit	UCB (OIE) or exhaustive (AIE)

The inner optimization proposes configurations by running a standard optimizer on the surrogate surface. The surrogate is cheap, so the inner loop can run to convergence (or until the trust boundary is reached). Two quantities govern when the inner loop should terminate and when the oracle should be consulted. Both are derived from the GP posterior variance projected onto the subspace relevant to each method.

For saddle point methods (dimer, OT-GP dimer [OTGPD]) and NEB, the relevant uncertainty is the gradient variance perpendicular to a preferred direction  $\boldsymbol{\tau}$  (the dimer orient or the NEB path tangent):

$$\sigma_{\perp}(\mathbf{x}, \boldsymbol{\tau}) = \sqrt{\sum_{d=1}^D \text{var} \left[ \frac{\partial V_{\text{GP}}}{\partial x_d} \right]} (1 - \tau_d^2) \quad (4.1)$$

For minimization, no preferred direction exists and the total gradient uncertainty  $\sigma_g = \sqrt{\sum_d \text{var}[\partial V_{\text{GP}}/\partial x_d]}$  replaces  $\sigma_{\perp}$ .

The LCB [75, 76] convergence criterion augments the inner loop stopping rule to prevent premature convergence in uncertain regions:

$$\|\nabla V_{\text{GP}}\|_{\text{eff}} = \|\nabla V_{\text{GP}}\| + \kappa \cdot \sigma(\mathbf{x}, \boldsymbol{\tau}) \quad (4.2)$$

where  $\sigma$  is  $\sigma_{\perp}$  for saddle-point and NEB methods, or  $\sigma_g$  for minimization. The inner loop continues until  $\|\nabla V_{\text{GP}}\|_{\text{eff}}$  drops below the GP tolerance. When  $\kappa = 0$  this reduces to the standard gradient norm test. In the OTGPD variant the GP tolerance itself is adapted across outer iterations. When the true force is far from the convergence threshold the inner loop uses a loose tolerance (divisor of 2), accepting imprecise solutions on the surrogate and avoiding wasted inner steps on an inaccurate GP surface. As the true force approaches the threshold, the divisor ramps linearly to a configured maximum, tightening the inner convergence to match the accuracy the surrogate has attained. This schedule prevents the optimizer from overshooting on early, data-poor surrogates while still extracting full precision from well-trained models near convergence.

On the acquisition side, the NEB-OIE variant provides the clearest example of an explicit acquisition function. After inner relaxation, the UCB criterion [77] selects the unevaluated image with the highest combined score:

$$i^* = \arg \max_{i \in \mathcal{U}} [|\mathbf{F}_i^{\text{NEB}}| + \kappa \cdot \sigma_{\perp}(\mathbf{R}_i, \boldsymbol{\tau}_i)] \quad (4.3)$$

where  $\mathcal{U}$  is the set of unevaluated images. This balances exploitation (images with large NEB forces) against exploration (images with high uncertainty). When  $\kappa = 0$  the selection reduces to force-only (pure exploitation); the variance-only criterion (Eq. 6.1) is recovered in the  $\kappa \rightarrow \infty$  limit.

The dual of LCB convergence operates at the oracle level. A variance gate suppresses unnecessary oracle evaluations when the surrogate is already confident:

$$\text{skip oracle if } \sigma_{\perp}(\mathbf{x}, \boldsymbol{\tau}) < \sigma_{\text{gate}} \quad (4.4)$$

Three acquisition modes cover the methods in this review. *Implicit* acquisition (GP-minimize, GP-dimer, OTGPD) has no separate selection step: the inner loop proposes a configuration by optimizing on the surrogate, the trust region clips the step, and the oracle evaluates wherever the clipped step lands. Trust violation is itself a secondary acquisition signal: it forces evaluation at the trust boundary when the proposal overshoots. *Explicit* acquisition (NEB OIE) applies Eq. 4.3 after inner relaxation to select the single most informative image from the unevaluated set. This is closest to classical BO. The chemgp-core implementation also provides MaxVariance, EI, and Thompson sampling strategies as alternatives. *Exhaustive* acquisition (NEB AIE) evaluates all  $P$  images at each outer iteration, bypassing image selection entirely. Table 2 summarizes the acquisition strategies used in each method. All three share the same Bayesian surrogate loop structure (Algorithm 4), differing only in how the acquisition criterion selects the next oracle point.

**Table 2.** Acquisition criteria across GP methods. GP-minimization and GP-dimer use implicit acquisition (trust-clipped step from inner loop), GP-NEB OIE uses explicit UCB selection from unevaluated images, and GP-NEB AIE uses exhaustive evaluation of all images.

Method	Mode	Selection Criterion	Calls/iter
GP-minimization	Implicit	Trust-clipped step	1
GP-dimer	Implicit	Trust-clipped step	1
GP-NEB OIE	Explicit	UCB on unevaluated images	1
GP-NEB AIE	Exhaustive	All images	$P$

The three application sections that follow each instantiate Algorithm 4 for their specific inner optimization and acquisition criterion.

## 5 GPR-Accelerated Minimum Mode Following, the GP-dimer

### 5.1 Overview

The standard dimer method is expensive because it is *iterative at two levels*: every translation step requires multiple rotation steps, each requiring a fresh electronic structure evaluation. A GP surrogate trained on the accumulated data replaces these inner evaluations with cheap predictions, and only the outer loop returns to the true PES to validate and extend the training set. Whereas GP-NEB requires known initial and final states (Section 6), the GP-dimer requires only a starting configuration and an initial guess for the dimer orientation.

The idea of using a machine-learned surrogate to accelerate saddle point searches goes from neural networks [78] to direct applications of Gaussian Processes [39, 40, 60] to specialized inverse-distance kernels [39, 62], to improved runtime and reliability from optimal transport extensions [38].

The specific algorithmic choices presented here (per-pair-type length scales optimized by maximum likelihood, the SE kernel in inverse-distance space, L-BFGS for translation) represent one point in a large design space. In the Bayesian surrogate loop (Algorithm 4), the GP-dimer instantiates the inner optimization as CG rotation followed by L-BFGS translation on  $V_{\text{GP}}$ , and uses implicit acquisition (Section 4): the oracle evaluates at the trust-clipped midpoint. When  $\kappa > 0$ , the LCB convergence criterion (Eq. 4.2) prevents the inner loop from terminating in uncertain regions. The remaining loop steps (FPS subset, SCG training, RFF prediction, EMD trust) follow the generic framework and are developed in Section 8. The inner components (kernel form, hyperparameter strategy, optimizer, trust region) can be varied independently, and in Section 6, at least three independent implementations with different kernel, descriptor, and hyperparameter choices achieve comparable performance. The `chemgp-core` and `gpr_optim` codes share the same algorithmic choices, though both differ from the original publications in specific convergence criteria and inner-loop heuristics.

The algorithm requires an initial exploration phase before the surrogate can take over. Skipping it and fitting a GP to just one or two evaluations produces a surrogate that is effectively a constant surface with large uncertainty everywhere; the dimer has no meaningful curvature to follow and wanders randomly. The two phases are:

#### 5.1.1 Phase 1: Initial Rotations (Finding the Minimum Mode)

The first few electronic structure evaluations establish the minimum mode direction. The dimer midpoint  $\mathbf{R}_0$  and one endpoint  $\mathbf{R}_1$  are evaluated on the true PES. The dimer is then repeatedly rotated, evaluating the true PES at each new  $\mathbf{R}_1$  position, until the orientation converges. Typically,  $\sim 6$  evaluations suffice. The convergence criterion for this phase is either a small preliminary rotation angle ( $\omega^* < 5^\circ$ ) or a small angle between successive converged orientations. These initial evaluations constitute the training set for the first GP model.

#### 5.1.2 Phase 2: GPR Iterations (Rotation + Translation on the Surrogate)

Once the initial minimum mode is established, the GP takes over. Algorithm 5 and Figure S1 (right) summarize the Phase 2 iteration.

---

#### Algorithm 5: GP-dimer Phase 2 (surrogate iterations)

---

**Input:** Training set  $\mathcal{D}$  from Phase 1, force threshold  $\epsilon_{\text{force}}$

**Output:** saddle point at  $\mathbf{R}_0$

```

1 repeat
2   Fit GP hyperparameters by maximizing  $\mathcal{L}(\theta)$  (Eq. 3.14) on  $\mathcal{D}$ ;
3   Run full dimer (rotation via CG + translation via L-BFGS) on  $V_{\text{GP}}(\mathbf{x})$ ;
4   ; // until surrogate convergence or trust radius violated
5   Evaluate true PES at midpoint  $\mathbf{R}_0$ ;
6   if  $|\mathbf{F}(\mathbf{R}_0)| < \epsilon_{\text{force}}$  then
7     return saddle point at  $\mathbf{R}_0$ ;
8   end
9   Add  $(\mathbf{x}, V, \nabla V)$  to  $\mathcal{D}$ ;
10 until converged;
```

---

The surrogate prediction at a new point is:

$$V_{\text{GP}}(\mathbf{x}_{\text{new}} | \mathcal{D}, \boldsymbol{\theta}_{\text{opt}}) \approx V(\mathbf{x}_{\text{new}}) \quad (5.1)$$

where  $\mathcal{D} = \{(\mathbf{x}_i, V_i, \nabla V_i)\}_{i=1}^M$  is the training set of previously computed configurations. The GP predictions of the force at the dimer endpoint  $\mathbf{R}_1$  replace the finite-difference extrapolations normally used. The GP posterior mean for the gradient uses all accumulated force data rather than just the most recent pair, and therefore produces a more accurate estimate.

The source of the savings is easy to trace. In the ‘‘improved’’ dimer formulation in eOn [79]<sup>3</sup> [44, 45], each translation step requires 5 to 15 rotation evaluations (each a full electronic structure call) to converge the orientation. The GP replaces almost all of these inner rotations with surrogate queries that cost microseconds rather than minutes, though the first few initial rotations take true forces. The outer loop still needs one true evaluation per translation step to validate the surrogate and extend the training set, but the inner loop is essentially free. Benchmarks [25, 38] show the median evaluation count dropping by a factor of ten which is precisely the factor one expects from eliminating the inner rotation cost. Despite working in Cartesian coordinates, the GP-dimer achieves performance comparable to internal-coordinate methods (Sella [80]), because the inverse-distance kernel (Eq. 3.10) learns per-pair length scales that adapt to the stiffness landscape of each reaction.

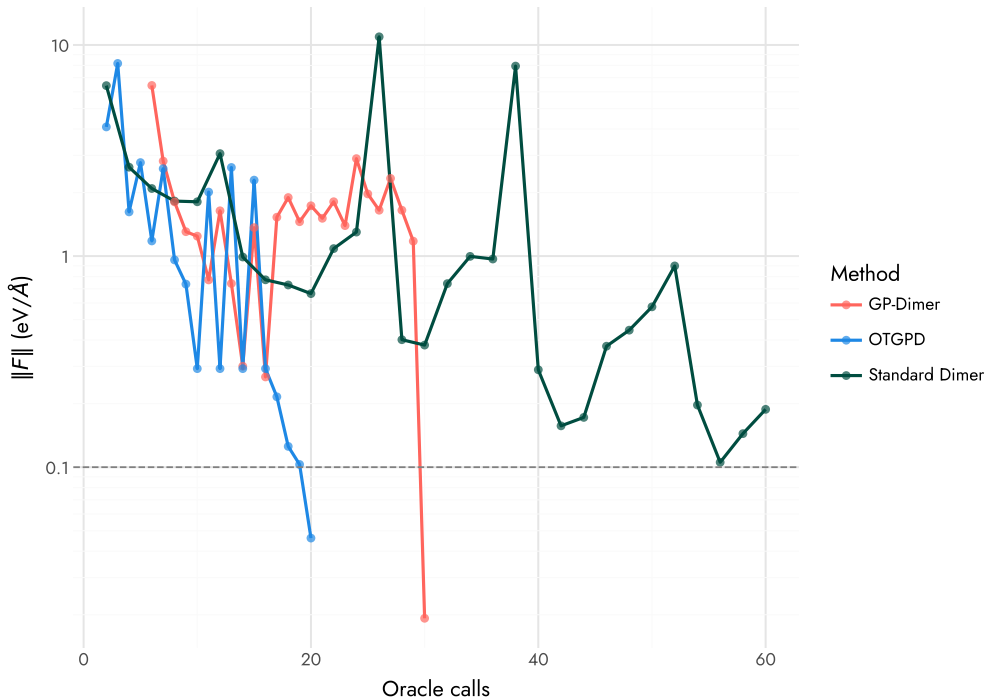


**Figure 9.** Convergence comparison of the standard dimer, GP-dimer, and OT-GP dimer (OTGPD) on a molecular system ( $\text{C}_3\text{H}_5$  allyl radical, 8 atoms, 24 DOF) via eOn server mode. The maximum per-atom force ( $\text{eV}/\text{\AA}$ ) is plotted against oracle evaluations on a logarithmic scale. The OTGPD variant reaches the convergence threshold (gray dashed,  $0.1 \text{ eV}/\text{\AA}$ ) with the fewest oracle calls; the GP-dimer shows oscillations from surrogate retraining instabilities that the OT-GP extensions suppress.

## 5.2 Trust Regions and Early Stopping

Left unconstrained, the GP-guided optimizer will eventually propose a geometry that lies outside the region where the surrogate is accurate [37]. Two distinct things can go wrong, and each requires its own safeguard.

<sup>3</sup><https://eondocs.org>

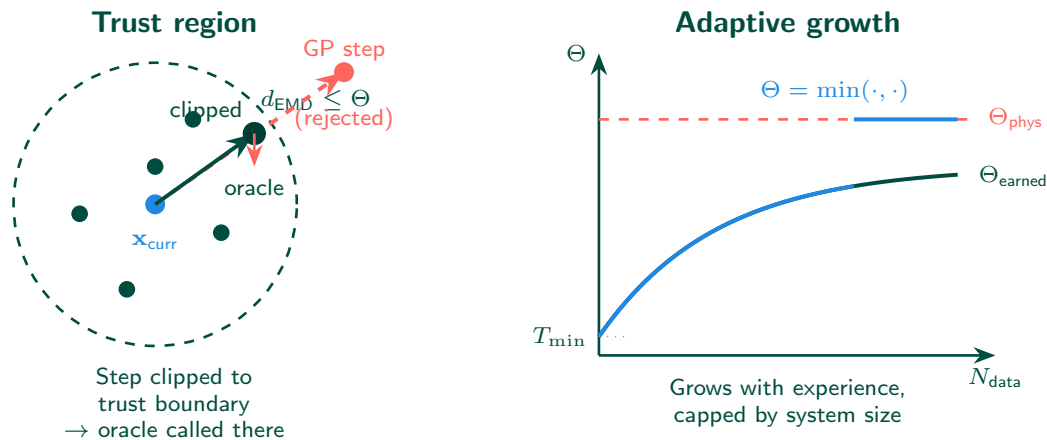


**Figure 10.** Trust region mechanism. (Left) A GP-proposed step (coral) that exceeds the trust boundary  $d_{\text{EMD}} \leq \Theta$  is clipped to the boundary; the oracle evaluates at the clipped location. (Right) The trust radius grows with accumulated data via an exponential saturation curve ( $\Theta_{\text{earned}}$ ), capped by a system-size-dependent physical ceiling ( $\Theta_{\text{phys}}$ ).

### 5.2.1 Extrapolation to Unseen Geometries

The first problem is that the optimizer proposes a configuration that is structurally unlike anything in the training set [72], and the models are best as interpolators, not extrapolators. The GP posterior mean in such a region is pulled toward the prior mean (near zero after subtracting the constant offset), which typically produces a spurious minimum that traps the dimer. The posterior variance is large, but the optimizer ignores variance and follows the mean. To detect when a proposed geometry has left the neighborhood of the training data, we measure its dissimilarity to the nearest training point using the 1D-max-log distance [38]:

$$D_{1\text{Dmaxlog}}(\mathbf{x}_1, \mathbf{x}_2) = \max_{i,j} \left| \log \frac{r_{ij}(\mathbf{x}_2)}{r_{ij}(\mathbf{x}_1)} \right| \quad (5.2)$$

This metric operates on interatomic distance *ratios* rather than absolute distances, so it is scale-invariant: a 10% change in the closest atom pair registers the same whether the pair is 1 Angstrom or 3 Angstrom apart. A proposed configuration is accepted only if its 1D-max-log distance to the nearest training point is below a threshold; otherwise, the algorithm falls back to evaluating the true PES at the trust boundary.

### 5.2.2 Atoms Approaching Too Closely

The second problem is specific to molecular systems: the optimizer can push two atoms into near-overlap. Even if the geometry is technically within the trust region (because the *log-ratio* distance to a training point is small), the electronic structure code may fail on a geometry with sub-Angstrom contacts. A step-size limit prevents this:

$$L_{\text{max}} = \frac{1}{2}(1 - r_{\text{limit}}) \cdot d_{\text{min}} \quad (5.3)$$

where  $d_{\text{min}}$  is the minimum interatomic distance in the current configuration and  $r_{\text{limit}} \in [0, 1]$  controls the conservativeness of the constraint. Values near 1 enforce small, cautious steps; values near 0 allow larger steps. This constraint is separate from the trust radius because the failure mode is different: the trust radius catches extrapolation in feature space, while the minimum-distance constraint catches a physically unacceptable geometry that the feature-space metric might miss.

The optimal transport extensions [38] cover walltime considerations due to the cubic scaling of the Cholesky factorization, the oscillation of surrogate surfaces on retraining, and add a trust region based on molecular similarity considerations, with bounds on hyperparameters. Here we will demonstrate how trivially extensible

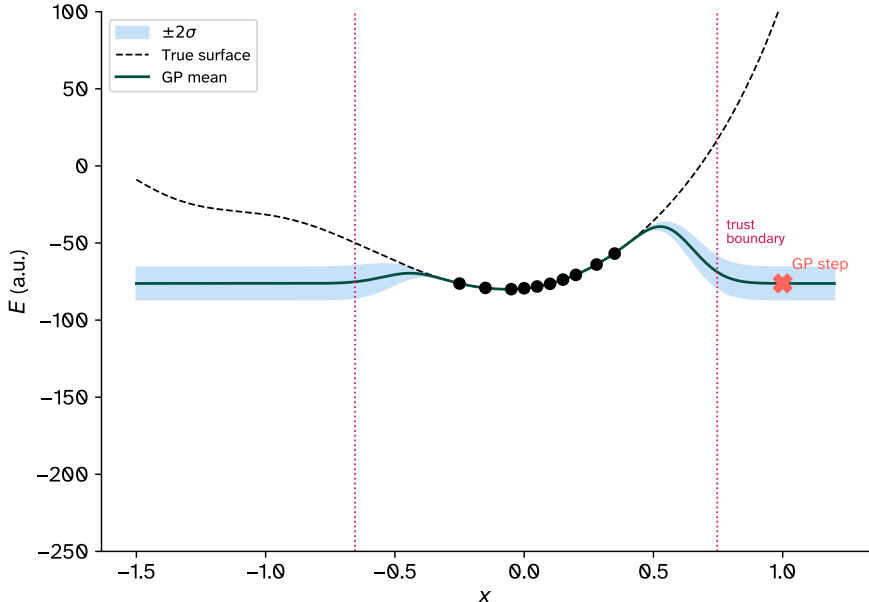


**Figure 11.** Trust region mechanism on a 1D slice ( $y = 0.5$ ) of the Muller-Brown surface. The GP posterior mean (teal) and  $\pm 2\sigma$  confidence band (light blue) are accurate near the training data (black dots) but diverge from the true surface (black dashed) outside the trust boundaries (magenta dotted verticals). A hypothetical GP-proposed step at  $x = 1.0$  (coral cross, labeled “GP step”) falls outside the trust region, where the surrogate is unreliable; the algorithm instead evaluates the true PES at the trust boundary (teal star, “Oracle fallback”).

these concepts are to the NEB within our framework. This forms section 6 where the surrogate accelerates the relaxation of multiple images along the minimum energy path.

## 6 GPR-Accelerated Nudged Elastic Band

GP-NEB instantiates Algorithm 4 with NEB force relaxation as the inner optimization and explicit UCB acquisition from unevaluated images as the selection criterion. The AIE variant uses exhaustive acquisition (all  $P$  images per iteration); the OIE variant selects a single image via the variance criterion (Eq. 6.1). Per-bead FPS and EMD trust adapt the shared components to the string discretization. The additional design choice specific to NEB is *how many* images to evaluate at each outer iteration, which determines the trade-off between surrogate accuracy and the cost per cycle [29, 62, 76, 81, 82].

Two variants bracket the design space. In the *all-images-evaluated* (AIE) variant, all  $P$  images are evaluated on the true PES at each outer iteration. This provides a dense training set before each surrogate relaxation and achieves a  $\sim 5\times$  reduction in total evaluations. In the more aggressive *one-image-evaluated* (OIE) variant, only the image with the largest GP posterior variance is evaluated.

$$i^* = \arg \max_{i \in \{1, \dots, P\}} \text{var}[V_{\text{GP}}(\mathbf{R}_i)] \quad (6.1)$$

This active learning criterion selects the image where the surrogate is least certain, roughly halving the evaluations compared to AIE. Equation 6.1 is the pure-variance criterion ( $\kappa = 0$  in Eq. 4.3); the LCB-augmented form balances force magnitude against uncertainty and is the default in chemgp-core. The trust region safeguards from Section 5.2 apply to both variants. When an image drifts beyond the reliable region of the surrogate, the constraint violation triggers an evaluation at that image, which is an implicit acquisition strategy. Figure S2 (right) illustrates both variants.

Three independent implementations of surrogate-accelerated NEB now exist. The CatLearn MLNEB [62], built on ASE [83], uses a Student’s t-process (Section 3.4) with a single isotropic length scale for surface catalysis; though the inverse-distance SE kernel with per-pair-type length scales is the current state of the art

implementation<sup>4</sup>. All reported calculations achieve 5–10 $\times$  reductions in electronic structure evaluations on their respective benchmarks, despite differing kernel, descriptor, and hyperparameter choices. The fact that these different combinations converge on comparable performance suggests that the active learning loop, not the specific surrogate model, is the primary source of the savings.

Figures 12–14 illustrate the GP-NEB on two test surfaces. On the Muller-Brown surface (Figure 12), an 11-image climbing-image NEB resolves the path from minimum A through saddle S2 to minimum B. The LEPS surface (Figure 13) provides a higher-dimensional test case modeling a collinear atom transfer  $A + BC \rightarrow AB + C$ , where the 9-dimensional NEB path projects onto the  $(r_{AB}, r_{BC})$  plane. The convergence comparison in Figure 14 quantifies the oracle savings of the AIE and OIE acquisition strategies on this surface.

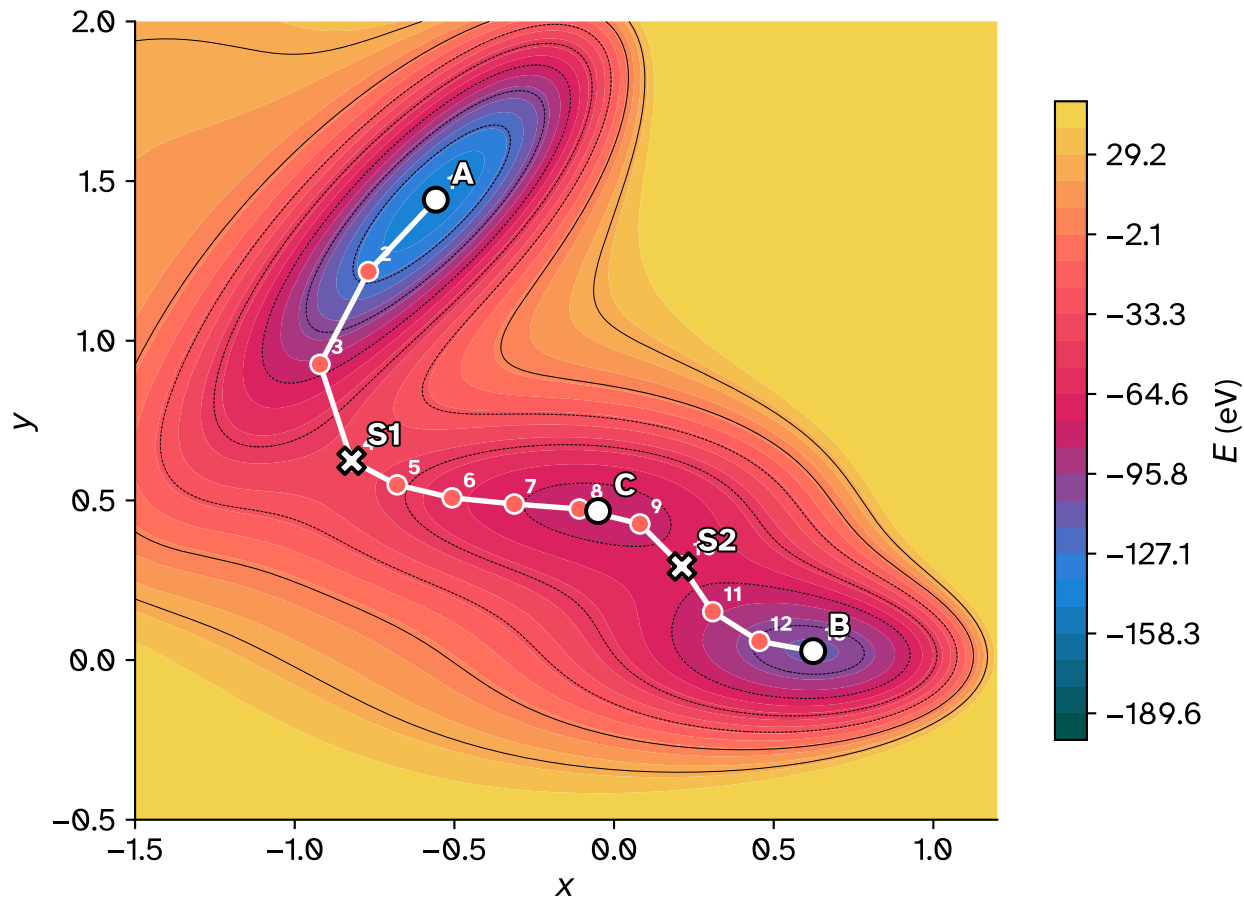


**Figure 12.** Muller-Brown potential energy surface with NEB path overlay. Filled contours show the energy landscape with three local minima (A, B, C) and two saddle points (S1, S2). Eleven NEB images (coral circles, numbered) trace the minimum energy path from A to B through S2. The climbing image (highest-energy interior image) approximates the saddle point. Energy values clipped to  $[-200, 50]$  a.u.

In the chain-of-states picture (Section 2.4), the inner loop evolves the discretized path under the force field of  $V_{GP}$  rather than  $V$ . The surrogate surface is a flexible interpolator trained on finitely many data points, and it generically has *more* stationary points than the true PES. Spurious minima and saddle points arise in the regions between training configurations where the GP reverts toward its prior. These additional critical points are an unavoidable consequence of building a smooth model from sparse data, and the outer loop exists precisely to filter them. At each outer iteration, the true PES is evaluated at the configuration proposed by the surrogate optimization, and if the true forces are not small, the new data point eliminates the spurious feature that trapped the optimizer. The trust region (Section 5.2) provides a second filter, preventing the

<sup>4</sup>and is adopted in the upstream codebase

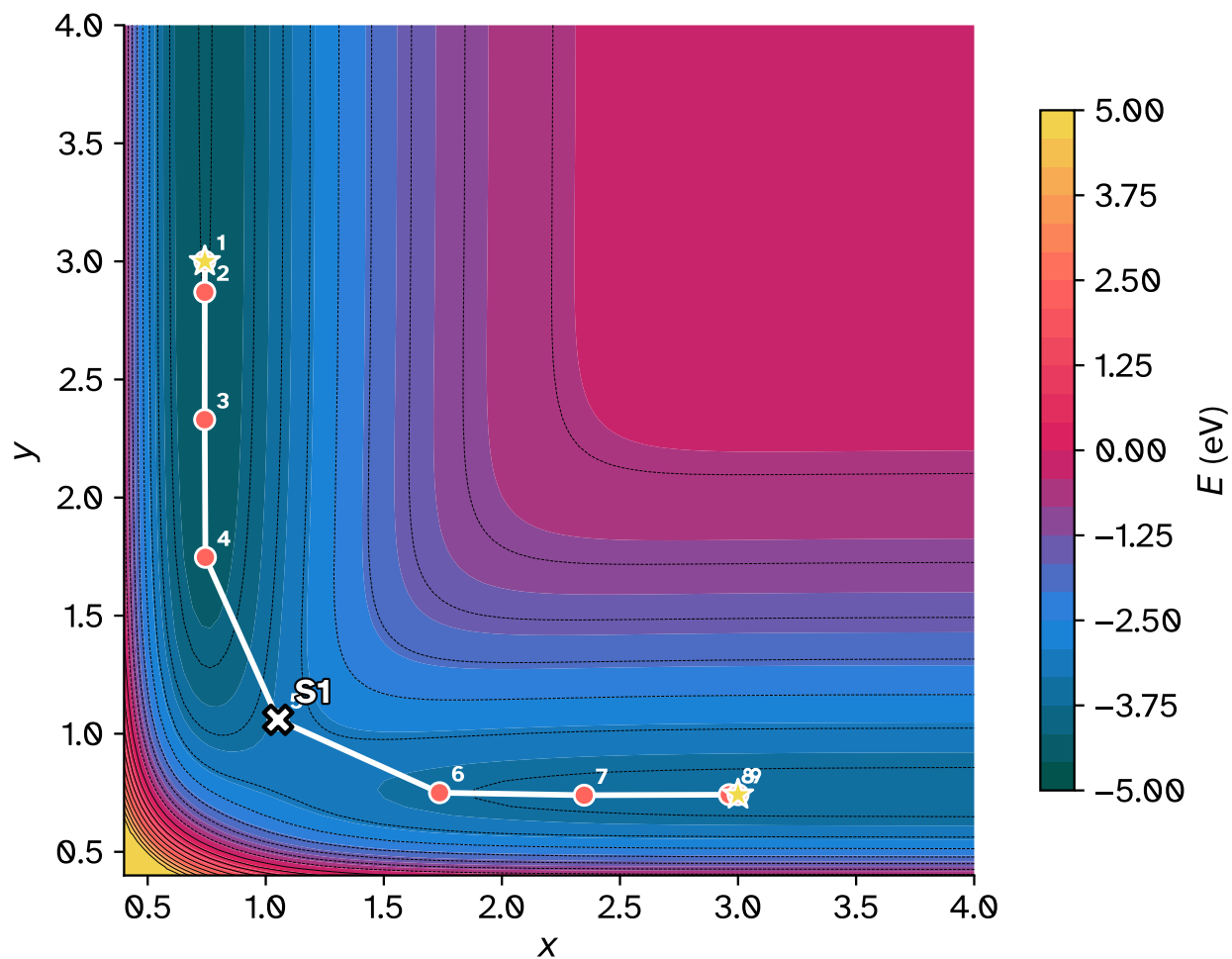


**Figure 13.** LEPS potential energy surface with NEB path overlay. The collinear atom transfer reaction  $A + BC \rightarrow AB + C$  is plotted as a function of bond distances  $r_{AB}$  and  $r_{BC}$ . Seven interior NEB images and two fixed endpoints (nine path points, coral circles numbered; endpoints also marked by yellow stars) are optimized in the full 9-dimensional coordinate space and projected onto the  $(r_{AB}, r_{BC})$  plane. The climbing image converges to the saddle region near  $r_{AB} \approx r_{BC} \approx 1.0$  Å. Contour spacing is 0.5 eV; energies clipped to  $[-5, 5]$  eV.

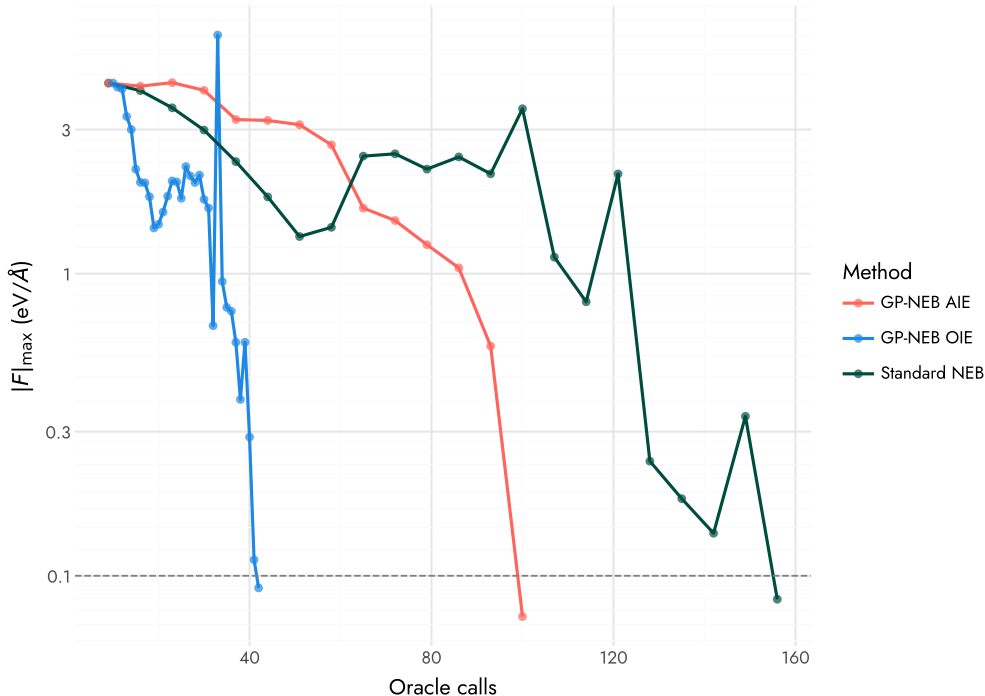


**Figure 14.** Convergence of NEB variants on the LEPS surface. Maximum per-atom force versus oracle evaluations on a logarithmic scale. Standard NEB (156 calls), AIE (100 calls), and OIE (42 calls) all reach the convergence threshold (dashed, 0.1 eV/Å). The OIE variant evaluates only the highest-variance image per cycle (Eq. 6.1) and converges fastest.

optimizer from reaching distant spurious features by confining each inner-loop step to the neighborhood where the GP has earned credibility from training data.

A property that makes this scheme well-posed is that the GP operates on Cartesian coordinates. Every configuration visited during the inner-loop optimization, including configurations at spurious stationary points of  $V_{\text{GP}}$ , is a valid atomic geometry in  $\mathbb{R}^{3N}$  that can be handed directly to the electronic structure code for evaluation. The inverse-distance kernel uses a feature map  $\phi(\mathbf{x}) = \{1/r_{ij}(\mathbf{x})\}$  internally, but the optimization variable remains  $\mathbf{x}$ , so there is no inverse problem. This would not hold for a method that optimized the path in descriptor space (e.g., SOAP), where the optimized images would be points in  $\mathbb{R}^{d_{\text{SOAP}}}$ , and recovering Cartesian pre-images would require solving a separate inverse problem that may have no solution (not every point in descriptor space corresponds to a valid geometry) or multiple solutions (the descriptor map is not injective). By keeping the optimization in Cartesian space and confining the descriptor to the kernel interior, the GP-NEB avoids this entirely. Every proposed path is physically realizable, and the only question is whether it lies on the true MEP.

Path initialization matters for the GP-NEB. The sequential image-dependent pair potential (S-IDPP) method [84], which builds on the IDPP [85] which interpolates interatomic distances rather than Cartesian coordinates, produces chemically reasonable initial configurations whose training data samples a more physical region of configuration space than linear interpolation would provide. This method may be augmented by the iterative rotations and assignments algorithm [54, 86]. Linear interpolation in Cartesian coordinates often creates initial paths where atoms pass through each other or where interatomic distances become unphysically short, producing training data from a region of the PES that is irrelevant to the reaction pathway and poorly conditioned for GP learning. These calculations may be visualized together on 2D plots [87].

## 7 GPR-Accelerated Minimization

Minimization is the simplest instantiation of Algorithm 4: the inner optimization is L-BFGS on  $V_{\text{GP}}$ , trust clipping is Euclidean or EMD, and acquisition is implicit (the oracle evaluates at the trust-clipped L-BFGS result). The LCB convergence criterion (Eq. 4.2, with total gradient  $\sigma_g$  instead of  $\sigma_{\perp}$ ) optionally augments the inner stopping rule. Denzel and Kastner [72] developed GP-accelerated minimization systematically, benchmarking a GP-based geometry optimizer against L-BFGS on 26 molecular systems and finding that the Matern kernel in Cartesian coordinates outperforms the squared exponential. They subsequently extended the approach to internal coordinates [88] and to MEP optimization [82]. An important distinction is that these earlier GP optimizers operate with kernels defined directly on Cartesian or internal coordinates, without the inverse-distance feature map (Section 3.3.1) that provides rotational and translational invariance. The inverse-distance kernel, introduced for NEB by Koistinen, Asgeirsson, and Jonsson [29] and adopted throughout the present framework, avoids the need for explicit coordinate alignment between training configurations and enables the GP to generalize across rigid-body motions of the molecule. Algorithm 6 summarizes the iteration.

---

### Algorithm 6: GP-accelerated local minimization

---

**Input:** Initial configuration  $\mathbf{x}$ , force threshold  $\epsilon_{\text{force}}$

**Output:** minimum at  $\mathbf{x}$

```

1 Evaluate  $V(\mathbf{x}), \mathbf{F}(\mathbf{x})$  on true PES;
2 repeat
3   Add  $(\mathbf{x}, V, \nabla V)$  to training set  $\mathcal{D}$ ;
4   Re-optimize GP hyperparameters (Eq. 3.14);
5   Run L-BFGS on  $V_{\text{GP}}(\mathbf{x})$  until GP forces vanish or trust radius violated;
6   Evaluate true PES at new  $\mathbf{x}$ ;
7   if  $|\mathbf{F}(\mathbf{x})| < \epsilon_{\text{force}}$  then
8     return minimum at  $\mathbf{x}$ ;
9   end
10 until converged;
```

---

The trust region plays the same role as in the GP-dimer, preventing the optimizer from venturing too far from the reliable region of the surrogate. The distance-based and interatomic-distance constraints from Section 5.2 apply directly. Figure 15 compares the GP-minimizer against classical L-BFGS on the LEPS surface.

The gains from GP acceleration are smaller for minimization than for saddle point searches, because the PES near minima is smooth and well-approximated by a quadratic, so standard L-BFGS already converges in few steps. The GP surrogate provides the largest benefit when the starting configuration is far from the minimum or when the electronic structure cost per evaluation is high (large systems, high-level methods). For a real molecular system, Figure 20 shows convergence of the GP-minimizer on the PET-MAD potential. GPR-accelerated minimization is particularly useful as a subroutine in adaptive kinetic Monte Carlo (AKMC), where many local minimizations are needed to characterize the final states of transitions discovered by saddle point searches. In AKMC, each saddle point found by the GP-dimer implies a transition to a new minimum, which must be located to continue the simulation. Reusing the GP training data from the saddle point search, which already samples the PES near the transition path, can warm-start the minimization and reduce the number of additional evaluations needed.

Section 8 develops the Optimal Transport GP (OT-GP) extensions that address the failure modes of the basic framework and make the Bayesian surrogate loop reliable for production use.

## 8 The Optimal Transport Gaussian Process Framework

1. *How do we keep the surrogate honest?* The signal variance can run away and the hyperparameters can oscillate, both of which produce surrogates that are unrelated to the true PES (Section 8.2).
2. *How far should we trust the surrogate?* A fixed trust radius is either too conservative (wasting oracle calls) or too aggressive (producing unphysical steps). The threshold should reflect how much the GP has actually learned (Section 8.3).

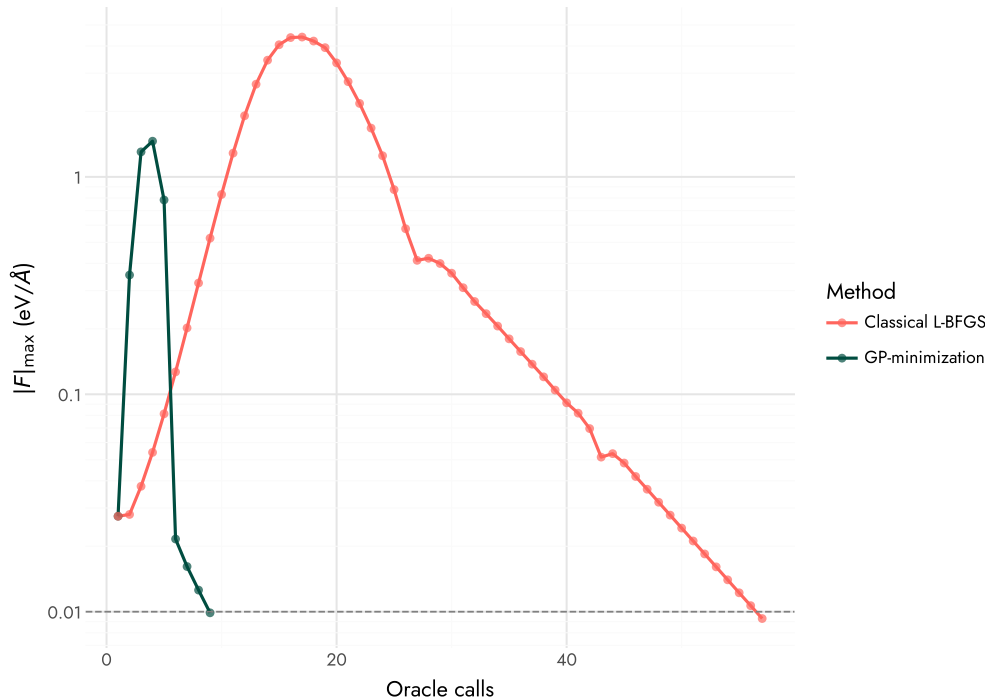


**Figure 15.** Convergence comparison of the GP-minimizer and classical L-BFGS on the LEPS surface. The GP surrogate reaches the convergence threshold in 10 oracle calls, compared to roughly 200 for direct gradient descent.

3. *Which training points matter?* As the dataset grows, the cubic cost of hyperparameter optimization becomes the bottleneck. Selecting a geometrically diverse subset keeps the cost bounded without sacrificing surrogate quality (Section 8.1).

The generic Bayesian surrogate loop (Algorithm 4) was introduced in Section 4. The present section develops the four shared components that make that loop reliable for production use: FPS with EMD (Section 8.1), MAP regularization (Section 8.2), the adaptive trust radius (Section 8.3), and RFF scaling (Section 8.4). Table 3 summarizes how these components specialize for each method.

**Table 3.** Shared Bayesian optimization components across GP methods. Each column shows how the six components specialize for a given method. Acquisition modes and the oracle gate are formalized in Section 4.

Component	Minimize	GP-dimer	OTGPD	NEB AIE	NEB OIE
FPS subset	global	global	HOD	per-bead	per-bead
Trust metric	Euclid./EMD	EMD	EMD	EMD	EMD
RFF predict	optional	optional	optional	optional	optional
Acquisition	implicit (Eq. 4.2)	LCB + trust	LCB + adaptive $T_{GP}$	exhaustive	UCB (Eq. 4.3)
Oracle gate	—	$\sigma_{\perp} < \sigma_{gate}$	$\sigma_{\perp} < \sigma_{gate}$	—	$\sigma_{\perp}$ phase
Inner optim	L-BFGS	rot.+trans.	rot.+trans.	L-BFGS	L-BFGS

Each of these components operates at the level of GP construction and hyperparameter management, not at the level of the optimizer itself. A dimer, a NEB, and a local minimizer all build a GP from accumulated data, re-optimize hyperparameters at each step, and propose new configurations on the surrogate. They all inherit the same failure modes, and they all benefit from the same stabilization mechanisms. We develop the per-bead FPS extension to NEB explicitly in Section 8.1; MAP regularization and the adaptive trust radius apply to any method without modification. Together, these changes reduce the failure rate from approximately 12% to approximately 2% across 500+ benchmark reactions [38]. Figure 16 shows the decision flow of the full pipeline.

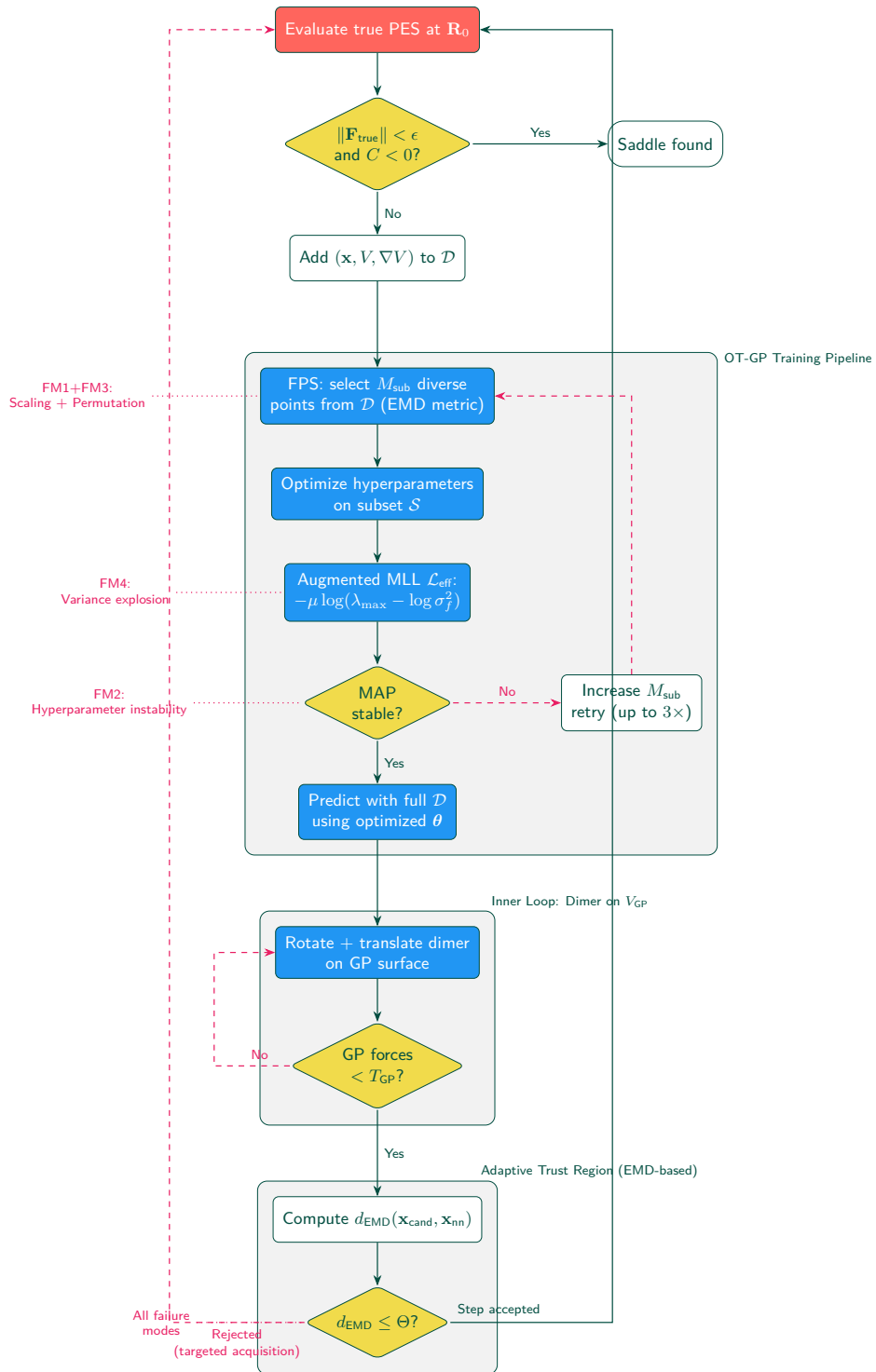


**Figure 16.** Decision flow of the OT-GP framework. The training pipeline (FPS, MAP regularization) and adaptive trust region (EMD-based) address the failure modes of the basic GP-dimer.

### 8.1 Farthest Point Sampling with Earth Mover’s Distance

As the search progresses and more electronic structure calculations are performed, the training set grows and the covariance matrix inversion becomes the dominant cost. For a system with  $N_{\text{atoms}}$  atoms and  $M_{\text{data}}$  collected configurations, the hyperparameter optimization involves repeated inversions at cost  $\mathcal{O}((M_{\text{data}} \cdot N_{\text{atoms}})^3)$ . The fix is to decouple hyperparameter optimization from prediction. We optimize hyperparameters on a small, geometrically spread-out subset  $\mathcal{S} \subset \mathcal{X}$ , chosen by farthest point sampling (FPS), while still using all collected data  $\mathcal{X}$  for prediction [89, 90]:

$$\mathbf{x}_{\text{next}} = \arg \max_{\mathbf{x}_i \in \mathcal{X} \setminus \mathcal{S}} \left[ \min_{\mathbf{x}_j \in \mathcal{S}} D(\mathbf{x}_i, \mathbf{x}_j) \right] \quad (8.1)$$

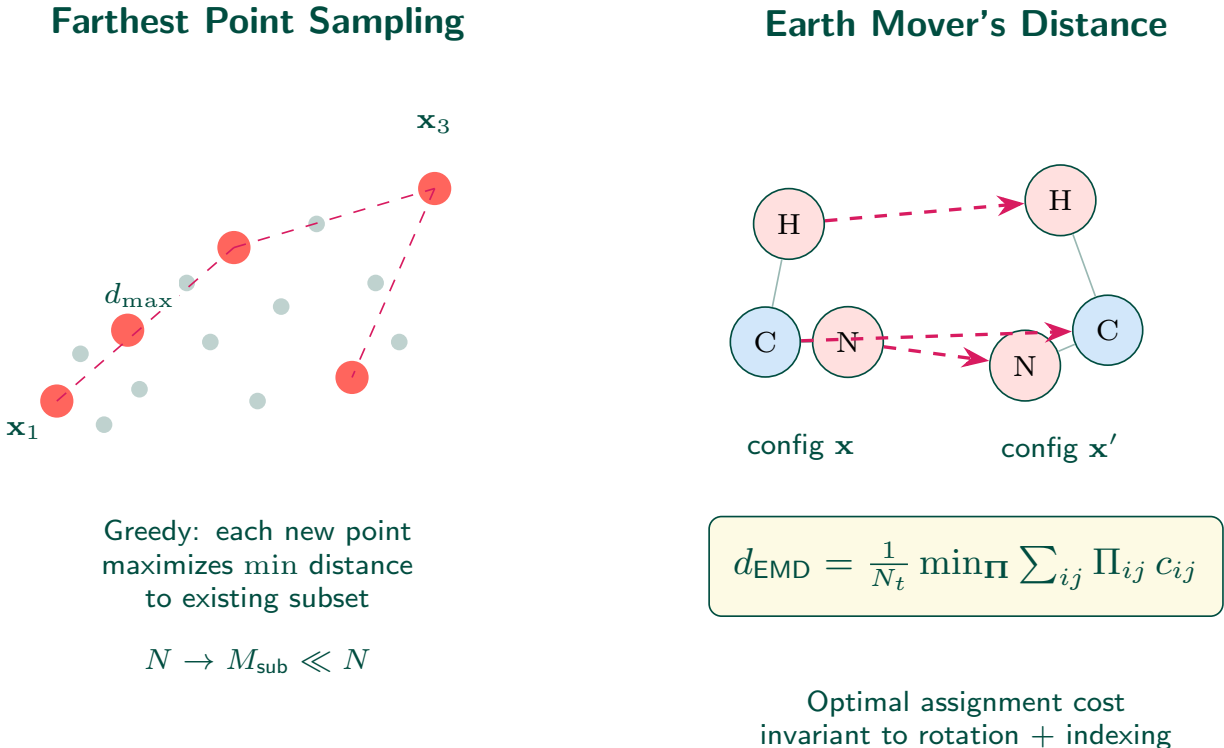


**Figure 17.** (Left) Farthest point sampling selects a geometrically spread-out subset (coral) from the full training set (gray) by greedily maximizing the minimum distance to the existing selection. (Right) The Earth mover’s distance measures structural dissimilarity between two molecular configurations as the optimal transport cost of matching their atom-pair distance distributions; it is invariant to rotation and atom indexing.

At each step, FPS picks the training point that is farthest from everything already selected, and repeats until  $M_{\text{sub}}$  points are chosen. Hyperparameters are optimized on this subset  $\mathcal{S}$ , but the full dataset  $\mathcal{X}$  is used for GP prediction. This bounds the optimization cost at  $\mathcal{O}((M_{\text{sub}} \cdot N_{\text{atoms}})^3)$  with  $M_{\text{sub}} \ll M_{\text{data}}$ . Two details matter in practice. First, the two most recent configurations are always forced into  $\mathcal{S}$ , regardless of their FPS rank, so that the hyperparameter estimates remain relevant to the current surrogate neighborhood. Second, 10 points is a good starting size for  $M_{\text{sub}}$ , but if the MAP estimate is unstable (detected by the oscillation monitor in Section 8.2), the subset grows adaptively up to  $M_{\text{sub}} = 30$ . The growth is triggered by a global signal (hyperparameter oscillation) rather than by local predictive variance, because kernel hyperparameters are global PES properties that require geometrically diverse data, whereas high local variance is better resolved by evaluating the true PES at that point (Section 8.3).

Extending FPS from the dimer to the NEB requires accounting for the string discretization. The NEB approximates the continuous MEP (Eq. 2.2) as a chain of  $P + 1$  images, each of which samples a different

local region of the PES. Configurations near the reactant minimum occupy a different part of configuration space than those near the saddle point, and the kernel length scales appropriate for one region need not suit the other. A single global FPS subset across all images mixes configurations from these different PES regions, producing hyperparameter estimates that compromise between them. The natural solution is to maintain one FPS subset  $\mathcal{S}_i$  per image  $i$ , so that each local surrogate draws its hyperparameters from configurations in the relevant neighborhood. This per-bead structure mirrors the NEB force decomposition itself, and just as the NEB force (Eq. 2.10) acts independently on each image’s perpendicular subspace, the FPS selects data independently for each image’s local GP. In practice, each image maintains its own  $\mathcal{S}_i$  with the same greedy selection rule (Eq. 8.1) applied to the subset of training data within a cutoff distance of that image in the EMD metric.

This technique differs from sparse GPs [55, 91] which introduce  $M \ll N$  pseudo-inputs optimized jointly with hyperparameters, approximating the full posterior at  $\mathcal{O}(M^2N)$  cost. That machinery suits the regime of large, static training sets. In the on-the-fly setting here, the training set starts nearly empty, grows by a few points per iteration, and rarely exceeds a few dozen configurations; re-optimizing inducing point locations at every step would add cost without benefit. FPS selects only *actually observed* configurations for hyperparameter optimization and retains the full dataset for prediction; no information is discarded. For problems that grow beyond roughly 100 evaluations, the RFF approach in Section 8.4 addresses the crossover to the large-data regime.

Beyond the computational savings, FPS improves the conditioning of the kernel matrix. Well-separated configurations produce small off-diagonal kernel entries (the SE kernel decays exponentially with distance), which by the Gershgorin circle theorem keeps the eigenvalues of  $\mathbf{K}$  away from zero. This numerical stability benefit is independent of the cost savings and would justify FPS even if the hyperparameter optimization were cheap.

Figure 18 illustrates the FPS selection on the LEPS surface. After a GP-NEB run collects approximately 50 candidate configurations, FPS selects 20 maximally diverse points in inverse-distance feature space, as visualized through PCA projection. The selected points (teal diamonds) span the feature space uniformly, while the pruned points (gray circles) cluster in already-represented regions.

The distance metric  $D$  in Eq. 8.1 determines which configurations the algorithm considers “similar” and which it considers “different.” A bad choice here can sabotage the entire FPS selection. The 1D-max-log distance (Eq. 5.2) compares atoms by fixed index, and this breaks down whenever chemically equivalent atoms swap positions. The classic example is a methyl group rotation: three hydrogens rotate by 120 degrees, but because each hydrogen keeps its original index, the fixed-index metric registers a large geometric displacement even though the molecule has barely changed. The trust region then rejects the configuration as “too far” from the training data, or FPS treats two nearly identical structures as maximally different, wasting a slot in the subset. What we need is a distance that matches atoms of the same element before measuring displacement. The Earth Mover’s Distance (EMD) [92] does exactly this. For each atom type  $t$ , we solve a linear assignment problem that optimally pairs atoms between two configurations to obtain the per-type average displacement:

$$\bar{d}_t = \frac{1}{N_t} \min_{\pi \in \Pi_{N_t}} \sum_{k=1}^{N_t} \|\mathbf{r}_{k,t}^{(1)} - \mathbf{r}_{\pi(k),t}^{(2)}\| \quad (8.2)$$

where  $N_t$  is the number of atoms of type  $t$  and  $\Pi_{N_t}$  is the set of all permutations. The overall distance is the maximum per-type displacement:

$$D(\mathbf{x}_i, \mathbf{x}_j) = \max_t \bar{d}_t(\mathbf{x}_i, \mathbf{x}_j) \quad (8.3)$$

Two design choices in this definition deserve explanation. First, the per-element averaging by  $1/N_t$  makes the metric scale-independent: a 5-atom molecule and a 50-atom molecule with the same reactive core produce comparable distance values. Without this normalization, adding inert atoms to the system (a larger solvent shell, a surface slab with more layers) would shrink the per-atom contribution and make the metric blind to the actual chemical change. This property is what lets us define a single trust radius threshold that works across systems of different sizes (Section 8.3). Second, the max over atom types ensures that a large displacement of *any* chemical species is detected, even if most other atoms are stationary. Together with the permutation optimization in Eq. 8.2, which resolves failure mode (3) described earlier, these choices produce a distance that tracks genuine structural change rather than labeling artifacts.

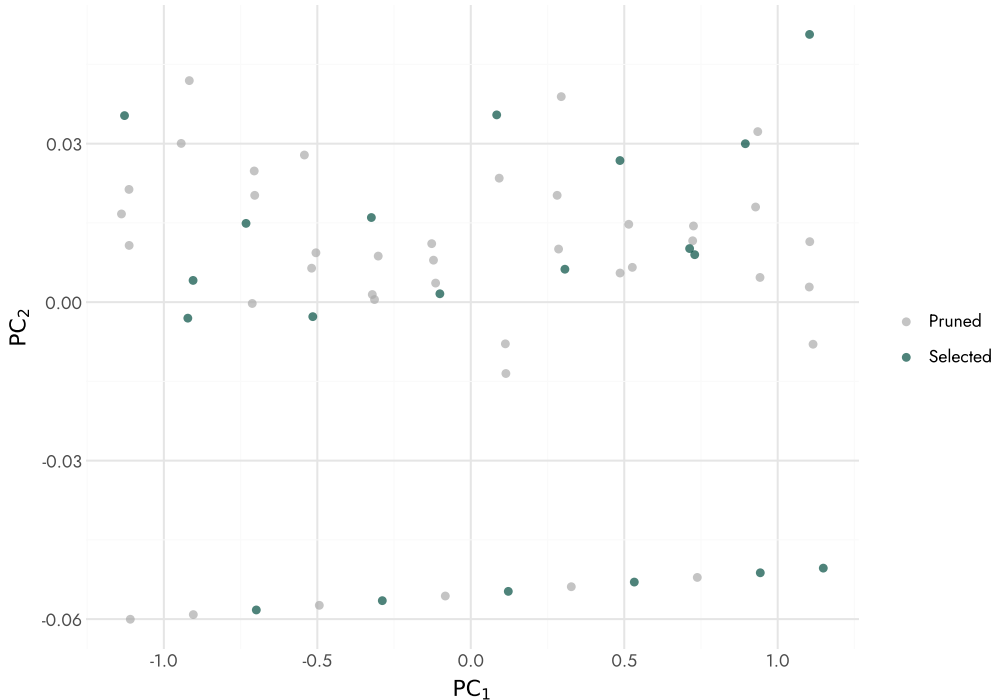


**Figure 18.** Farthest point sampling (FPS) on the LEPS surface. Approximately 50 candidate configurations from a GP-NEB run are projected onto their first two principal components in inverse-distance feature space. FPS selects 20 points (teal diamonds) that maximally cover the feature space; pruned points (gray circles) lie near already-selected configurations and would add redundancy to the training set without improving kernel matrix conditioning.

To see the permutation invariance in action, consider a proton (indexed  $k$ ) transferring between two chemically equivalent sites (atoms  $m$  and  $n$ ). The initial and final states are energetically degenerate, and the true structural difference is small. But a fixed-index metric like the 1D-max-log distance (Eq. 5.2) sees atom  $k$  far from its original position and reports a large displacement, because it cannot recognize that relabeling  $m$  and  $n$  would reconcile the structures. The EMD solves the assignment problem and correctly identifies the proton transfer as a small rearrangement. In chemgp-core (`src/emd.rs`), the optimal assignment is computed by the Hungarian algorithm [93] at  $\mathcal{O}(N_t^3)$  cost, matching the C++ `gpr\optim` implementation. For the small atom groups typical of saddle point searches ( $N_t \leq 20$ ), this cost is negligible.

The per-type linear assignment problem (Eq. 8.2) is a discrete optimal transport problem, which gives the framework its name. The “earth” being moved is a unit point mass at each atomic position, and the “work” is the total displacement needed to transform one configuration into the other [38].

## 8.2 Regularizing the MAP Estimate

With few data points the MLL landscape is poorly determined, and the MAP estimate of the hyperparameters exhibits two pathologies. First, the signal variance  $\sigma_f^2$  grows without bound because the data-fit term in Eq. 3.14 dominates the complexity penalty. The resulting surrogate interpolates the training data exactly and produces steep, unphysical gradients between data points. Soft penalties (L1 or L2 on  $\sigma_f^2$ ) are easily overwhelmed by the MLL gradient, so a hard ceiling is needed. Second, the full hyperparameter vector oscillates between competing MLL modes at successive iterations: the marginal likelihood landscape shifts every time a new data point arrives or the FPS subset changes, and with a small training set the optimizer has no strong reason to prefer one local minimum over another. The surrogate surface changes shape erratically, and the search makes no net progress.

We address the first pathology with a logarithmic barrier drawn from interior point methods [94, 95], augmenting the MLL:

$$\mathcal{L}_{\text{eff}}(\boldsymbol{\theta}) = \log p(\mathbf{y} \mid \mathcal{S}, \boldsymbol{\theta}) - \mu \log(\lambda_{\text{max}} - \log \sigma_f^2) \quad (8.4)$$

where  $\lambda_{\text{max}}$  is an absolute upper bound for  $\log \sigma_f^2$  and  $\mu \geq 0$  is the barrier strength, which grows with the training set size so that the GP has room to adapt when data is scarce and progressively less room to inflate its variance as evidence accumulates. For the second pathology, a sign-reversal diagnostic over a sliding window detects oscillation: when a large fraction of the hyperparameters reverse direction at every step, the algorithm grows the FPS subset size  $M_{\text{sub}}$  (Section 8.1) and re-runs the optimization, up to three retries. Adding more geometrically diverse data sharpens the MLL landscape and constrains the optimizer. Both fixes are standard regularization of the MAP estimate: the barrier imposes a hard constraint on one parameter, and the subset growth sharpens the MLL landscape for all parameters.

### 8.3 Adaptive Trust Radius

A fixed trust radius is either too conservative (wasting oracle calls) or too aggressive (producing unphysical geometries). The natural solution is to let the radius grow with the GP’s experience, measured via the intensive EMD (Eq. 8.3) for size-independent thresholds. A candidate configuration  $\mathbf{x}_{\text{cand}}$  is accepted only if:

$$d_{\text{EMD}}(\mathbf{x}_{\text{cand}}, \mathbf{x}_{\text{nn}}) \leq \Theta(N_{\text{data}}, N_{\text{atoms}}) \quad (8.5)$$

where  $\mathbf{x}_{\text{nn}}$  is the nearest neighbor in the training set and  $\Theta$  follows an exponential saturation curve:

$$\Theta_{\text{earned}}(N_{\text{data}}) = T_{\text{min}} + \Delta T_{\text{explore}} \cdot (1 - e^{-kN_{\text{data}}}), \quad k = \frac{\ln 2}{N_{\text{half}}} \quad (8.6)$$

with a physical ceiling:

$$\Theta_{\text{phys}}(N_{\text{atoms}}) = \max \left( a_{\text{floor}}, \frac{a_A}{\sqrt{N_{\text{atoms}}}} \right) \quad (8.7)$$

The final threshold is  $\Theta = \min(\Theta_{\text{earned}}, \Theta_{\text{phys}})$ . The earned component (Eq. 8.6) grows rapidly with the first few data points and saturates, so that late-stage evaluations do not keep inflating the step size. The physical ceiling (Eq. 8.7) scales as  $1/\sqrt{N_{\text{atoms}}}$  because per-atom displacements are smaller in larger systems. Here  $a_A$  is a characteristic atomic length scale (approximately 1.0 Å, the typical bond length), and  $a_{\text{floor}}$  is a minimum threshold to prevent the trust radius from becoming too small for small systems. When a proposed step violates the trust radius, the algorithm evaluates the true PES at the rejected configuration and adds the result to the training set, turning the violation into targeted acquisition that concentrates the electronic structure budget near the transition path.

### 8.4 Scaling via Random Fourier Features

The FPS strategy (Section 8.1) bounds the hyperparameter optimization cost, but prediction still requires the full  $M(1 + 3N) \times M(1 + 3N)$  covariance matrix. For long NEB paths or large systems where the training set grows beyond  $\sim 50$  configurations, even the prediction step becomes a bottleneck. Random Fourier features (RFF) [96, 97] provide a way to decouple hyperparameter training from prediction, using the per-bead FPS subset for the former and all available data for the latter.

The mathematical basis is Bochner’s theorem [55], which states that any stationary kernel is the Fourier transform of a non-negative spectral measure. For the SE kernel in inverse-distance space, the spectral density is Gaussian:

$$k(\mathbf{x}, \mathbf{x}') = \sigma_f^2 \exp \left( - \sum_{(i,j)} \frac{(\phi_{ij}(\mathbf{x}) - \phi_{ij}(\mathbf{x}'))^2}{l_{\phi(i,j)}^2} \right) = \sigma_f^2 \int p(\boldsymbol{\omega}) e^{i\boldsymbol{\omega}^T(\phi(\mathbf{x}) - \phi(\mathbf{x}'))} d\boldsymbol{\omega} \quad (8.8)$$

where  $p(\boldsymbol{\omega}) = \mathcal{N}(\mathbf{0}, 2 \text{diag}(1/l_{\phi(i,j)}^2))$ . Drawing  $D_{\text{rff}}$  frequency vectors  $\boldsymbol{\omega}_m \sim p(\boldsymbol{\omega})$  and random phases  $b_m \sim \text{Uniform}[0, 2\pi)$ , the kernel is approximated by an inner product of finite-dimensional feature vectors:

$$k(\mathbf{x}, \mathbf{x}') \approx \mathbf{z}(\mathbf{x})^T \mathbf{z}(\mathbf{x}'), \quad z_m(\mathbf{x}) = \sigma_f \sqrt{\frac{2}{D_{\text{rff}}}} \cos(\boldsymbol{\omega}_m^T \phi(\mathbf{x}) + b_m) \quad (8.9)$$

This converts the GP from a kernel machine into a Bayesian linear regression problem in the  $D_{\text{rff}}$ -dimensional feature space. Training reduces to solving a linear system.

$$\boldsymbol{\alpha} = (\mathbf{Z}^T \boldsymbol{\Lambda} \mathbf{Z} + \mathbf{I})^{-1} \mathbf{Z}^T \boldsymbol{\Lambda} \mathbf{y} \quad (8.10)$$

where  $\mathbf{Z}$  is the  $n_{\text{obs}} \times D_{\text{rff}}$  design matrix and  $\boldsymbol{\Lambda} = \text{diag}(1/\sigma_E^2, \dots, 1/\sigma_F^2, \dots)$  contains the observation precisions. The cost is  $\mathcal{O}(n_{\text{obs}} \cdot D_{\text{rff}} + D_{\text{rff}}^3)$ , which replaces the exact GP cost of  $\mathcal{O}(n_{\text{obs}}^3)$ . For  $n_{\text{obs}} = 400$  and  $D_{\text{rff}} = 200$ , this is roughly a  $1000\times$  speedup. The predictive variance retains a closed form,  $\text{var}[f(\mathbf{x}_*)] = \mathbf{z}_*^T (\mathbf{Z}^T \boldsymbol{\Lambda} \mathbf{Z} + \mathbf{I})^{-1} \mathbf{z}_*$ , preserving the uncertainty-based acquisition that drives the active learning loop.

Derivative observations enter naturally through the chain rule. The Jacobian of the RFF feature vector with respect to Cartesian coordinates is:

$$\frac{\partial z_m}{\partial x_a} = -\sigma_f \sqrt{\frac{2}{D_{\text{rff}}}} \sin(\boldsymbol{\omega}_m^T \boldsymbol{\phi}(\mathbf{x}) + b_m) \sum_{(i,j)} \omega_{m,(i,j)} \frac{\partial \phi_{ij}}{\partial x_a} \quad (8.11)$$

where  $\partial \phi_{ij} / \partial x_a$  is the inverse-distance Jacobian (Eq. 3.13). Each gradient observation contributes a row of  $\mathbf{Z}$  via this Jacobian, so the design matrix has the same blocked structure (energy rows, then force rows) as the full covariance matrix. The difference is that the matrix dimensions are  $n_{\text{obs}} \times D_{\text{rff}}$  rather than  $n_{\text{obs}} \times n_{\text{obs}}$ , and  $D_{\text{rff}}$  is a user-chosen constant that does not grow with the data.

The conceptual connection to per-bead FPS is direct. In the exact GP, FPS selects a subset for hyperparameter optimization; all data is used for prediction, but the prediction cost is cubic in the total data size. RFF takes the separation one step further. The hyperparameters (which determine the spectral density  $p(\boldsymbol{\omega})$ ) are still optimized on the FPS subset at  $\mathcal{O}(M_{\text{sub}}^3)$  cost, and then the RFF model is built using *all* training data at the lower  $\mathcal{O}(n_{\text{obs}} \cdot D_{\text{rff}})$  cost. This two-stage strategy, hyperparameters from a subset, prediction from the full set, exploits the structural insight that kernel hyperparameters are global properties of the PES that can be estimated from a diverse subset, while prediction accuracy benefits from every available data point.

The division of labor is: FPS controls *which* data enters the hyperparameter optimization (bounding its  $\mathcal{O}(M_{\text{sub}}^3)$  cost), while RFF controls *how* prediction is performed on the full dataset (replacing the  $\mathcal{O}(M^3)$  exact solve with an  $\mathcal{O}(M \cdot D_{\text{rff}})$  linear regression). The two mechanisms are orthogonal and can be enabled independently, though they are most beneficial in combination.

The required  $D_{\text{rff}}$  depends on the dimensionality of the inverse-distance feature space (i.e., the number of atom pairs  $N_{\text{pairs}} = N(N-1)/2$ ), because the RFF must approximate the SE kernel in this space (Eq. 8.8). For 2D model surfaces (3 atoms, 3 inverse-distance features),  $D_{\text{rff}} \sim 50$ –100 suffices. For a 9-atom molecule (36 inverse-distance features),  $D_{\text{rff}} \sim 500$  is needed for the AIE variant to converge reliably; lower values (e.g., 300) introduce sufficient approximation error to stall the climbing-image convergence. As a practical rule,  $D_{\text{rff}} \gtrsim 10 N_{\text{pairs}}$  provides a reasonable starting point, though the exact threshold depends on the kernel length-scale spectrum and should be verified by comparing RFF predictions against the exact GP on held-out test points.

Figure 19 quantifies the RFF approximation quality on the LEPS surface (3 atoms, 3 inverse-distance features). The energy and gradient MAE between RFF and exact GP predictions are plotted against  $D_{\text{rff}}$  for held-out test configurations. The approximation error drops below  $10^{-4}$  eV by  $D_{\text{rff}} = 100$  and continues to decrease monotonically, confirming that low-dimensional kernels are well approximated by modest numbers of random features.

The computational savings from RFF scale favorably. For a training set of  $M$  configurations with  $N$  atoms each, the exact GP prediction requires  $\mathcal{O}((M(1+3N))^2)$  operations per test point (matrix-vector products with the inverse covariance), while RFF prediction costs  $\mathcal{O}(D_{\text{rff}} \cdot N_{\text{pairs}})$ . For a typical system with  $M = 50$  training points, this is a reduction from  $\sim 10^7$  to  $\sim 10^4$  operations per inner-loop prediction. In the NEB context, where each outer iteration may involve hundreds of inner-loop evaluations across  $P$  images, this per-evaluation speedup translates to a significant wall-clock reduction. The hyperparameter optimization remains the dominant cost, but because FPS bounds that at  $\mathcal{O}(M_{\text{sub}}^3)$  with  $M_{\text{sub}} \sim 10$ –30, the combined FPS+RFF strategy keeps the total GP overhead well below the electronic structure cost at each outer iteration.

The RFF extension presented here extends the OT-GP framework to larger systems across the Dimer, NEB and minimization. In practice, molecular systems benefit from a reduced GP tolerance divisor (e.g. 3 rather than 10) compared to toy surfaces, because the higher-dimensional surrogate is less reliable in extrapolation

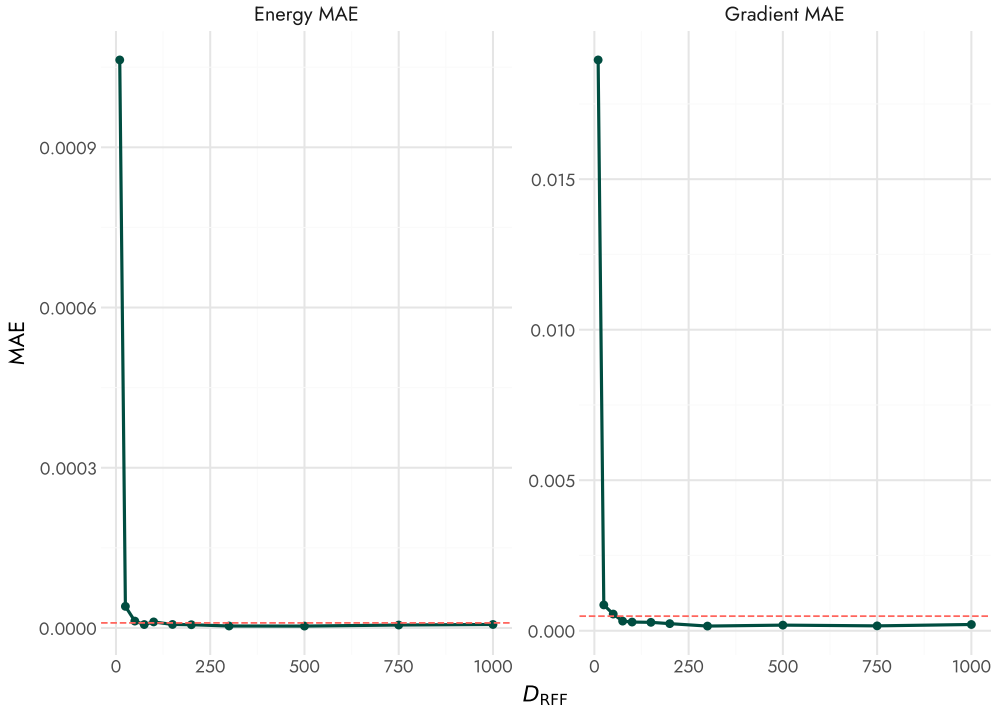


**Figure 19.** RFF approximation quality on the LEPS surface ( $\text{H}_3$ , 3 inverse-distance features). Energy MAE (top) and gradient MAE (bottom) between RFF and exact GP predictions on held-out test points, plotted against  $D_{\text{RFF}}$ . The kernel is well approximated by  $D_{\text{RFF}} \sim 100$ .

regions. Enabling RFF prediction in the OTGPD inner loop further stabilizes molecular runs by smoothing the surrogate away from training data, suppressing the oscillations that exact GP prediction can exhibit when the inverse-distance feature space is sparsely sampled.

## 9 Illustrative Examples

The chemgp-core crate includes three toy potentials (in `src/potentials.rs`: Muller-Brown, LEPS, and Lennard-Jones) that illustrate the algorithms on two-dimensional surfaces where the GP behavior can be visualized directly.

### 9.1 Muller-Brown Potential

The Muller-Brown surface [31] (Figure 12) is a standard benchmark for saddle point searches, with three minima and two saddle points connected by curved MEPs. Because the surface is two-dimensional, the GP behavior can be visualized directly: Figure 3 shows how the surrogate evolves from a crude approximation with few training points to a faithful replica of the true PES as data accumulates. The variance landscape (Figure 4) guides the active learning criterion, concentrating evaluations near the reaction path. The GP surface closely matches the true PES within the trust region (Figure 11), but diverges outside it, which is the expected behavior of a local surrogate. The NEB path connecting minima A and B through saddle S2 is shown in Figure 12.

### 9.2 LEPS Potential

The London-Eyring-Polanyi-Sato surface [98] (Figure 13) models a collinear atom-transfer reaction  $A + BC \rightarrow AB + C$ . The MEP has a single saddle point with pronounced curvature and is an ideal test for the GP-NEB (Figure 13). Classical NEB converges in 156 oracle evaluations and AIE in 100. The OIE variant converges in

40 outer iterations (42 total evaluations including endpoints), showing the efficiency of uncertainty-based image selection on a simple reaction coordinate (Figure 14).

### 9.3 PET-MAD Molecular System

The PET-MAD universal potential [18], trained on the MAD dataset [99], provides a realistic test beyond toy surfaces where the inverse-distance kernel operates on physical interatomic distances. For saddle point searches, Figure 9 compares the standard dimer, GP-dimer, and OTGPD on the  $C_{3H5}$  allyl radical (8 atoms, 24 DOF): the OTGPD converges with the fewest oracle calls, while the GP-dimer shows oscillations that the OT-GP extensions suppress. Figure 20 shows the convergence of GP-accelerated minimization on a molecular system, where the maximum per-atom force drops below the convergence threshold with significantly fewer oracle evaluations than the unaccelerated optimizer.

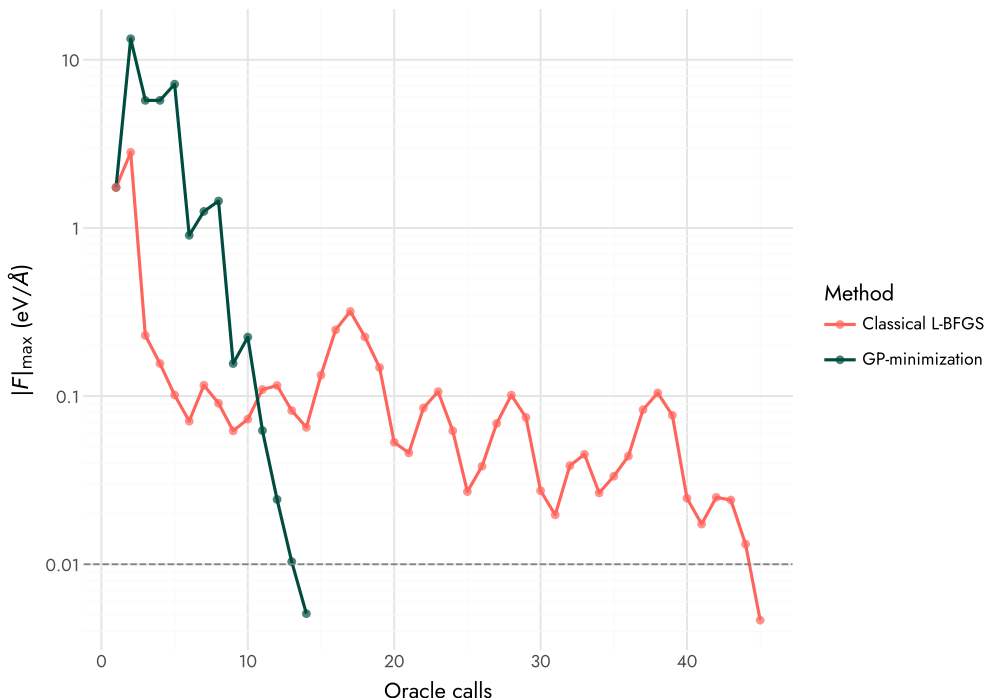


**Figure 20.** Convergence of GP-accelerated minimization on a real molecular system (PET-MAD potential). The maximum per-atom force is plotted against the number of oracle evaluations on a logarithmic scale.

For NEB, a 9-atom cycloaddition system ( $C_2H_4 + N_2O$ , 27 degrees of freedom, 36 inverse-distance features) on the PET-MAD surface illustrates how the GP-NEB variants scale to molecular reactions. Figure 21 compares classical NEB, AIE, and OIE on this system. A relaxed convergence threshold of  $0.5 \text{ eV}/\text{\AA}$  is used here for demonstration purposes; tighter tolerances are straightforward but require more evaluations and are better explored in a dedicated benchmarking study. Classical NEB converges in 102 oracle evaluations. The AIE variant converges in 42 evaluations, showing that the surrogate accelerates convergence even when all images are evaluated each cycle. The OIE variant evaluates only one image per cycle, selected by maximum predictive variance, and converges in 44 evaluations, a  $\sim 2.3\times$  reduction over classical NEB. Figure 22 shows the energy profiles along the converged MEP; all three variants recover the same barrier and exothermic product basin, confirming that the surrogate does not distort the path. Figure 23 shows the reaction valley projection [87] comparing the standard NEB and AIE saddle points; both paths lie within the low-variance region where the surrogate is well-trained, and the molecular snapshots along the bottom illustrate the structural progression from reactant to product.

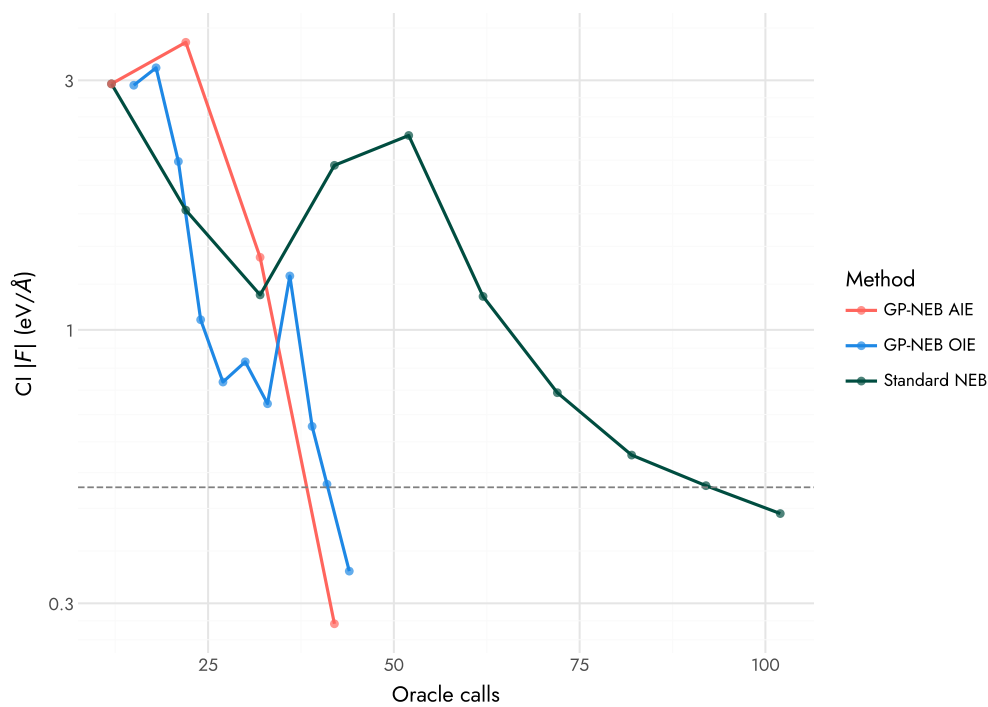


**Figure 21.** Convergence of GP-NEB variants on a 9-atom cycloaddition (PET-MAD surface, 27 DOF). Climbing image force versus oracle evaluations on a logarithmic scale. Classical NEB (102 calls), AIE (42 calls), and OIE (44 calls). Dashed line shows the convergence threshold.

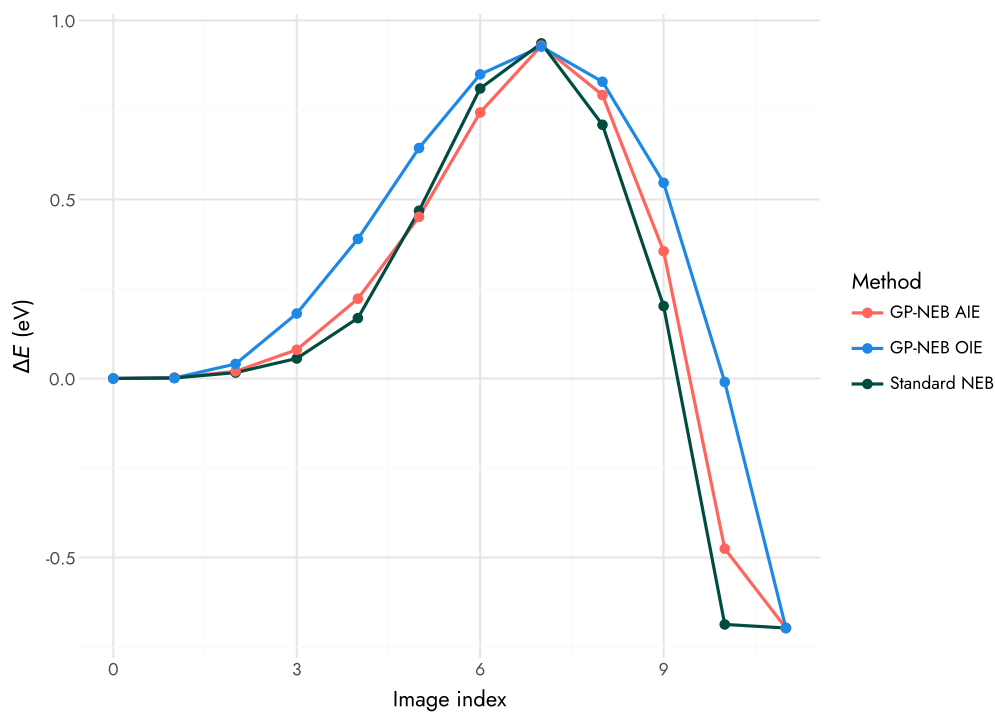


**Figure 22.** Energy profiles along the converged MEP for the cycloaddition system on the PET-MAD surface. All three NEB variants recover the same barrier and exothermic product basin. The AIE profile is slightly shifted near the saddle region but converges to the same endpoints.

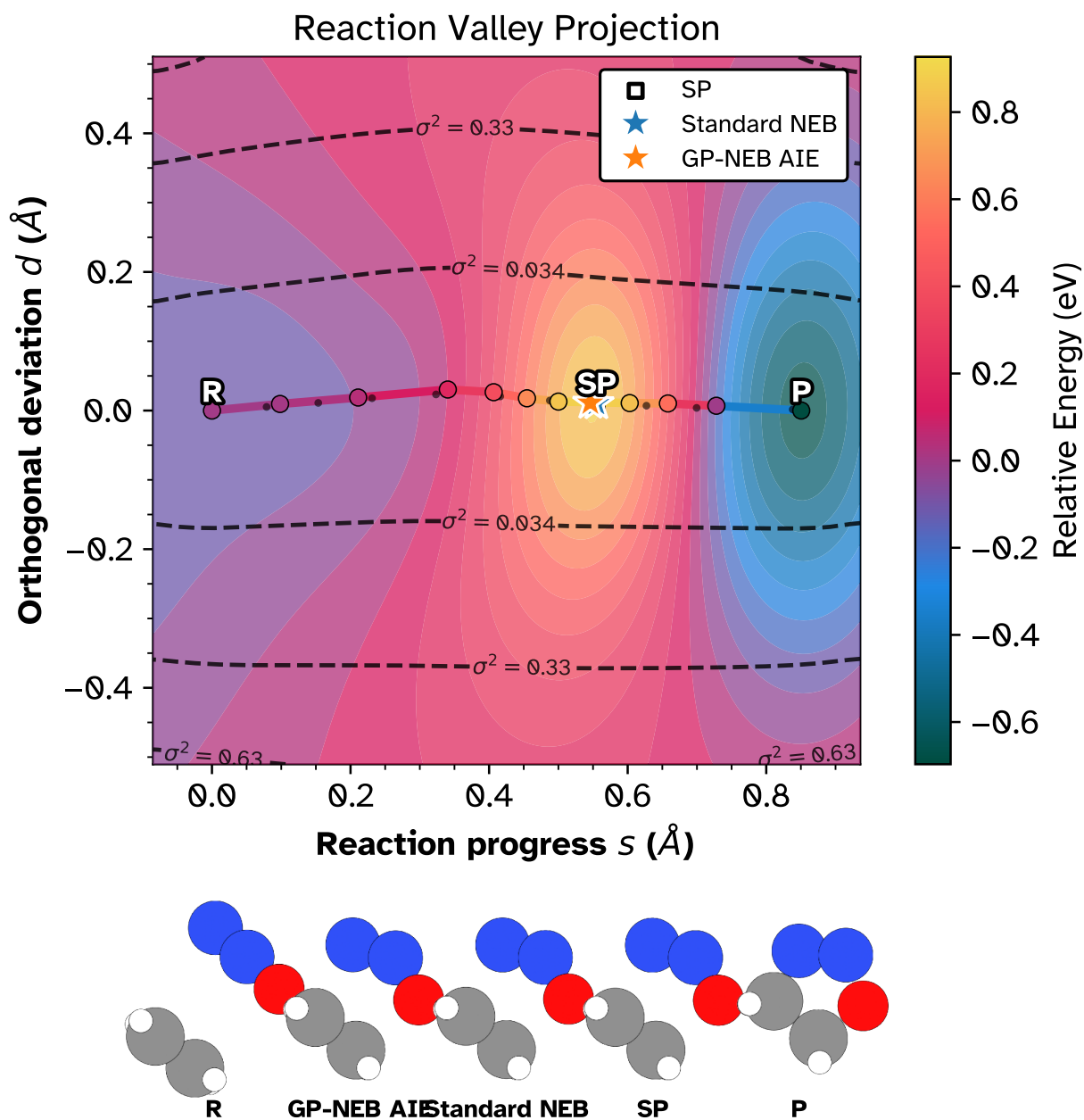


**Figure 23.** Reaction valley projection [87] of the NEB paths on the PET-MAD surface. Reaction progress  $s$  and orthogonal deviation  $d$  are projected RMSD coordinates. Standard NEB (blue stars) and GP-NEB AIE (orange stars) saddle points are compared; both lie near the true saddle (black square). Dashed contours show GP variance ( $\sigma^2$ ); the paths remain within the low-variance region where the surrogate is reliable. Bottom: molecular snapshots at key points along the reaction coordinate.

## 10 Conclusions

Gaussian process regression provides a practical framework for accelerating saddle point searches on potential energy surfaces. The local surrogate approach builds a GP on-the-fly from electronic structure evaluations during a single search, delivering a ten-fold reduction in computational cost compared to classical methods while preserving the accuracy of the underlying electronic structure theory.

The inverse-distance kernel delivers rotational and translational invariance through the feature map  $\phi_{ij} = 1/r_{ij}$ , and the learned length-scale parameters automatically identify which interatomic distances govern the reaction. This feature map also preconditions the PES by homogenizing the effective curvature, enabling accurate interpolation with a stationary kernel despite the wide range of stiffness in molecular systems. The analytical derivative blocks are essential for numerical stability; automatic differentiation through the inverse-distance computation introduces noise that destroys positive definiteness of the covariance matrix.

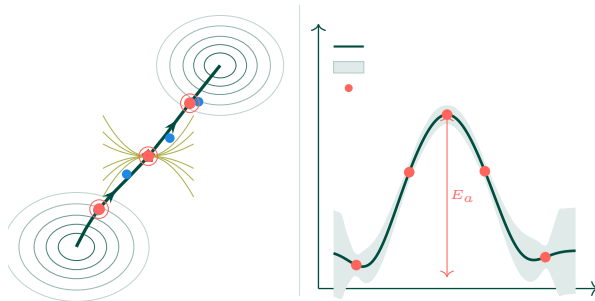
The primary goal of the methodology described is to forward the unification concept. Like optimizers, there are many modalities and choices, but all understood through a Bayesian optimization outer loop, from the origins to every method described in the literature thus far including state of the art methods. We have demonstrated how advanced concepts borrowed from statistical sciences can be applied holistically across stationary point searches.

The accompanying Rust code is a pedagogical reference, with documentation and plotting helpers and can be considered a primer to understanding performance bottlenecks and production interfaces. Each equation maps to a specific function, and the same binary runs the examples. The single-codebase design eliminates the gap between tutorial and deployment: the function that appears in the code listing is the function that runs the calculation.

It is expected that Bayesian methods will take root within the community and become an applied aspect of the field, much as optimization techniques have.

## Acknowledgements

The author thanks Prof. Birgir Hrafnkelsson, Prof. Thomas Bligaard, Dr. Andreas Vishart, and Dr. Miha Gunde for helpful discussions on the methodology. R.G. also acknowledges valuable discussions with Dr. Amrita Goswami, Dr. Moritz Sallermann, Prof. Debabrata Goswami, Mrs. Sonaly Goswami, and Mrs. Ruhila Goswami. Financial support from Dr. Guillaume Fraux and Prof. Michele Ceriotti of Lab-COSMO, EPFL is gratefully acknowledged. The figure color scheme was designed by Ruhila Goswami. The author thanks his family, pets, plants, birds, and garden creatures for their patience and support throughout this work.



GP surrogates accelerate saddle point searches on PES.

## 11 Supporting Information

**ignoreheading:appendix**

The following supplementary material provides additional details on algorithm flowcharts, marginal likelihood landscapes, hyperparameter defaults, and code implementation details.

## .1 Algorithm Flowcharts

The following flowcharts visualize the classical and GP-accelerated versions of the dimer method and NEB. Each pair shows the unmodified algorithm (left) alongside its GP-accelerated counterpart (right).

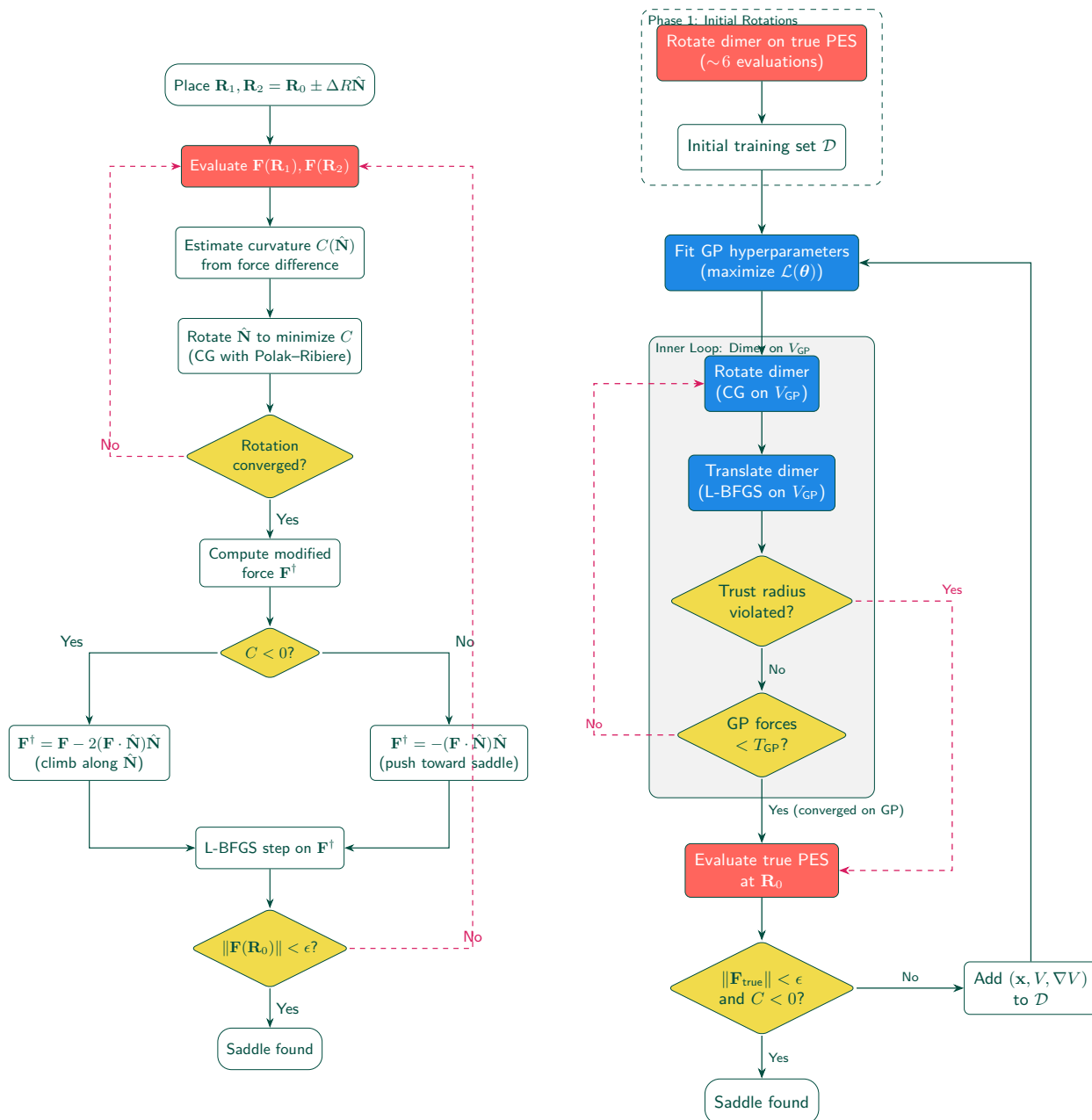


**Figure 24.** Classical dimer (left) and GP-dimer (right) flowcharts. The classical version evaluates the true PES at every rotation step; the GP-accelerated version performs rotations and translations on the surrogate surface, querying the oracle only when trust radius violations occur or GP-level convergence is achieved.

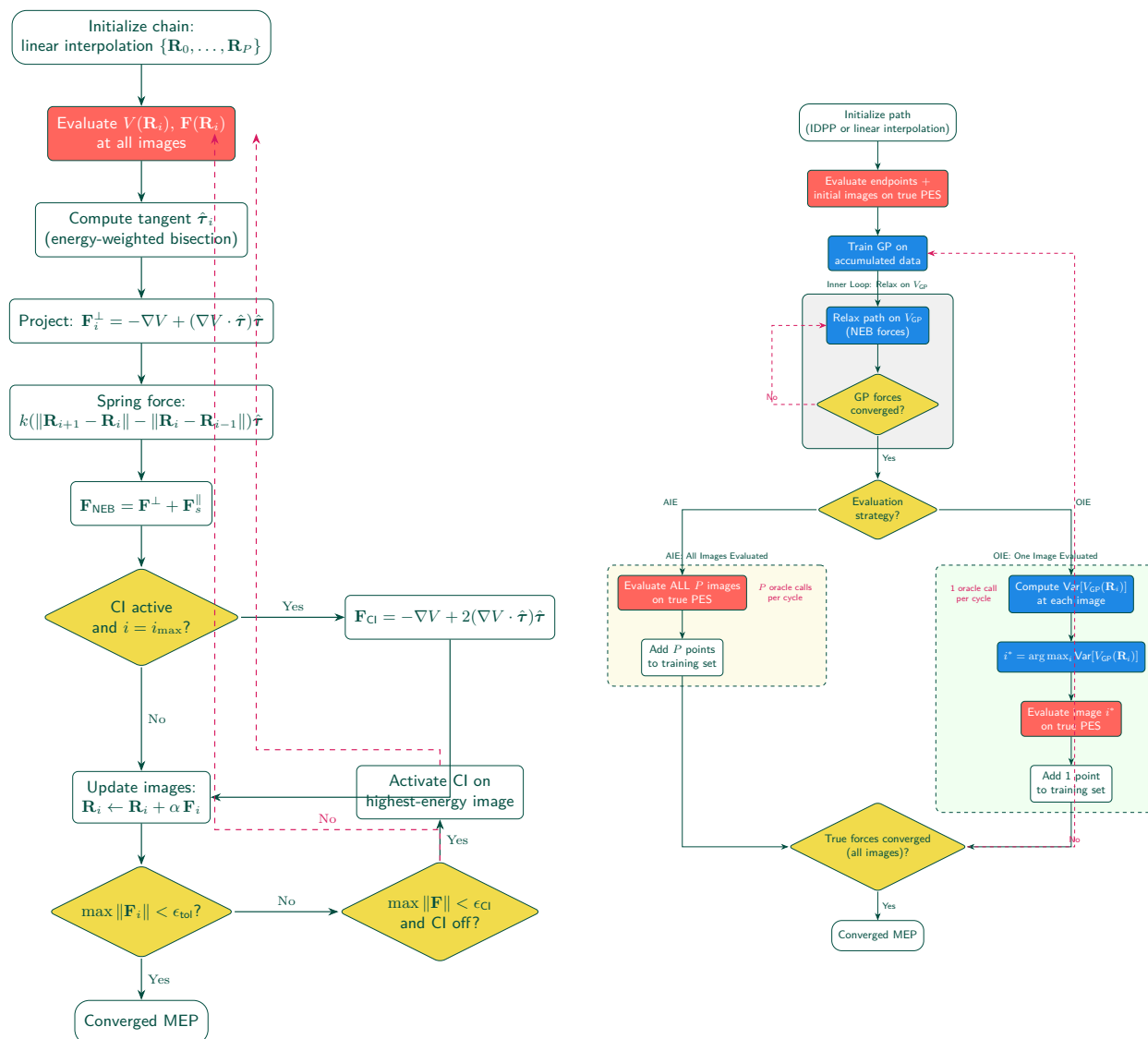


**Figure 25.** Classical NEB (left) and GP-NEB (right) flowcharts. The classical version optimizes all images via L-BFGS; the GP-NEB variant uses OIE acquisition to select a single image per outer loop iteration, minimizing oracle queries.

## A Marginal Likelihood Landscape

## B Hyperparameter Defaults

Table 4 collects default values for all hyperparameters used in GP-dimer, GP-NEB, and GP-minimization. These are starting values tuned for molecular systems with DFT energies (eV scale) and small to medium-sized systems (10-50 atoms). Adjustments may be needed for model potentials, very large systems, or different energy units.

## C Connection to Code: chemgp-core

The chemgp-core crate (<https://github.com/HaoZeke/ChemGP>) is both the pedagogical companion and the production implementation of the algorithms described in this review. Each listing below is extracted

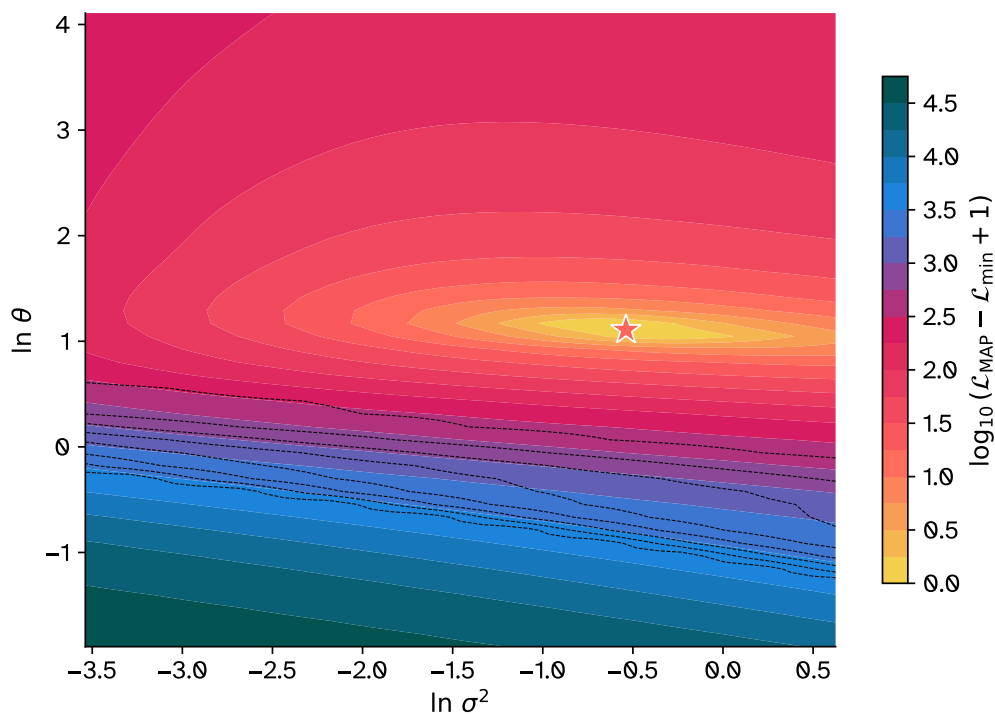


**Figure 26.** MAP-regularized negative log marginal likelihood landscape on the LEPS surface. The filled contours show the NLL as a function of the log-hyperparameters  $\ln \sigma^2$  and  $\ln \theta$ , computed on a  $40 \times 40$  grid from 5 training points near the reactant. The dashed black contours show the gradient norm. The coral star marks the MAP optimum that SCG converges to. Regions where the Cholesky factorization fails (hyperparameters that produce a non-positive-definite covariance matrix) are masked.

**Table 4.** Default hyperparameters for GP-accelerated saddle point searches. Parameters marked with <sup>†</sup> are documented in [38].

Parameter	Default	Meaning
<i>Kernel</i>		
$\sigma_c^2$	1.0	Constant offset (eV-scale energies); set to 0.0 for centered model surfaces
$\sigma_f^2$	Free (MLL)	Signal variance (optimized via MAP-NLL)
$l_{\phi(i,j)}$	Free (MLL)	Inverse-distance length scales (per atom-type pair, optimized)
<i>Noise and Regularization</i>		
$\sigma_E^2$	$10^{-8}$	Energy noise (Tikhonov regularizer, not physical noise)
$\sigma_F^2$	$10^{-8}$	Force noise (Tikhonov regularizer)
Jitter	$10^{-8} \max(\text{diag}(\mathbf{K}))$	Initial Cholesky jitter; grows $10\times$ per retry
<i>MAP Regularization<sup>†</sup></i>		
$\mu_0$	$10^{-4}$	Initial logarithmic barrier strength (Eq. 8.4)
$\alpha$	$10^{-3}$	Barrier growth rate with training set size
$\mu_{\max}$	0.5	Maximum barrier strength
$\lambda_{\max}$	$\ln(2)$	Upper bound for $\log \sigma_f^2$ (barrier ceiling)
<i>Dimer Method</i>		
$\Delta R$	0.01 Å	Dimer separation distance (Eq. 2.5)
$T_{\text{GP}}$	$10^{-3}$	GP-level force convergence threshold (eV/Å)
<i>FPS Subset Selection</i>		
$M_{\text{sub,init}}$	10	Initial FPS subset size
$M_{\text{sub,max}}$	30	Maximum subset size (after oscillation retries)
<i>Trust Radius</i>		
$T_{\min}$	0.1 Å	Minimum trust radius (per-atom EMD)
$\Delta T_{\text{explore}}$	0.4 Å	Exploration increment (saturation curve amplitude)
$N_{\text{half}}$	5	Half-life for exponential saturation (Eq. 8.6)
$a_{\text{floor}}$	0.3 Å	Minimum physical ceiling (small systems)
$a_A$	1.0 Å	Atomic length scale for size-dependent ceiling (Eq. 8.7)
<i>NEB Acquisition</i>		
$\kappa_{\text{UCB}}$	2.0	Exploration weight for Upper Confidence Bound (OIE)
<i>Random Fourier Features</i>		
$D_{\text{RFF}}$	200	Number of random features (for large training sets $M > 100$ )

from the crate source, and the same binary runs the benchmarks reported throughout. The crate was systematically aligned with the C++ `gpr\optim` code through a ten-fix campaign covering rotation fitting, convergence criteria, trust radius, and rigid-body projection; the algorithmic choices (SCG for hyperparameter optimization, Hungarian algorithm for EMD, adaptive trust radius) match the production C++ code. Table 5 summarizes the module correspondence.

**Table 5.** Conceptual mapping between mathematical ideas, chemgp-core Rust modules, and `gpr\optim` C++ classes. Both implementations share the same algorithmic structure; the Rust code runs the benchmarks reported in this review.

Concept	chemgp-core (Rust)	<code>gpr\optim</code> (C++)
Inverse-distance kernel	<code>kernel.rs</code> ( <code>MolInvDistSE</code> )	<code>InvDistSE</code>
Derivative kernel blocks	<code>kernel.rs</code> ( <code>molinvdist\_kernel\_blocks</code> )	<code>GPKernelBlocks</code>
GP training (SCG)	<code>train.rs</code> + <code>scg.rs</code> + <code>nll.rs</code>	<code>GPMoDel</code>
Dimer method	<code>dimer.rs</code> ( <code>gp\_dimer</code> )	<code>DimerSearch</code>
NEB method	<code>neb.rs</code> + <code>neb\_oie.rs</code>	<code>NEBSearch</code>
OT-GP Dimer	<code>otgpd.rs</code> ( <code>otgpd</code> )	<code>OTGPDimer</code>
FPS + EMD	<code>sampling.rs</code> + <code>emd.rs</code>	<code>FPSSampler</code> , <code>EMDDistance</code>
Trust regions	<code>trust.rs</code>	<code>TrustRegion</code>
Random Fourier features	<code>rff.rs</code> ( <code>build\_rff</code> )	<code>RFFModel</code>
L-BFGS	<code>lbfgs.rs</code> + <code>optim\_step.rs</code>	<code>LBFGS</code>
Constant kernel	<code>covariance.rs</code> + <code>rff.rs</code>	–

**Table 6.** Equation-to-function mapping for chemgp-core. Each equation in the main text maps to a specific function in the Rust implementation. The annotations in the code listings connect variable names to the mathematical symbols in the equations.

Equation	chemgp-core Function	Purpose
Eq. 2.6	<code>curvature()</code>	Dimer curvature estimate
Eq. 2.7	<code>rotational_force()</code>	CG rotation force
Eq. 2.8	<code>translational_force()</code>	Householder reflection
Eq. 2.10	<code>neb_force()</code>	NEB total force
Eq. 3.6–3.7	<code>molinvdist_kernel_blocks()</code>	Derivative covariance blocks
Eq. 3.8	<code>build_full_covariance()</code>	Assemble $\mathbf{K}_{\text{full}}$
Eq. 3.5	<code>robust_cholesky()</code>	Guarded Cholesky factorization
Eq. 3.3	<code>predict()</code>	Posterior mean prediction
Eq. 3.4	<code>predict_with_variance()</code>	Posterior mean + variance
Eq. 3.13	<code>invdist_jacobian()</code>	Inverse-distance Jacobian
Eq. 8.2–8.3	<code>emd_distance()</code>	EMD distance (per-type + overall)
Eq. 8.7	<code>adaptive_trust_threshold()</code>	Physical trust ceiling
Eq. 8.8	<code>build_rff()</code>	RFF model construction

The code snippets below are extracted from chemgp-core, with annotations connecting variables to the equations in the preceding sections. The same functions run the examples in this review and are deployed via the eOn saddle point search framework [79] for production calculations.

### C.1 Kernel Evaluation and Analytical Derivative Blocks

The kernel evaluation (Eq. 3.10) computes the squared Mahalanobis distance in inverse-distance feature space and applies the SE exponential. The variable `d2` accumulates the sum  $\sum_{(i,j)} \theta_{(i,j)}^2 (\phi_{ij}(\mathbf{x}) - \phi_{ij}(\mathbf{x}'))^2$ , where `inv_lengthscales` stores the  $\theta_{(i,j)} = 1/l_{\phi(i,j)}$  values and `compute_inverse_distances` returns the feature vector  $\phi(\mathbf{x})$ .

*Parameterization convention:* The paper’s kernel (Eq. 3.10) uses the standard SE form with a 1/2 factor in the exponent:  $k(\mathbf{x}, \mathbf{x}') = \sigma^2 \exp(-1/2 \sum_i (\phi_i(\mathbf{x}) - \phi_i(\mathbf{x}'))^2 / l_i^2)$ . The code absorbs the 1/2 into the inverse lengthscale definition, so  $\theta_{\text{code}} = 1/(l_{\text{paper}}\sqrt{2})$ . The two forms are mathematically equivalent; the code’s parameterization simplifies the derivative computation.

```
impl MolInvDistSE {
    pub fn eval(&self, x: &[f64], y: &[f64]) -> f64 {
        let fx = compute_inverse_distances(x, &self.frozen_coords);
        let fy = compute_inverse_distances(y, &self.frozen_coords);
```

```

let mut d2 = 0.0;
if !self.feature_params_map.is_empty() {
  for i in 0..fx.len() {
    let idx = self.feature_params_map[i];
    let val = (fx[i] - fy[i]) * self.inv_lengthscales[idx];
    d2 += val * val;
  }
} else {
  let theta = self.inv_lengthscales[0];
  for i in 0..fx.len() {
    let diff = fx[i] - fy[i];
    d2 += diff * diff;
  }
  d2 *= theta * theta;
}
self.signal_variance * (-d2).exp()
}
}

```

The derivative blocks (`kernel_blocks`, Listing S1 in the Supporting Information) compute the four covariance components between energy and force observations via chain rule through the inverse-distance Jacobian.

## C.2 Covariance Matrix Assembly and GP Training

The full covariance matrix (Eq. 3.8) is assembled by calling `kernel_blocks` for every pair of training configurations and placing the resulting  $2 \times 2$  block structure at the appropriate indices. For  $N$  training points with  $D = 3N_{\text{atoms}}$  coordinates each, the matrix has dimension  $N(1 + D) \times N(1 + D)$ : the first  $N$  rows/columns correspond to energies, and the remaining  $ND$  to forces. The noise variances  $\sigma_E^2$  and  $\sigma_F^2$  are added to the respective diagonal blocks.

```

pub fn build_full_covariance(
  kernel: &Kernel, x_data: &[f64], dim: usize, n: usize,
  noise_e: f64, noise_g: f64, jitter: f64, const_sigma2: f64,
) -> Mat<f64> {
  let total = n * (1 + dim);
  let mut k_mat = Mat::::zeros(total, total);
  for i in 0..n {
    let xi = &x_data[i * dim..(i + 1) * dim];
    let b = kernel.kernel_blocks(xi, xi);
    k_mat[(i, i)] = b.k_ee + const_sigma2 + noise_e + jitter; // const_sigma2: added to all
    E-E entries (rank-1 matrix sigma_c^2 * 11^T)
    let s_g = n + i * dim;
    for d in 0..dim {
      k_mat[(i, s_g + d)] = b.k_ef[d];
      k_mat[(s_g + d, i)] = b.k_fe[d];
      k_mat[(s_g + d, s_g + d)] += noise_g + jitter;
    }
    for di in 0..dim {
      for dj in 0..dim {
        k_mat[(s_g + di, s_g + dj)] = b.k_ff[(di, dj)];
      }
    }
  }
  for j in (i + 1)..n {
    let xj = &x_data[j * dim..(j + 1) * dim];
    let b = kernel.kernel_blocks(xi, xj);
    let j_s = n + j * dim;
    k_mat[(i, j)] = b.k_ee + const_sigma2;
    k_mat[(j, i)] = b.k_ee + const_sigma2;
    for d in 0..dim {

```

```

        k_mat[(i, j_s + d)] = b.k_ef[d];
        k_mat[(j_s + d, i)] = b.k_ef[d];
        k_mat[(s_g + d, j)] = b.k_fe[d];
        k_mat[(j, s_g + d)] = b.k_fe[d];
    }
    for di in 0..dim {
        for dj in 0..dim {
            k_mat[(s_g + di, j_s + dj)] = b.k_ff[(di, dj)];
            k_mat[(j_s + dj, s_g + di)] = b.k_ff[(di, dj)];
        }
    }
}
}
// Floor sub-epsilon entries (matches MATLAB GPstuff: C(C<eps)=0)
let eps = f64::EPSILON;
for r in 0..total {
    for c in 0..total {
        if k_mat[(r, c)].abs() < eps { k_mat[(r, c)] = 0.0; }
    }
}
k_mat
}

```

The training loop (`train_model`, Listing S2) minimizes the MAP-regularized NLL (Eq. 3.14) using the SCG optimizer [67] with log-space reparameterization.

The GP-dimer main loop (`gp_dimer`, Listing S3) alternates between outer iterations (oracle evaluations that grow the training set) and inner iterations (rotation and translation on the GP surface). Convergence requires both small translational force and negative curvature. The trust radius check (Eq. 5.2 or Eq. 8.5) breaks the inner loop when exceeded.

The GP-NEB OIE outer loop (`gp_neb_oie`, Listing S4) selects images via configurable acquisition strategies: `MaxVariance`, `Ucb` (NEB force plus perpendicular uncertainty), or `ExpectedImprovement`. A critical implementation detail: acquisition uses forces computed *before* inner relaxation, because re-predicting at relaxed positions with sparse training data produces unreliable NEB forces.

The RFF model (`build_rff`, Listing S5) replaces the exact GP with Bayesian linear regression in a random feature space sampled from the kernel’s spectral density (Section 8.4 of the main text). Prediction reduces to a dot product at  $\mathcal{O}(D_{\text{rff}})$  cost per component. Activating RFF is a single configuration change:

```

let config = NEBConfig {
    rff_features: 500,           // 0 = exact GP; >0 = RFF approximation
    max_gp_points: 40,         // per-bead subset for hyperparameter training
    acquisition: AcquisitionStrategy::Ucb,
    lcb_kappa: 2.0,           // UCB exploration weight
    const_sigma2: 0.0,        // constant kernel: 1.0 for molecular PES, 0.0 for models
    ..Default::default()
};

```

### C.3 Code Listings

The listings here cover the inverse-distance kernel derivative blocks (Listing S1), MAP-regularized hyperparameter training (Listing S2), GP-dimer main loop (Listing S3), GP-NEB OIE acquisition loop (Listing S4), and Random Fourier feature construction (Listing S5).

**Listing S1.** Derivative blocks for the inverse-distance kernel (`kernel_blocks`). The chain-rule structure projects the feature-space Hessian to Cartesian coordinates via the inverse-distance Jacobians.

```

pub fn molinvdist_kernel_blocks(
    k: &MolInvDistSE, x1: &[f64], x2: &[f64],
) -> KernelBlocks {

```

```

let (f1, j1) = invdist_jacobian(x1, &k.frozen_coords);
let (f2, j2) = invdist_jacobian(x2, &k.frozen_coords);
let nf = f1.len();

// Per-feature theta^2 values
let theta2: Vec<f64> = (0..nf).map(|i| {
    let idx = if k.feature_params_map.is_empty() { 0 }
              else { k.feature_params_map[i] };
    k.inv_lengthscales[idx].powi(2)
}).collect();

// SE kernel value
let r: Vec<f64> = (0..nf).map(|i| f1[i] - f2[i]).collect();
let d2: f64 = (0..nf).map(|i| theta2[i] * r[i] * r[i]).sum();
let kval = k.signal_variance * (-d2).exp();

// Feature-space gradient: dk/df
let mut dk_df2 = vec![0.0; nf];
let mut dk_df1 = vec![0.0; nf];
for i in 0..nf {
    let v = 2.0 * kval * theta2[i] * r[i];
    dk_df2[i] = v;
    dk_df1[i] = -v;
}

// Feature-space Hessian: H[i,j] = 2*kval*(theta2[i]*delta_ij - 2*u[i]*u[j])
let u: Vec<f64> = (0..nf).map(|i| theta2[i] * r[i]).collect();
let mut h_feat = Mat::<<f64>>::zeros(nf, nf);
for i in 0..nf {
    h_feat[(i, i)] = 2.0 * kval * (theta2[i] - 2.0 * u[i] * u[i]);
    for j in (i + 1)..nf {
        let val = -4.0 * kval * u[i] * u[j];
        h_feat[(i, j)] = val;
        h_feat[(j, i)] = val;
    }
}

// Chain rule: project to Cartesian coordinates
let k_ee = kval;
let k_ef = mat_t_vec(&j2, &dk_df2); // J2^T * dk/df2 (D x 1)
let k_fe = mat_t_vec(&j1, &dk_df1); // J1^T * dk/df1 (D x 1)
let k_ff = jt_h_j(&j1, &h_feat, &j2); // J1^T H J2 (D x D)
KernelBlocks { k_ee, k_ef, k_fe, k_ff }
}

```

**Listing S2.** MAP-regularized hyperparameter training via SCG (`train_model`). All hyperparameters are optimized in log-space; Cholesky failure returns infinity to reject infeasible configurations.

```

pub fn train_model(model: &mut GPModel, iterations: usize) {
    // Pack hyperparameters to log-space
    let mut w0 = Vec::

```

```

nll_and_grad(w, &model.x_data, model.dim, model.n_train,
            &model.y, &model.kernel, model.noise_var,
            model.grad_noise_var, model.jitter,
            &w_prior, &prior_var, model.const_sigma2,
            model.prior_dof, model.prior_s2, model.prior_mu)
};

let config = ScgConfig {
  max_iter: iterations,
  tol_f: 1e-4,
  lambda_init: model.scg_lambda_init,
  ..Default::default()
};

let result = scg_optimize(&mut fg, &w0, &config);
if result.converged || result.f_best < f64::INFINITY {
  let sigma2 = result.w_best[0].exp();
  let inv_ls: Vec<f64> =
    result.w_best[1..].iter().map(|v| v.exp()).collect();
  model.kernel = model.kernel.with_params(sigma2, inv_ls);
}
}

```

**Listing S3.** GP-dimer main loop (`gp_dimer`). The outer loop evaluates the oracle and grows the training set; the inner loop performs rotation and translation on the GP surface.

```

pub fn gp_dimer(
  oracle: &OracleFn, x_init: &[f64], orient_init: &[f64],
  kernel: &Kernel, config: &DimerConfig,
) -> DimerResult {
  let mut state = DimerState {
    r: x_init.to_vec(),
    orient: normalize_vec(orient_init),
    dimer_sep: config.dimer_sep,
  };
  let mut td = TrainingData::new(x_init.len());

  // Bootstrap: evaluate midpoint and one dimer endpoint
  let (e, g) = oracle(x_init);
  td.add_point(x_init, e, &g);
  let r1 = dimer_endpoint(&state);
  let (e1, g1) = oracle(&r1);
  td.add_point(&r1, e1, &g1);

  for _outer in 0..config.max_outer_iter {
    // FPS subset selection for hyperparameter training
    let td_sub = select_fps_subset(&td, &state.r, config);

    // Train GP on subset, predict on full data (RFF if configured)
    let mut gp = GPModel::new(kernel.clone(), &td_sub, ...);
    train_model(&mut gp, config.gp_train_iter);
    let model = build_pred_model(&gp.kernel, &td, config);

    // Inner loop: rotate + translate on GP surface
    for _inner in 0..config.max_inner_iter {
      rotate_dimer(&mut state, &model, config);
      let (g0, g1, _e0) = predict_dimer_gradients(&state, &model);
      let f_trans = translational_force(&g0, &state.orient);
      if vec_norm(&f_trans) < config.t_force_gp { break; }
    }
  }
}

```

```

    let r_new = translate_dimer_lbfgs(&state, &g0, &g1, config);
    if exceeds_trust(&r_new, &td, config) { break; }
    state.r = r_new;
}

// Evaluate oracle at proposed position
let (e_true, g_true) = oracle(&state.r);
td.add_point(&state.r, e_true, &g_true);

// Converge when true force is small AND curvature is negative
let f_true = translational_force(&g_true, &state.orient);
if vec_norm(&f_true) < config.t_force_true && curvature < 0.0 {
    return DimerResult { converged: true, oracle_calls: td.npoints(), .. };
}
}
DimerResult { converged: false, oracle_calls: td.npoints(), .. }
}
}

```

**Listing S4.** GP-NEB OIE acquisition loop (`gp_neb_oie`). The `select_image` function supports `MaxVariance`, `Ucb`, and `ExpectedImprovement` strategies.

```

pub fn gp_neb_oie(
    oracle: &OracleFn, x_start: &[f64], x_end: &[f64],
    kernel: &Kernel, config: &NEBConfig,
) -> NEBResult {
    let mut images = init_path(x_start, x_end, config);
    let mut td = TrainingData::new(x_start.len());

    // Evaluate endpoints and midpoint
    for x in &[x_start, x_end, &images[config.images / 2]] {
        let (e, g) = oracle(x);
        td.add_point(x, e, &g);
    }

    for _outer in 0..config.max_outer_iter {
        let model = train_and_build_model(&td, kernel, config);

        // Acquire: select unevaluated image by acquisition strategy
        let i_eval = select_image(
            &config.acquisition, &images, &energies,
            &unevaluated, &model, &cached_forces, config,
        );

        // Evaluate oracle at selected image
        let (e, g) = oracle(&images[i_eval]);
        td.add_point(&images[i_eval], e, &g);

        // Relax path on GP surface (L-BFGS inner loop)
        images = oie_inner_relax(&model, &images, &td, config);

        // Convergence check on true forces
        let max_f = compute_neb_forces(&images, &model, config).max_f;
        if max_f < config.conv_tol { /* verify unevaluated images */ }
    }
}
}

```

**Listing S5.** Random Fourier feature construction (`build_rff`). Frequency vectors are sampled from the kernel's spectral density (Bochner's theorem); the constant kernel adds one extra basis function.

```

pub fn build_rff(

```

```

kernel: &Kernel, x_train: &[f64], y_train: &[f64],
dim: usize, n: usize, d_rff: usize,
noise_var: f64, grad_noise_var: f64, seed: u64,
const_sigma2: f64,
) -> RffModel {
    let inv_ls = kernel.inv_lengthscales();
    let d_feat = kernel.n_features(dim);

    // Sample frequencies from N(0, 2*theta^2 * I) (Bochner's theorem)
    let mut rng = StdRng::seed_from_u64(seed);
    let mut w = Mat::<f64>::zeros(d_rff, d_feat);
    for f in 0..d_feat {
        let idx = kernel.pair_type_index(f);
        let scale = (2.0f64).sqrt() * inv_ls[idx];
        for i in 0..d_rff {
            w[(i, f)] = rng.sample::<f64, _>(StandardNormal) * scale;
        }
    }
    let b: Vec<f64> = (0..d_rff).map(|_| rng.random::<f64>()) * 2.0 * PI).collect();
    let c = kernel.signal_variance().sqrt() * (2.0 / d_rff as f64).sqrt();

    // Design matrix Z: d_eff = d_rff + 1 (extra column for const kernel)
    let d_eff = d_rff + 1;
    let n_obs = n * (1 + dim);
    let mut z = Mat::<f64>::zeros(n_obs, d_eff);
    for i in 0..n {
        let (zi, j_z) = rff_features(&w, &b, c, &x_train[i*dim..(i+1)*dim]);
        for f in 0..d_eff { z[(i, f)] = zi[f]; } // Eq. rff_features
        for d in 0..dim {
            for f in 0..d_eff { z[(n + i*dim + d, f)] = j_z[(f, d)]; }
        }
    }

    // Bayesian linear regression: A = Z^T diag(prec) Z + I
    let prec = build_precision(n, dim, noise_var, grad_noise_var);
    let a = zt_diag_z_plus_eye(&z, &prec, d_eff);
    let llt = a.llt(Side::Lower).expect("RFF Cholesky failed");
    let rhs = zt_diag_y(&z, &prec, y_train, d_eff);
    let alpha = llt.solve(&rhs);
    RffModel { w, b, c, alpha, a_chol: llt, dim, const_sigma2, .. }
}

```

## D Mathematical Derivations

### D.1 Rigid-Body Mode Basis Construction

The projection of rigid-body modes requires an orthonormal basis  $\{\mathbf{u}_k\}_{k=1}^6$  spanning the 6 external degrees of freedom. For a molecule with  $N$  atoms and Cartesian coordinates  $\mathbf{x} = (x_1, y_1, z_1, \dots, x_N, y_N, z_N)^T \in \mathbb{R}^{3N}$ , the six basis vectors correspond to three translations and three infinitesimal rotations.

The unnormalized translation vectors are:

$$\mathbf{t}_x = (1, 0, 0, 1, 0, 0, \dots, 1, 0, 0)^T, \quad (\text{D.1})$$

$$\mathbf{t}_y = (0, 1, 0, 0, 1, 0, \dots, 0, 1, 0)^T, \quad (\text{D.2})$$

$$\mathbf{t}_z = (0, 0, 1, 0, 0, 1, \dots, 0, 0, 1)^T. \quad (\text{D.3})$$

The unnormalized infinitesimal rotation vectors (about the molecular center of mass  $\mathbf{r}_0$ ) are:

$$\mathbf{r}_x = (0, z_1 - z_0, -(y_1 - y_0), \dots, 0, z_N - z_0, -(y_N - y_0))^T, \quad (\text{D.4})$$

$$\mathbf{r}_y = (-(z_1 - z_0), 0, x_1 - x_0, \dots, -(z_N - z_0), 0, x_N - x_0)^T, \quad (\text{D.5})$$

$$\mathbf{r}_z = (y_1 - y_0, -(x_1 - x_0), 0, \dots, y_N - y_0, -(x_N - x_0), 0)^T. \quad (\text{D.6})$$

where  $(x_i, y_i, z_i)$  are the coordinates of atom  $i$ , and  $(x_0, y_0, z_0)$  is the center of mass.

These six vectors are linearly independent but not orthonormal. The Gram-Schmidt process applied in the order  $(\mathbf{t}_x, \mathbf{t}_y, \mathbf{t}_z, \mathbf{r}_x, \mathbf{r}_y, \mathbf{r}_z)$  produces the orthonormal basis  $\{\mathbf{u}_k\}_{k=1}^6$ :

$$\mathbf{u}_1 = \frac{\mathbf{t}_x}{\|\mathbf{t}_x\|}, \quad (\text{D.7})$$

$$\mathbf{u}_2 = \frac{\mathbf{t}_y - (\mathbf{t}_y \cdot \mathbf{u}_1)\mathbf{u}_1}{\|\mathbf{t}_y - (\mathbf{t}_y \cdot \mathbf{u}_1)\mathbf{u}_1\|}, \quad (\text{D.8})$$

$$\mathbf{u}_3 = \frac{\mathbf{t}_z - \sum_{j=1}^2 (\mathbf{t}_z \cdot \mathbf{u}_j)\mathbf{u}_j}{\|\mathbf{t}_z - \sum_{j=1}^2 (\mathbf{t}_z \cdot \mathbf{u}_j)\mathbf{u}_j\|}, \quad (\text{D.9})$$

$$\mathbf{u}_{k+3} = \frac{\mathbf{r}_k - \sum_{j=1}^{k+2} (\mathbf{r}_k \cdot \mathbf{u}_j)\mathbf{u}_j}{\|\mathbf{r}_k - \sum_{j=1}^{k+2} (\mathbf{r}_k \cdot \mathbf{u}_j)\mathbf{u}_j\|}, \quad k \in \{x, y, z\}. \quad (\text{D.10})$$

In practice, the translation vectors are already orthogonal (and of equal norm  $\sqrt{N}$ ), so the Gram-Schmidt process only needs to orthogonalize the rotation vectors against the translations and against each other. This basis is computed once per molecular geometry and cached; the projection then costs  $\mathcal{O}(N)$  per step.

## D.2 Hyperparameter Oscillation Detection

The oscillation diagnostic mentioned in Section 8.2 of the main text detects when the MAP estimate of hyperparameters oscillates between competing local minima as new data arrives. For a hyperparameter vector  $\boldsymbol{\theta}(t) = (\theta_1(t), \dots, \theta_K(t))$  at outer iteration  $t$ , the per-component oscillation indicator is:

$$O_j(t) = \begin{cases} 1, & \text{if } (\theta_j(t) - \theta_j(t-1))(\theta_j(t-1) - \theta_j(t-2)) < 0, \\ 0, & \text{otherwise.} \end{cases} \quad (\text{D.11})$$

This indicator is 1 when hyperparameter  $j$  reverses direction (sign change in the gradient) between consecutive steps, and 0 otherwise. The fraction of oscillating components over a sliding window of length  $W$  (typically  $W = 5$  in chemgp-core) is:

$$f_{\text{osc}}(t) = \frac{1}{KW} \sum_{j=1}^K \sum_{s=t-W+1}^t O_j(s). \quad (\text{D.12})$$

When  $f_{\text{osc}}(t)$  exceeds a threshold  $p_{\text{osc}}$  (default  $p_{\text{osc}} = 0.8$  in chemgp-core), the algorithm detects instability and triggers growth of the FPS subset  $M_{\text{sub}}$  (Section 8.1). The subset grows incrementally (default: +2 points per retry) up to a maximum size (default: 30). This adaptive subset sizing sharpens the MLL landscape by adding geometrically diverse training data, constraining the optimizer to a narrower region of hyperparameter space.

## D.3 Kernel Block Structure

The full covariance matrix for derivative observations has a block structure that arises from the chain rule applied to the inverse-distance feature map. For two configurations  $\mathbf{x}_1$  and  $\mathbf{x}_2$ , the kernel blocks are:

$$k_{ee} = k(\phi(\mathbf{x}_1), \phi(\mathbf{x}_2)) \quad (\text{D.13})$$

$$k_{ef} = \frac{\partial k}{\partial \mathbf{x}_2} = \left( \frac{\partial k}{\partial \phi} \right)^T \frac{\partial \phi}{\partial \mathbf{x}_2} = \mathbf{J}_2^T \frac{\partial k}{\partial \phi} \quad (\text{D.14})$$

$$k_{fe} = \frac{\partial k}{\partial \mathbf{x}_1} = \mathbf{J}_1^T \frac{\partial k}{\partial \phi} \quad (\text{D.15})$$

$$k_{ff} = \frac{\partial^2 k}{\partial \mathbf{x}_1 \partial \mathbf{x}_2^T} = \mathbf{J}_1^T \left( \frac{\partial^2 k}{\partial \phi \partial \phi^T} - 2 \frac{\partial k}{\partial \phi} \otimes \frac{\partial \phi}{\partial \mathbf{x}_2} \right) \mathbf{J}_2 \quad (\text{D.16})$$

where  $\mathbf{J}_i = \partial \phi / \partial \mathbf{x}_i$  is the Jacobian of the feature map at configuration  $\mathbf{x}_i$ , and the feature-space Hessian is computed analytically for the SE kernel.

#### D.4 Earth Mover’s Distance for Trust Regions

The EMD-based trust region uses the per-type distance (Eq. 8.2) to compute a size-independent metric. For two configurations  $\mathbf{x}_1$  and  $\mathbf{x}_2$  with atom types  $\{t_i\}$ , the per-type distance is:

$$d_{\text{EMD}}^{(t)} = \min_{\pi \in \Pi_t} \sum_{i \in \mathcal{I}_t^{(1)}} \sum_{j \in \mathcal{I}_t^{(2)}} c_{ij}^{(t)} \pi_{ij} \quad (\text{D.17})$$

where  $\Pi_t$  is the set of joint distributions with marginals matching the counts of type  $t$  atoms, and  $c_{ij}^{(t)} = \|\mathbf{x}_1^{(i)} - \mathbf{x}_2^{(j)}\|$  is the ground cost. The overall EMD distance is the sum over all atom types:

$$d_{\text{EMD}}(\mathbf{x}_1, \mathbf{x}_2) = \sum_t w_t \cdot d_{\text{EMD}}^{(t)} \quad (\text{D.18})$$

where  $w_t$  are type-dependent weights (typically  $w_t = 1$  for all types).

#### D.5 OIE Acquisition Criterion Derivation

The Upper Confidence Bound (UCB) acquisition criterion for NEB OIE balances exploitation (large NEB forces) against exploration (high uncertainty). The criterion is:

$$\alpha(\mathbf{R}_i) = |\mathbf{F}_i^{\text{NEB}}| + \kappa \cdot \sigma_{\perp}(\mathbf{R}_i, \boldsymbol{\tau}_i) \quad (\text{D.19})$$

where  $\sigma_{\perp}$  is the perpendicular gradient variance (Eq. 4.1). This is derived from the Gaussian tail bound: with probability at least  $1 - \delta$ ,

$$|F_d^{\text{true}} - F_d^{\text{GP}}| \leq \kappa \cdot \sigma(F_d^{\text{GP}}), \quad \kappa = \sqrt{2 \log(1/\delta)} \quad (\text{D.20})$$

Applying this bound to the NEB force magnitude gives the UCB criterion as a conservative estimate of the true force magnitude.

## E References

### References

- [1] Peter Hänggi, Peter Talkner, and Michal Borkovec. Reaction-rate theory: Fifty years after Kramers. *Reviews of Modern Physics*, 62(2):251–341, April 1990. doi:10.1103/RevModPhys.62.251.
- [2] Henry Eyring. The activated complex in chemical reactions. *Journal of Chemical Physics*, 3(2):107–115, February 1935. ISSN 0021-9606. doi:10.1063/1.1749604.
- [3] George H. Vineyard. Frequency factors and isotope effects in solid state rate processes. *Journal of Physics and Chemistry of Solids*, 3(1):121–127, January 1957. ISSN 0022-3697. doi:10.1016/0022-3697(57)90059-8.

- 
- [4] Baron Peters. *Reaction Rate Theory and Rare Events*. Elsevier, Amsterdam ; Cambridge, MA, 2017. ISBN 978-0-444-56349-1.
- [5] Michele Re Fiorentin, Michele G. Bianchi, Magnus A. H. Christiansen, Anna Ciotti, Francesca Risplendi, Wei Wang, Elvar Ö. Jónsson, Hannes Jónsson, and Giancarlo Cicero. Methodological frameworks for computational electrocatalysis: From theory to practice. *Small Methods*, page e01542, February 2026. ISSN 2366-9608, 2366-9608. doi:[10.1002/smt.202501542](https://doi.org/10.1002/smt.202501542).
- [6] Gareth James, Daniela Witten, Trevor Hastie, and Robert Tibshirani. *An Introduction to Statistical Learning*, volume 103 of *Springer Texts in Statistics*. Springer New York, New York, NY, 2013. ISBN 978-1-4614-7137-0 978-1-4614-7138-7. doi:[10.1007/978-1-4614-7138-7](https://doi.org/10.1007/978-1-4614-7138-7).
- [7] D. Madsen, R. Pearman, and M. Gruebele. Approximate factorization of molecular potential surfaces. I. Basic approach. *Journal of Chemical Physics*, 106(14):5874–5893, April 1997. ISSN 0021-9606, 1089-7690. doi:[10.1063/1.473253](https://doi.org/10.1063/1.473253).
- [8] Giovanni Pizzi, Andrea Cepellotti, Riccardo Sabatini, Nicola Marzari, and Boris Kozinsky. AiiDA: Automated interactive infrastructure and database for computational science. *Computational Materials Science*, 111:218–230, January 2016. ISSN 0927-0256. doi:[10.1016/j.commatsci.2015.09.013](https://doi.org/10.1016/j.commatsci.2015.09.013).
- [9] Felix Mölder, Kim Philipp Jablonski, Brice Letcher, Michael B. Hall, Christopher H. Tomkins-Tinch, Vanessa Sochat, Jan Forster, Soohyun Lee, Sven O. Twardziok, Alexander Kanitz, Andreas Wilm, Manuel Holtgrewe, Sven Rahmann, Sven Nahnsen, and Johannes Köster. Sustainable data analysis with Snakemake, April 2021.
- [10] Graeme Henkelman and Hannes Jónsson. Long time scale kinetic Monte Carlo simulations without lattice approximation and predefined event table. *The Journal of Chemical Physics*, 115(21):9657–9666, November 2001. ISSN 0021-9606. doi:[10.1063/1.1415500](https://doi.org/10.1063/1.1415500).
- [11] Rohit Goswami. Efficient exploration of chemical kinetics, October 2025.
- [12] Felix Musil, Andrea Grisafi, Albert P. Bartók, Christoph Ortner, Gábor Csányi, and Michele Ceriotti. Physics-Inspired Structural Representations for Molecules and Materials. *Chemical Reviews*, 121(16): 9759–9815, August 2021. ISSN 0009-2665, 1520-6890. doi:[10.1021/acs.chemrev.1c00021](https://doi.org/10.1021/acs.chemrev.1c00021).
- [13] Andrea Grisafi, David M. Wilkins, Michael J. Willatt, and Michele Ceriotti. Atomic-Scale Representation and Statistical Learning of Tensorial Properties. In Edward O. Pyzer-Knapp and Teodoro Laino, editors, *ACS Symposium Series*, volume 1326, pages 1–21. American Chemical Society, Washington, DC, January 2019. ISBN 978-0-8412-3505-2 978-0-8412-3504-5. doi:[10.1021/bk-2019-1326.ch001](https://doi.org/10.1021/bk-2019-1326.ch001).
- [14] Albert Pártay Bartók. *The Gaussian Approximation Potential*. Springer Theses. Springer Berlin Heidelberg, Berlin, Heidelberg, 2010. ISBN 978-3-642-14066-2 978-3-642-14067-9. doi:[10.1007/978-3-642-14067-9](https://doi.org/10.1007/978-3-642-14067-9).
- [15] Alexander V. Shapeev. Moment Tensor Potentials: A Class of Systematically Improvable Interatomic Potentials. *Multiscale Modeling & Simulation*, 14(3):1153–1173, January 2016. ISSN 1540-3459. doi:[10.1137/15M1054183](https://doi.org/10.1137/15M1054183).
- [16] Jörg Behler and Michele Parrinello. Generalized Neural-Network Representation of High-Dimensional Potential-Energy Surfaces. *Physical Review Letters*, 98(14):146401, April 2007. doi:[10.1103/PhysRevLett.98.146401](https://doi.org/10.1103/PhysRevLett.98.146401).
- [17] Volker L. Deringer, Albert P. Bartók, Noam Bernstein, David M. Wilkins, Michele Ceriotti, and Gábor Csányi. Gaussian Process Regression for Materials and Molecules. *Chemical Reviews*, 121(16): 10073–10141, August 2021. ISSN 0009-2665, 1520-6890. doi:[10.1021/acs.chemrev.1c00022](https://doi.org/10.1021/acs.chemrev.1c00022).
- [18] Arslan Mazitov, Filippo Bigi, Matthias Kellner, Paolo Pegolo, Davide Tisi, Guillaume Fraux, Sergey Pozdnyakov, Philip Loche, and Michele Ceriotti. PET-MAD as a lightweight universal interatomic potential for advanced materials modeling. *Nature Communications*, 16(1):10653, November 2025. ISSN 2041-1723. doi:[10.1038/s41467-025-65662-7](https://doi.org/10.1038/s41467-025-65662-7).
- [19] Filippo Bigi, Paolo Pegolo, Arslan Mazitov, and Michele Ceriotti. Pushing the limits of unconstrained machine-learned interatomic potentials, January 2026.

- [20] Ilyes Batatia, Philipp Benner, Yuan Chiang, Alin M. Elena, Dávid P. Kovács, Janosh Riebesell, Xavier R. Advincula, Mark Asta, Matthew Avaylon, William J. Baldwin, Fabian Berger, Noam Bernstein, Arghya Bhowmik, Filippo Bigi, Samuel M. Blau, Vlad Cărare, Michele Ceriotti, Sanggyu Chong, James P. Darby, Sandip De, Flaviano Della Pia, Volker L. Deringer, Rokas Elijošius, Zakariya El-Machachi, Edvin Fako, Fabio Falcioni, Andrea C. Ferrari, John L. A. Gardner, Mikołaj J. Gawkowski, Annalena Genreith-Schriever, Janine George, Rhys E. A. Goodall, Jonas Grandel, Clare P. Grey, Petr Grigorev, Shuang Han, Will Handley, Hendrik H. Heenen, Kersti Hermansson, Cheuk Hin Ho, Stephan Hofmann, Christian Holm, Jad Jaafar, Konstantin S. Jakob, Hyunwook Jung, Venkat Kapil, Aaron D. Kaplan, Nima Karimitari, James R. Kermode, Panagiotis Kourtis, Namu Kroupa, Jolla Kullgren, Matthew C. Kuner, Domantas Kuryla, Guoda Liepuoniute, Chen Lin, Johannes T. Margraf, Ioan-Bogdan Magdău, Angelos Michaelides, J. Harry Moore, Aakash A. Naik, Samuel P. Niblett, Sam Walton Norwood, Niamh O'Neill, Christoph Ortner, Kristin A. Persson, Karsten Reuter, Andrew S. Rosen, Louise A. M. Rosset, Lars L. Schaaf, Christoph Schran, Benjamin X. Shi, Eric Sivonxay, Tamás K. Stenczel, Christopher Sutton, Viktor Svahn, Thomas D. Swinburne, Jules Tilly, Cas van der Oord, Santiago Vargas, Eszter Varga-Umbrich, Tejs Vegge, Martin Vondrák, Yangshuai Wang, William C. Witt, Thomas Wolf, Fabian Zills, and Gábor Csányi. A foundation model for atomistic materials chemistry. *Journal of Chemical Physics*, 163(18), November 2025. ISSN 0021-9606. doi:[10.1063/5.0297006](https://doi.org/10.1063/5.0297006).
- [21] Mathias Schreiner, Arghya Bhowmik, Tejs Vegge, Jonas Busk, and Ole Winther. Transition1x - a dataset for building generalizable reactive machine learning potentials. *Scientific Data*, 9(1):779, December 2022. ISSN 2052-4463. doi:[10.1038/s41597-022-01870-w](https://doi.org/10.1038/s41597-022-01870-w).
- [22] Philipp Hennig. Probabilistic Machine Learning, September 2023.
- [23] Richard S. Sutton and Andrew G. Barto. *Reinforcement Learning: An Introduction*. Adaptive Computation and Machine Learning Series. The MIT Press, Cambridge, Massachusetts, second edition edition, 2018. ISBN 978-0-262-03924-6.
- [24] Jasper Snoek, Hugo Larochelle, and Ryan P Adams. Practical Bayesian Optimization of Machine Learning Algorithms. In *Advances in Neural Information Processing Systems*, volume 25. Curran Associates, Inc., 2012.
- [25] Rohit Goswami, Maxim Masterov, Satish Kamath, Alejandro Pena-Torres, and Hannes Jónsson. Efficient Implementation of Gaussian Process Regression Accelerated Saddle Point Searches with Application to Molecular Reactions. *Journal of Chemical Theory and Computation*, July 2025. doi:[10.1021/acs.jctc.5c00866](https://doi.org/10.1021/acs.jctc.5c00866).
- [26] Andrew Gelman, John B Carlin, Hal S Stern, David B Dunson, Aki Vehtari, and Donald B Rubin. Bayesian Data Analysis Third edition (with errors fixed as of 15 February 2021). page 677.
- [27] Robert B. Gramacy. *Surrogates: Gaussian Process Modeling, Design, and Optimization for the Applied Sciences*. CRC Press ; Taylor & Francis Group, New York, NY, 2020. ISBN 978-0-367-41542-6.
- [28] Miguel A. Caro. Optimizing many-body atomic descriptors for enhanced computational performance of machine learning based interatomic potentials. *Physical Review B*, 100(2):024112, July 2019. doi:[10.1103/PhysRevB.100.024112](https://doi.org/10.1103/PhysRevB.100.024112).
- [29] Olli-Pekka Koistinen, Vilhjálmur Ásgeirsson, Aki Vehtari, and Hannes Jónsson. Nudged Elastic Band Calculations Accelerated with Gaussian Process Regression Based on Inverse Interatomic Distances. *Journal of Chemical Theory and Computation*, 15(12):6738–6751, December 2019. ISSN 1549-9618. doi:[10.1021/acs.jctc.9b00692](https://doi.org/10.1021/acs.jctc.9b00692).
- [30] Errol G. Lewars. *Computational Chemistry*. Springer International Publishing, Cham, 2016. ISBN 978-3-319-30914-9 978-3-319-30916-3. doi:[10.1007/978-3-319-30916-3](https://doi.org/10.1007/978-3-319-30916-3).
- [31] Klaus Müller and Leo D. Brown. Location of saddle points and minimum energy paths by a constrained simplex optimization procedure. *Theoretica chimica acta*, 53(1):75–93, March 1979. ISSN 1432-2234. doi:[10.1007/BF00547608](https://doi.org/10.1007/BF00547608).
- [32] Graeme Henkelman and Hannes Jónsson. A dimer method for finding saddle points on high dimensional potential surfaces using only first derivatives. *The Journal of Chemical Physics*, 111(15):7010–7022, October 1999. ISSN 0021-9606, 1089-7690. doi:[10.1063/1.480097](https://doi.org/10.1063/1.480097).

- 
- [33] Hannes Jonsson, Greg Mills, and Karsten W. Jacobsen. Nudged elastic band method for finding minimum energy paths of transitions. In *Classical and Quantum Dynamics in Condensed Phase Simulations*, pages 385–404. World Scientific, June 1998. ISBN 978-981-02-3498-0. doi:[10.1142/9789812839664\\_0016](https://doi.org/10.1142/9789812839664_0016).
- [34] Graeme Henkelman, Blas P. Uberuaga, and Hannes Jónsson. A climbing image nudged elastic band method for finding saddle points and minimum energy paths. *The Journal of Chemical Physics*, 113(22): 9901–9904, November 2000. ISSN 0021-9606. doi:[10.1063/1.1329672](https://doi.org/10.1063/1.1329672).
- [35] Dong C. Liu and Jorge Nocedal. On the limited memory BFGS method for large scale optimization. *Mathematical Programming*, 45(1):503–528, August 1989. ISSN 1436-4646. doi:[10.1007/BF01589116](https://doi.org/10.1007/BF01589116).
- [36] Richard H. Byrd, Peihuang Lu, Jorge Nocedal, and Ciyou Zhu. A limited memory algorithm for bound constrained optimization. *SIAM Journal on Scientific Computing*, 16:1190–1208, September 1995. ISSN 1064-8275. doi:[10.1137/0916069](https://doi.org/10.1137/0916069).
- [37] Jorge Nocedal and Stephen J. Wright. *Numerical Optimization*. Springer Series in Operations Research. Springer, New York, 2nd ed edition, 2006. ISBN 978-0-387-30303-1.
- [38] Rohit Goswami and Hannes Jónsson. Adaptive Pruning for Increased Robustness and Reduced Computational Overhead in Gaussian Process Accelerated Saddle Point Searches. *ChemPhysChem*, November 2025. ISSN 1439-7641. doi:[10.1002/cphc.202500730](https://doi.org/10.1002/cphc.202500730).
- [39] Olli-Pekka Koistinen, Vilhjálmur Ásgeirsson, Aki Vehtari, and Hannes Jónsson. Minimum Mode Saddle Point Searches Using Gaussian Process Regression with Inverse-Distance Covariance Function. *Journal of Chemical Theory and Computation*, 16(1):499–509, January 2020. ISSN 1549-9618. doi:[10.1021/acs.jctc.9b01038](https://doi.org/10.1021/acs.jctc.9b01038).
- [40] Alexander Denzel and Johannes Kästner. Gaussian Process Regression for Transition State Search. *Journal of Chemical Theory and Computation*, 14(11):5777–5786, November 2018. ISSN 1549-9618. doi:[10.1021/acs.jctc.8b00708](https://doi.org/10.1021/acs.jctc.8b00708).
- [41] James F Epperson. An Introduction to Numerical Methods and Analysis. page 615, 2012.
- [42] E. Polak and G. Ribiere. Note sur la convergence de méthodes de directions conjuguées. *Revue française d’informatique et de recherche opérationnelle. Série rouge*, 3(16):35–43, 1969. ISSN 0373-8000. doi:[10.1051/m2an/196903R100351](https://doi.org/10.1051/m2an/196903R100351).
- [43] Andreas Heyden, Alexis T. Bell, and Frerich J. Keil. Efficient methods for finding transition states in chemical reactions: Comparison of improved dimer method and partitioned rational function optimization method. *The Journal of Chemical Physics*, 123(22):224101, December 2005. ISSN 0021-9606. doi:[10.1063/1.2104507](https://doi.org/10.1063/1.2104507).
- [44] Johannes Kästner and Paul Sherwood. Superlinearly converging dimer method for transition state search. *The Journal of Chemical Physics*, 128(1):014106, January 2008. ISSN 0021-9606. doi:[10.1063/1.2815812](https://doi.org/10.1063/1.2815812).
- [45] R. A. Olsen, G. J. Kroes, G. Henkelman, A. Arnaldsson, and H. Jónsson. Comparison of methods for finding saddle points without knowledge of the final states. *The Journal of Chemical Physics*, 121(20): 9776–9792, November 2004. ISSN 0021-9606. doi:[10.1063/1.1809574](https://doi.org/10.1063/1.1809574).
- [46] Rohit Goswami. Bayesian hierarchical models for quantitative estimates for performance metrics applied to saddle search algorithms. *AIP Advances*, 15(8):85210, August 2025. ISSN 2158-3226. doi:[10.1063/5.0283639](https://doi.org/10.1063/5.0283639).
- [47] Jing Leng, Weiguo Gao, Cheng Shang, and Zhi-Pan Liu. Efficient softest mode finding in transition states calculations. *Journal of Chemical Physics*, 138(9):94110, March 2013. ISSN 0021-9606. doi:[10.1063/1.4792644](https://doi.org/10.1063/1.4792644).
- [48] Marko Melander, Kari Laasonen, and Hannes Jónsson. Removing External Degrees of Freedom from Transition-State Search Methods using Quaternions. *Journal of Chemical Theory and Computation*, 11(3):1055–1062, March 2015. ISSN 1549-9618. doi:[10.1021/ct501155k](https://doi.org/10.1021/ct501155k).
- [49] Weinan E, Weiqing Ren, and Eric Vanden-Eijnden. String method for the study of rare events. *Physical Review B*, 66(5):52301, August 2002. doi:[10.1103/PhysRevB.66.052301](https://doi.org/10.1103/PhysRevB.66.052301).

- 
- [50] Weinan E, Weiqing Ren, and Eric Vanden-Eijnden. Simplified and improved string method for computing the minimum energy paths in barrier-crossing events. *The Journal of Chemical Physics*, 126(16):164103, April 2007. ISSN 0021-9606, 1089-7690. doi:[10.1063/1.2720838](https://doi.org/10.1063/1.2720838).
- [51] Daniel Sheppard, Rye Terrell, and Graeme Henkelman. Optimization methods for finding minimum energy paths. *The Journal of Chemical Physics*, 128(13):134106, April 2008. ISSN 0021-9606. doi:[10.1063/1.2841941](https://doi.org/10.1063/1.2841941).
- [52] Vilhjálmur Ásgeirsson, Benedikt Orri Birgisson, Ragnar Bjornsson, Ute Becker, Frank Neese, Christoph Riplinger, and Hannes Jónsson. Nudged Elastic Band Method for Molecular Reactions Using Energy-Weighted Springs Combined with Eigenvector Following. *Journal of Chemical Theory and Computation*, 17(8):4929–4945, August 2021. ISSN 1549-9618. doi:[10.1021/acs.jctc.1c00462](https://doi.org/10.1021/acs.jctc.1c00462).
- [53] Graeme Henkelman and Hannes Jónsson. Improved tangent estimate in the nudged elastic band method for finding minimum energy paths and saddle points. *The Journal of Chemical Physics*, 113(22):9978–9985, December 2000. ISSN 0021-9606. doi:[10.1063/1.1323224](https://doi.org/10.1063/1.1323224).
- [54] Rohit Goswami, Miha Gunde, and Hannes Jónsson. Enhanced climbing image nudged elastic band method with hessian eigenmode alignment, January 2026.
- [55] Carl Edward Rasmussen and Christopher K. I. Williams. *Gaussian Processes for Machine Learning*. Adaptive Computation and Machine Learning. MIT Press, Cambridge, Mass, 2006. ISBN 978-0-262-18253-9.
- [56] E. Solak, R. Murray-smith, W. Leithead, D. Leith, and Carl Rasmussen. Derivative observations in gaussian process models of dynamic systems. In S. Becker, S. Thrun, and K. Obermayer, editors, *Advances in Neural Information Processing Systems*, volume 15. MIT Press, 2002.
- [57] Mykel J Kochenderfer and Tim A Wheeler. *Algorithms for Optimization*.
- [58] Albert P. Bartók, Risi Kondor, and Gábor Csányi. On representing chemical environments. *Physical Review B*, 87(18):184115, May 2013. doi:[10.1103/PhysRevB.87.184115](https://doi.org/10.1103/PhysRevB.87.184115).
- [59] Ralf Drautz. Atomic cluster expansion for accurate and transferable interatomic potentials. *Physical Review B*, 99(1):014104, January 2019. doi:[10.1103/PhysRevB.99.014104](https://doi.org/10.1103/PhysRevB.99.014104).
- [60] Ignacio Fdez. Galván, Gerardo Raggi, and Roland Lindh. Restricted-Variance Constrained, Reaction Path, and Transition State Molecular Optimizations Using Gradient-Enhanced Kriging. *Journal of Chemical Theory and Computation*, 17(1):571–582, January 2021. ISSN 1549-9618. doi:[10.1021/acs.jctc.0c01163](https://doi.org/10.1021/acs.jctc.0c01163).
- [61] Casper Larsen, Sami Kaappa, Andreas Lynge Vishart, Thomas Bligaard, and Karsten Wedel Jacobsen. Machine-learning-enabled optimization of atomic structures using atoms with fractional existence. *Physical Review B*, 107(21):214101, June 2023. doi:[10.1103/PhysRevB.107.214101](https://doi.org/10.1103/PhysRevB.107.214101).
- [62] Andreas Lynge Vishart. *Accelerating Catalysis Simulations Using Surrogate Machine Learning Models*. PhD thesis.
- [63] Olli-Pekka Koistinen. *Algorithms for Finding Saddle Points and Minimum Energy Paths Using Gaussian Process Regression*. PhD thesis, Aalto University School of Science, 2019.
- [64] Matthias Rupp, Alexandre Tkatchenko, Klaus-Robert Müller, and O. Anatole von Lilienfeld. Fast and Accurate Modeling of Molecular Atomization Energies with Machine Learning. *Physical Review Letters*, 108(5):058301, January 2012. ISSN 0031-9007, 1079-7114. doi:[10.1103/PhysRevLett.108.058301](https://doi.org/10.1103/PhysRevLett.108.058301).
- [65] Kai Cheng and Ralf Zimmermann. Sliced gradient-enhanced kriging for high-dimensional function approximation. *SIAM Journal on Scientific Computing*.
- [66] Selvakumar Ulaganathan, Ivo Couckuyt, Tom Dhaene, Joris Degroote, and Eric Laermans. Performance study of gradient-enhanced kriging. *Engineering with Computers*, 32(1):15–34, February 2015. ISSN 1435-5663. doi:[10.1007/s00366-015-0397-y](https://doi.org/10.1007/s00366-015-0397-y).
- [67] Martin Fodstlette Møller. A scaled conjugate gradient algorithm for fast supervised learning. *Neural Networks*, 6(4):525–533, January 1993. ISSN 0893-6080. doi:[10.1016/S0893-6080\(05\)80056-5](https://doi.org/10.1016/S0893-6080(05)80056-5).
- [68] Filippo Bigi, Sergey N. Pozdnyakov, and Michele Ceriotti. Wigner kernels: Body-ordered equivariant machine learning without a basis. *Journal of Chemical Physics*, 161(4), 2024. doi:[10.1063/5.0208746](https://doi.org/10.1063/5.0208746).

- [69] Estefanía Garijo del Río, Sami Kaappa, José A. Garrido Torres, Thomas Bligaard, and Karsten Wedel Jacobsen. Machine learning with bond information for local structure optimizations in surface science. *The Journal of Chemical Physics*, 153(23):234116, December 2020. ISSN 0021-9606, 1089-7690. doi:[10.1063/5.0033778](https://doi.org/10.1063/5.0033778).
- [70] Estefanía Garijo del Río, Jens Jørgen Mortensen, and Karsten Wedel Jacobsen. Local Bayesian optimizer for atomic structures. *Physical Review B*, 100(10):104103, September 2019. doi:[10.1103/PhysRevB.100.104103](https://doi.org/10.1103/PhysRevB.100.104103).
- [71] Amar Shah, Andrew Gordon Wilson, and Zoubin Ghahramani. Student-t Processes as Alternatives to Gaussian Processes.
- [72] Alexander Denzel and Johannes Kästner. Gaussian process regression for geometry optimization. *The Journal of Chemical Physics*, 148(9):094114, March 2018. ISSN 0021-9606. doi:[10.1063/1.5017103](https://doi.org/10.1063/1.5017103).
- [73] Donald R. Jones, Matthias Schonlau, and William J. Welch. Efficient Global Optimization of Expensive Black-Box Functions. *Journal of Global Optimization*, 13(4):455–492, December 1998. ISSN 1573-2916. doi:[10.1023/A:1008306431147](https://doi.org/10.1023/A:1008306431147).
- [74] Bobak Shahriari, Kevin Swersky, Ziyu Wang, Ryan P. Adams, and Nando de Freitas. Taking the Human Out of the Loop: A Review of Bayesian Optimization. *Proceedings of the IEEE*, 104(1):148–175, January 2016. ISSN 0018-9219, 1558-2256. doi:[10.1109/JPROC.2015.2494218](https://doi.org/10.1109/JPROC.2015.2494218).
- [75] P Hennig, M A Osborne, and H P Kersting. *Probabilistic Numerics*.
- [76] José A. Garrido Torres, Paul C. Jennings, Martin H. Hansen, Jacob R. Boes, and Thomas Bligaard. Low-Scaling Algorithm for Nudged Elastic Band Calculations Using a Surrogate Machine Learning Model. *Physical Review Letters*, 122(15):156001, April 2019. doi:[10.1103/PhysRevLett.122.156001](https://doi.org/10.1103/PhysRevLett.122.156001).
- [77] Niranjana Srinivas, Andreas Krause, Sham Kakade, and Matthias Seeger. Gaussian process optimization in the bandit setting: No regret and experimental design. In *Proceedings of the 27th International Conference on International Conference on Machine Learning*, ICML'10, pages 1015–1022, Madison, WI, USA, June 2010. Omnipress. ISBN 978-1-60558-907-7.
- [78] Andrew A. Peterson. Acceleration of saddle-point searches with machine learning. *The Journal of Chemical Physics*, 145(7):074106, August 2016. ISSN 0021-9606. doi:[10.1063/1.4960708](https://doi.org/10.1063/1.4960708).
- [79] Samuel T Chill, Matthew Welborn, Rye Terrell, Liang Zhang, Jean-Claude Berthet, Andreas Pedersen, Hannes Jónsson, and Graeme Henkelman. EON: Software for long time simulations of atomic scale systems. *Modelling and Simulation in Materials Science and Engineering*, 22(5):055002, July 2014. ISSN 0965-0393, 1361-651X. doi:[10.1088/0965-0393/22/5/055002](https://doi.org/10.1088/0965-0393/22/5/055002).
- [80] Eric D. Hermes, Khachik Sargsyan, Habib N. Najm, and Judit Zádor. Sella, an Open-Source Automation-Friendly Molecular Saddle Point Optimizer. *Journal of Chemical Theory and Computation*, 18(11):6974–6988, November 2022. ISSN 1549-9618. doi:[10.1021/acs.jctc.2c00395](https://doi.org/10.1021/acs.jctc.2c00395).
- [81] Olli-Pekka Koistinen, Freyja B. Dagbjartsdóttir, Vilhjálmur Ásgeirsson, Aki Vehtari, and Hannes Jónsson. Nudged elastic band calculations accelerated with Gaussian process regression. *The Journal of Chemical Physics*, 147(15):152720, September 2017. ISSN 0021-9606. doi:[10.1063/1.4986787](https://doi.org/10.1063/1.4986787).
- [82] Alexander Denzel, Bernard Haasdonk, and Johannes Kästner. Gaussian Process Regression for Minimum Energy Path Optimization and Transition State Search. *The Journal of Physical Chemistry A*, 123(44):9600–9611, November 2019. ISSN 1089-5639. doi:[10.1021/acs.jpca.9b08239](https://doi.org/10.1021/acs.jpca.9b08239).
- [83] Ask Hjorth Larsen, Jens Jørgen Mortensen, Jakob Blomqvist, Ivano E. Castelli, Rune Christensen, Marcin Dułak, Jesper Friis, Michael N. Groves, Bjørk Hammer, Cory Hargus, Eric D. Hermes, Paul C. Jennings, Peter Bjerre Jensen, James Kermode, John R. Kitchin, Esben Leonhard Kolsbjerg, Joseph Kubal, Kristen Kaasbjerg, Steen Lysgaard, Jón Bergmann Maronsson, Tristan Maxson, Thomas Olsen, Lars Pastewka, Andrew Peterson, Carsten Rostgaard, Jakob Schiøtz, Ole Schütt, Mikkel Strange, Kristian S. Thygesen, Tejs Vegge, Lasse Vilhelmsen, Michael Walter, Zhenhua Zeng, and Karsten W. Jacobsen. The atomic simulation environment—a Python library for working with atoms. *Journal of Physics: Condensed Matter*, 29(27):273002, June 2017. ISSN 0953-8984. doi:[10.1088/1361-648X/aa680e](https://doi.org/10.1088/1361-648X/aa680e).

- [84] Yorick L. A. Schmerwitz, Vilhjálmur Ásgeirsson, and Hannes Jónsson. Improved Initialization of Optimal Path Calculations Using Sequential Traversal over the Image-Dependent Pair Potential Surface. *Journal of Chemical Theory and Computation*, 20(1):155–163, January 2024. ISSN 1549-9618. doi:10.1021/acs.jctc.3c01111.
- [85] Søren Smidstrup, Andreas Pedersen, Kurt Stokbro, and Hannes Jónsson. Improved initial guess for minimum energy path calculations. *The Journal of Chemical Physics*, 140(21):214106, June 2014. ISSN 0021-9606. doi:10.1063/1.4878664.
- [86] Miha Gunde, Nicolas Salles, Anne Hémerlyck, and Layla Martin-Samos. IRA: A shape matching approach for recognition and comparison of generic atomic patterns. *Journal of Chemical Information and Modeling*, 61(11):5446–5457, November 2021. ISSN 1549-9596. doi:10.1021/acs.jcim.1c00567.
- [87] Rohit Goswami. Two-dimensional RMSD projections for reaction path visualization and validation. *MethodsX*, page 103851, March 2026. ISSN 2215-0161. doi:10.1016/j.mex.2026.103851.
- [88] Ralf Meyer and Andreas W. Hauser. Geometry optimization using Gaussian process regression in internal coordinate systems. *The Journal of Chemical Physics*, 152(8):084112, February 2020. ISSN 0021-9606. doi:10.1063/1.5144603.
- [89] Sandip De, Albert P. Bartók, Gábor Csányi, and Michele Ceriotti. Comparing molecules and solids across structural and alchemical space. *Physical Chemistry Chemical Physics*, 18(20):13754–13769, May 2016. ISSN 1463-9084. doi:10.1039/C6CP00415F.
- [90] Giulio Imbalzano, Andrea Anelli, Daniele Giofré, Sinja Klees, Jörg Behler, and Michele Ceriotti. Automatic selection of atomic fingerprints and reference configurations for machine-learning potentials. *The Journal of Chemical Physics*, 148(24):241730, April 2018. ISSN 0021-9606. doi:10.1063/1.5024611.
- [91] Robert B. Gramacy. laGP: Large-Scale Spatial Modeling via Local Approximate Gaussian Processes in R. *Journal of Statistical Software*, 72:1–46, August 2016. ISSN 1548-7660. doi:10.18637/jss.v072.i01.
- [92] Yossi Rubner, Carlo Tomasi, and Leonidas J. Guibas. The Earth mover’s distance as a metric for image retrieval. *International Journal of Computer Vision*, 40(2):99–121, November 2000. ISSN 1573-1405. doi:10.1023/A:1026543900054.
- [93] H. W. Kuhn. The Hungarian method for the assignment problem. *Naval Research Logistics Quarterly*, 2(1-2):83–97, 1955. ISSN 1931-9193. doi:10.1002/nav.3800020109.
- [94] Stephen P. Boyd and Lieven Vandenbergh. *Convex Optimization*. Cambridge University Press, Cambridge, UK ; New York, 2004. ISBN 978-0-521-83378-3.
- [95] Florian A. Potra and Stephen J. Wright. Interior-point methods. *Journal of Computational and Applied Mathematics*, 124(1):281–302, December 2000. ISSN 0377-0427. doi:10.1016/S0377-0427(00)00433-7.
- [96] Ali Rahimi and Benjamin Recht. Random Features for Large-Scale Kernel Machines. In *Advances in Neural Information Processing Systems*, volume 20. Curran Associates, Inc., 2007.
- [97] Pietro Novelli, Giacomo Meanti, Pedro J. Buigues, Lorenzo Rosasco, Michele Parrinello, Massimiliano Pontil, and Luigi Bonati. Fast and fourier features for transfer learning of interatomic potentials, May 2025.
- [98] Shin Sato. On a New Method of Drawing the Potential Energy Surface. *Journal of Chemical Physics*, 23(3):592–593, March 1955. ISSN 0021-9606. doi:10.1063/1.1742043.
- [99] Arslan Mazitov, Sofia Chorna, Guillaume Fraux, Marnik Berx, Giovanni Pizzi, Sandip De, and Michele Ceriotti. Massive atomic diversity: A compact universal dataset for atomistic machine learning. *Scientific Data*, 12(1):1857, November 2025. ISSN 2052-4463. doi:10.1038/s41597-025-06109-y.